Volume 65C
Number 1
Jan.-Mar. 1961

THE UNIVERSITY OF MICHIGAN
MAR 15 1961
ENGINEERING LIBRARY

Engineering and Instrumentation

SECTION C

JOURNAL OF RESEARCH

NATIONAL BUREAU OF STANDARDS

Journal of Research
of the
National Bureau of Standards

C. Engineering and Instrumentation

JAN.–MAR. • 1961

VOLUME • 65C

NUMBER • 1

Editor: W. A. Wildhack

Associate Editors: G. F. Montgomery, R. B. Jacobs

Publication dates:
Feb. 15, May 15, Aug. 15, Nov. 15, 1961

JOURNAL OF RESEARCH

The National Bureau of Standards Journal of Research reports research and development in the fields of activity shown at right. Also included from time to time are survey articles on topics closely related to the Bureau's scientific and technical program.

The Journal is published in four separate sections as follows:

A. Physics and Chemistry

Contains papers of interest primarily to scientists working in these fields. Issued six times a year. Annual subscription: domestic, $4.00; foreign, $4.75.

B. Mathematics and Mathematical Physics

Presents studies and compilations designed mainly for the mathematician and the theoretical physicist. Issued quarterly. Annual subscription: domestic, $2.25; foreign, $2.75.

C. Engineering and Instrumentation

Reports research and development results of interest chiefly to the engineer and the applied scientist. Issued quarterly. Annual subscription: domestic, $2.25; foreign, $2.75.

D. Radio Propagation

Reports work in radio propagation physics and upper atmospheric research. Issued six times a year. Annual subscription: domestic, $4.00; foreign, $4.75.

Functions and Activities

The functions of the National Bureau of Standards are set forth in the Act of Congress, March 3, 1901, as amended. These include the development and maintenance of the national standards of measurement and the provision of means and methods for making measurements consistent with these standards; the determination of physical constants and properties of materials; the development of methods and instruments for testing materials, devices, and structures; advisory services to government agencies on scientific and technical problems; invention and development of devices to serve special needs of the Government; and the development of standard practices, codes, and specifications. The work includes basic and applied research, development, engineering, instrumentation, testing, evaluation, calibration services, and various consultation and information services. The Bureau also serves as the Federal technical research center in a number of specialized fields. The scope of activities of the National Bureau of Standards is suggested in the following listing of the divisions and sections engaged in technical work.

Washington, D. C.

Electricity. Resistance and Reactance. Electrochemistry. Electrical Instruments. Magnetic Measurements. Dielectrics.
Metrology. Photometry and Colorimetry. Refractometry. Photographic Research. Length. Engineering Metrology. Mass and Scale. Volumetry and Densimetry.
Heat. Temperature Physics. Heat Measurements. Cryogenic Physics. Equation of State. Statistical Physics.
Radiation Physics. X-Ray. Radioactivity. Radiation Theory. High Energy Radiation. Radiological Equipment. Nucleonic Instrumentation. Neutron Physics.
Analytical and Inorganic Chemistry. Pure Substances. Spectrochemistry. Solution Chemistry. Analytical Chemistry. Inorganic Chemistry.
Mechanics. Sound. Pressure and Vacuum. Fluid Mechanics. Engineering Mechanics. Rheology. Combustion Controls.
Organic and Fibrous Materials. Rubber. Textiles. Paper. Leather. Testing and Specifications. Polymer Structure. Plastics. Dental Research.
Metallurgy. Thermal Metallurgy. Chemical Metallurgy. Mechanical Metallurgy. Corrosion. Metal Physics.
Mineral Products. Engineering Ceramics. Glass. Refractories. Enameled Metals. Crystal Growth. Constitution and Microstructure.
Building Research. Structural Engineering. Fire Research. Mechanical Systems. Organic Building Materials. Codes and Safety Standards. Heat Transfer. Inorganic Building Materials.
Applied Mathematics. Numerical Analysis. Computation. Statistical Engineering. Mathematical Physics.
Data Processing Systems. Components and Techniques. Digital Circuitry. Digital Systems. Analog Systems. Applications Engineering.
Atomic Physics. Spectroscopy. Radiometry. Solid State Physics. Electron Physics. Atomic Physics.
Instrumentation. Engineering Electronics. Electron Devices. Electronic Instrumentation. Mechanical Instruments. Basic Instrumentation.
Physical Chemistry. Thermochemistry. Surface Chemistry. Organic Chemistry. Molecular Spectroscopy. Molecular Kinetics. Mass Spectrometry. Molecular Structure and Radiation Chemistry.
Office of Weights and Measures.

Boulder, Colo.

Cryogenic Engineering. Cryogenic Equipment. Cryogenic Processes. Properties of Materials. Gas Liquefaction.
Ionosphere Research and Propagation. Low Frequency and Very Low Frequency Research. Ionosphere Research. Prediction Services. Sun-Earth Relationships. Field Engineering. Radio Warning Services.
Radio Propagation Engineering. Data Reduction Instrumentation. Radio Noise. Tropospheric Measurements. Tropospheric Analysis. Propagation-Terrain Effects. Radio-Meteorology. Lower Atmosphere Physics.
Radio Standards. High Frequency Electrical Standards. Radio Broadcast Service. Radio and Microwave Materials. Atomic Frequency and Time Interval Standards. Electronic Calibration Center. Millimeter-Wave Research. Microwave Circuit Standards.
Radio Systems. High Frequency and Very High Frequency Research. Modulation Research. Antenna Research. Navigation Systems. Space Telecommunications.
Upper Atmosphere and Space Physics. Upper Atmosphere and Plasma Physics. Ionosphere and Exosphere Scatter. Airglow and Aurora. Ionospheric Radio Astronomy.

U.S. DEPARTMENT OF COMMERCE
Luther H. Hodges, Secretary

NATIONAL BUREAU OF STANDARDS
A. V. Astin, Director

Order all publications from the Superintendent of Documents
U.S. Government Printing Office, Washington 25, D.C.

Use of funds for printing this publication approved by the Director of the Bureau of the Budget (June 24, 1958).

JOURNAL OF RESEARCH of the National Bureau of Standards—C. Engineering and Instrumentation
Vol. 65C, No. 1, January–March 1961

Electronic Scanning Microscope for a Spectrographic Plate Comparator

M. L. Kuder

(October 6, 1960)

A scanning microdensitometer has been constructed for the purpose of analyzing spectrographic plates. The instrument facilitates reading the data and increases the speed and accuracy over other methods.

A small section of the plate is scanned at one time and converted to a magnified X–Y plot of density versus wavelength displayed on the screen of a cathode ray oscilloscope. The display includes an electronically produced fiducial line which is used as a reference point for measurements of line position. An alternate type of display may be used which includes the superposition of the mirror image trace on the original trace. This is preferred in some cases for setting on unsymmetrical lines.

Resolution to better than 0.001 millimeter on the plate is consistently obtained, and the fiducial line remains stable to this precision for several hours. Provision is made for observing up to five adjacent spectrograms on a single plate.

1. Introduction

Wavelength measurements of spectral lines may be made by accurately comparing the relative positions of the images recorded on a spectrograph plate. If the lines are sharp and distinct they may be scaled by an operator using a visual microscope having a suitable arrangement of cross hairs and a calibrated lead screw for advancing the spectrograph plate. However, if the lines are faint, unsymmetrical or superimposed on other lines, visual reading is difficult.

Greater accuracy and convenience is obtained by the use of a scanning microscope used as a microdensitometer to convert the image densities into analog values, these being presented as a display on a cathode ray oscillograph. The use of such a display of density versus wavelength in analyzing spectrograph plates is not new.[1] However, an electronic scanning microscope (figs. 1 and 2) has been devised which incorporates certain refinements in the principles of operation of a device of this type. The instrument shown was engineered to rapidly scan spectral lines (on a plate) and convert them into a magnified X–Y coordinate plot, which is displayed on a cathode ray screen. This device produces an unusually stable and sharply defined display of the X–Y plot of densities versus wavelength.

An electronically generated fiducial index has been integrated into the sytem in such a way that unusual stability has resulted in respect to the wavelength position which it indicates. This fiducial index appears on the cathode ray screen display superimposed upon the X–Y plot of the spectral pattern. The integrated generation of a fiducial index makes it possible to manipulate any of the normal controls of the oscilloscope without engendering any relative motion between the fiducial index and the X–Y plot.

The overall stability of the display together with the relative stability of the fiducial index line is sufficient to insure wavelength position readings within an accuracy of 0.001 mm or better when interpolating these wavelength positions from spectral lines of a parallel track on the same plate. In order to obtain absolute measurements of wavelength it is customary to record the spectrum of a standard source on an adjacent track on the same spectrograph plate. This makes it more convenient and more accurate to obtain a measurement of the relative positions of unknown spectral lines for accurate interpolation of their absolute wavelength.

The photographic density of the spectral lines as recorded on the plate may be read directly from the oscilloscope since d–c amplification of the scanned signal is employed throughout. The determination of ordinate deflection versus density calibration of the oscilloscope is not difficult, since the instrument yields the same deflections for static densitometer readings. Thus, with or without scanning, a standard density step wedge may be inserted in place of the spectrograph plate when calibrating the ordinate deflection representing densities. The instrument as presently designed yields a linear relationship between light intensities and ordinate deflections. This will ordinarily make it difficult to read photographic densities much above 2.2 with any degree of accuracy. For densities below 2.2 it is possible to obtain density readings with an accuracy of approximately 5 percent.

[1] A photoelectric setting device for a spectrum plate comparator, by F. S. Tompkins and M. Fred, J. Opt. Soc. **41**, p. 641 (Sept. 1951).

573960—61——1

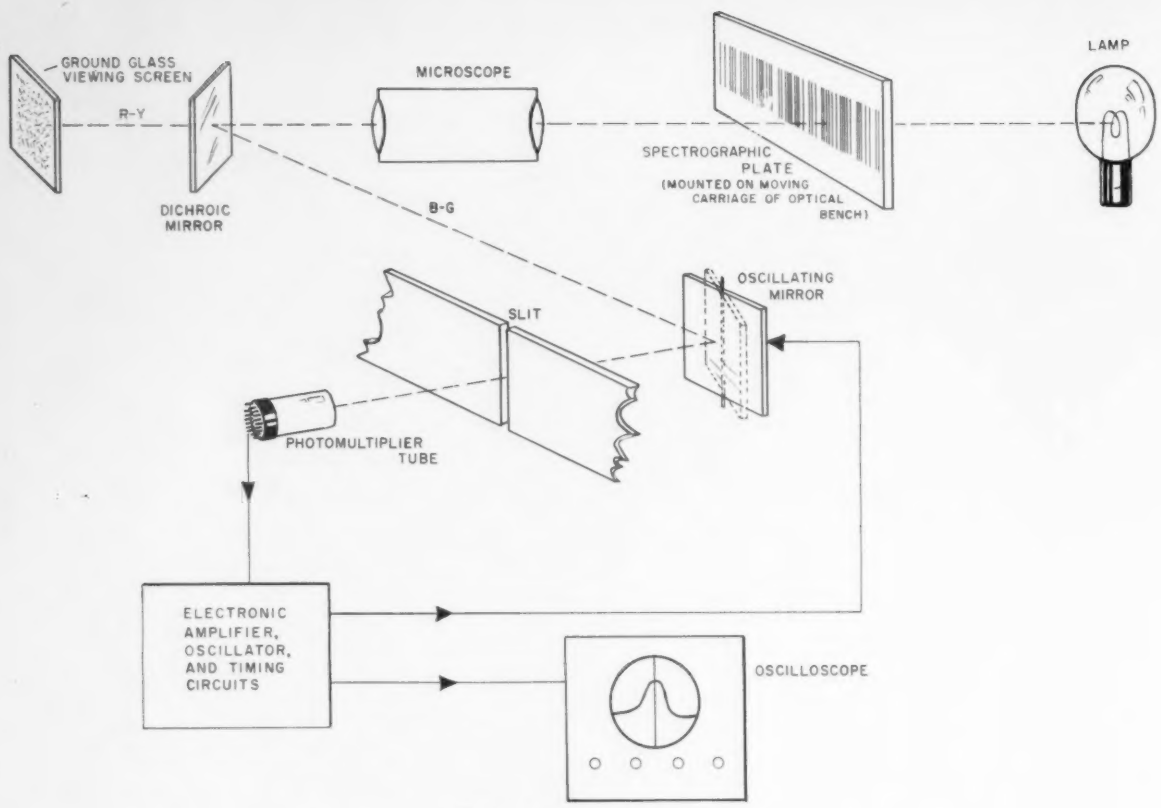

FIGURE 1. *Optical system.*

FIGURE 2. *Operator's view of assembled microscope, with the electronic controls on the right.*

2. Electronic Scanning Microscope

2.1. Operational Goals

Basically, an ordinate-line scanning microscope will provide video signals for a density versus wavelength display on a cathode-ray tube. In order that such a display may be useful for making measurements of a spectrograph-plate, it must first be stable and free of drift. Secondly, for precision measurements, the display should have a "generated" fiducial index which is related electronically in a very stable fashion to the optical axis of the microscope. Centering-drift of the oscilloscope will then be relatively unimportant. Direct-current amplification of the ordinate or density signal is essential for making absolute density estimates from the display. In order to make precision wavelength measurements the spectrograph plate should preferably have a pair of coherently exposed "standard" spectra (on the two outside tracks) such as thorium and iron. Using premeasured lines of these standard spectra, precise interpolation of the adjacent spectral tracks

may be accomplished. In this procedure the electro-optical fiducial-index is used in conjunction with the micrometer lead screw for making precise settings on selected lines of the parallel spectral tracks. Interpolation between the unknown and the standard is then accomplished by calculations from the micrometer lead-screw readings used to advance the spectrograph plate under the microscope. If the oscilloscope displays a highly magnified image (of the plate) which is very stable and free of noise, it is possible to resolve the settings more acutely, more rapidly, and with less eye strain than is possible with the conventional optical microscope.

2.2. Optical Scanner

The optical scanning portion of the instrument (figs. 1 and 2) consists of a special low-power microscope with a magnification of approximately 10 diameters. Immediately behind the objective lens a dichroic mirror is inserted which splits the image beam into essentially equal parts of the visible spectrum. The red-yellow portion of the spectrum is delivered via bent optics to a viewing ground glass screen. The blue-green portion of the microscope beam is reflected from a vibrating mirror which is part of an electromechanical-optical transducer. Thence the oscillating beam impinges upon a slit of approximately 0.125 mm width and 13 cm length. Behind this slit five end-on photomultipliers are mounted, each of which receives the light from the lines of adjacent spectra on the same spectrograph plate.

A miniature DuMont 6365, end-on photomultiplier was selected for this application because its small size permits close stacking behing the common slit and also because the 6365 yields a better signal to noise ratio than some other older types that were tried. Also the "dark noise" is probably reduced by keeping the unilluminated portion of the photocathode to a minimum. The ideal photocathode might be one which was only a little wider than the slit aperture in front of it. Individual separation adjustment of the photomultiplier tubes is provided along the slit aperture to compensate for differences in separation of the parallel spectral tracks.

The vibrating mirror causes the 10 times magnified image of the spectrum to traverse the slit aperture before the photomultipliers. This mirror scans the image through a very small angle in sinusoidal fashion and sweeps over a maximum of approximately 0.5 mm on the spectrograph plate, with a slit-scanning resolution of 0.0005 in. or 12.7 μ. The electromagnetic mirror transducer shown in figure 3 consists of a miniature dynamic-speaker movement which imparts a push-pull movement to one edge of the mirror while the other edge of the mirror is affixed to a flexure plate made of phosphor-bronze. This transducer is self-resonant at approximately 400 cycles and is driven electrically at a frequency slightly below resonance. It is excited by a sine wave source of moderately constant frequency derived from a high-Q LC-circuit oscillator followed

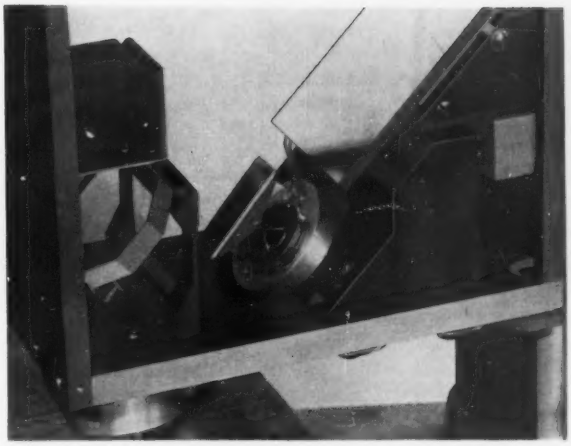

FIGURE 3. *The electro-magnetic mirror transducer.*

by a push-pull power amplifier. A gain control in this amplifier provides adjustment of the amplitude of vibration and hence of the scanning width on the spectrograph plate. A tilt adjustment has been provided for aligning the slit with the images of the spectrograph plate lines. If an identical spectral line (standard) is provided on the two outside tracks of the spectrograph plate, the slit may be readily and precisely aligned by adjusting the slit for coherent oscillograms of the scanning signals of these two outside tracks, as they are viewed on two separate oscilloscopes.

2.3. Programed Oscilloscope Sweep

The oscilloscope sweep as well as the source for the vibrating mirror transducer originates with the 400-cycle oscillator. In the block diagram, figure 4, this oscillator (1) is shown as the prime source for the network of electronics. This oscillator signal is fed through a paraphase amplifier which splits the signal into two signals which are mutually 180° out of phase. These two opposite phased signals of 400 cycles each pass through a pair of cathode follower impedance changers (3 and 5) which in turn feed into a pair of asymmetric clamps (4 and 6), which alternately clamp off first one and then the other of these two opposite-phased signals. These two asymmetric clamps are alternately turned "off" and "on" by the binary counter in such a manner as to pass exactly one cycle of each phase signal in sequence to the cathode follower (7). Each cycle passed by the asymmetric clamp is turned "on" at the peak of the sine wave and "off" at the next peak. The binary counter (12) is synchronized by means of the phase shifter (10) and the Schmitt trigger (11) to accomplish this precise timing for clamping the sine wave sweep signal at the crest of the sine wave. This paraphase sweep signal

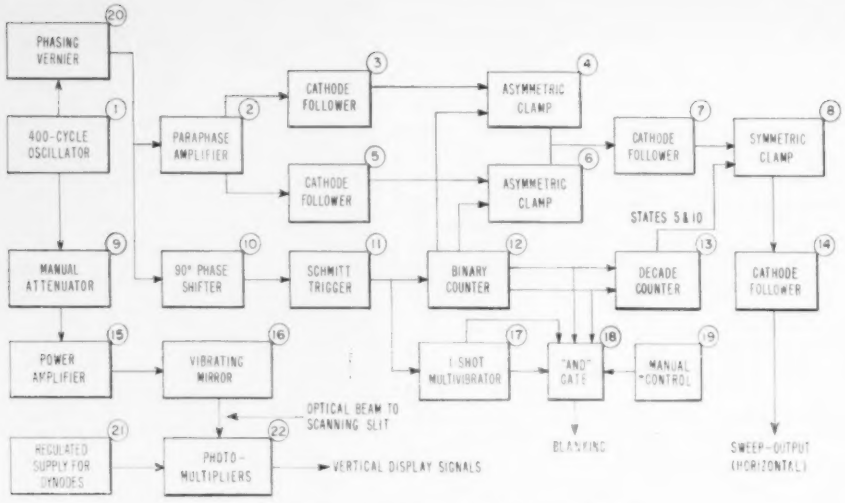

FIGURE 4. *The block diagram of the electronic system.*

presented on alternate sweeps has the property of generating a mirror image presentation of the scanned area of the spectrograph plate. The mirror image may be superimposed on the normal image. See figure 5 for oscillogram of this complex sweep signal.

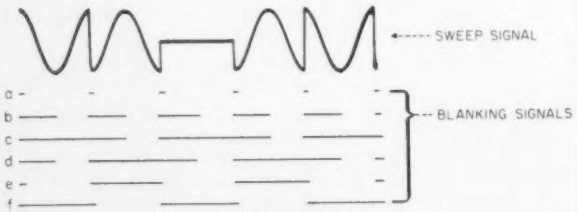

FIGURE 5. *Paraphase sweep-signal, and blanking signals.*

(a) Flyback blanking only.
(b) Flyback and retrace blanking for dual-presentation.
(c) Flyback, retrace, and mirror image blanking.
(d) Flyback, retrace, and normal image blanking.
(e) Flyback, and normal image blanking.
(f) Flyback, and mirror image blanking.

The binary counter also drives a decade counter (13) which in turn operates the symmetric clamp (8). The symmetric clamp has the property of collapsing the output signal precisely to the center of the sine wave for exactly 1 out of every 5 cycles. It is this collapse of the sine wave sweep signal to its exact center or zero voltage position which results in the generation of a stable fiducial line on the oscilloscope. During this single collapsed sweep interval the vibrating mirror transducer goes through its normal gyrations causing the vertical deflection of the oscilloscope to proceed in the normal manner with its signals from the photomultiplier. The normal deflection signals from the photomultipliers then plot the vertical fiducial line on the oscilloscope during this single collapsed sweep.

It will be noted that the same 400 cycle oscillator (1) feeds the power amplifier (15) through the manual attenuator (9). This latter link provides the necessary power to operate the vibrating mirror transducer (16) which of course vibrates synchronously with the sweep signals since they both operate from the same primary signal source. A manual attenuator (9) permits the selection of any width of scanning of the spectrograph plate from approximately ½ millimeter down to zero, by adjustment of the transducer driver amplitude. The vibrating mirror transducer is a-c coupled to the amplifier through an impedance matching transformer which also has the property of eliminating any d-c component from the amplifier which could tend to cause a d-c drift in the central position of the vibrating mirror. Also, since the transducer is driven by a coil in a magnetic field, there are no moving components in the vibrating mirror system to accrue residual magnetism which would tend to affect the stability of the central position of the mirror. The choice of a high (400 cycle) scanning frequency permits a relatively rigid flexure-plate mount for the mirror, further insuring mechanical stability for positioning the nominal or central position of the mirror during its vibrating cycle, which precisely

corresponds to the static position of the mirror when the transducer is at rest. The symmetric clamp (8) thus plots a stable fiducial line representing the rest position of the vibrating mirror. Since the symmetric clamp (8) is a high-impedance circuit which is sensitive to loading it is followed by the cathode-follower (14) to prevent any disturbance of this clamping circuit.

2.4. Selective Blanking

With the 400 cycle oscillator source (1), coming through (2), (3), (4), (7), (8), and (14) used directly for the oscilloscope sweep, a single pattern is traced during one-half of the cycle going from a peak to a trough of the 400 cycle source, while another (backward) retrace of the same pattern results from the other half of the 400 cycle signal which corresponds to the returning traverse of the mirror to its starting point. This retracing of the pattern during the last half cycle of the sine wave corresponding to the return sweep of the mirror is useful for checking phase shift in the system but is generally undersirable for measurement observations, since it tends to broaden the trace and reduce acuity. Any change in separation of the retrace pattern with respect to the normal trace is a sensitive indication of relative phase shift between the motion of the vibrating mirror and the oscilloscope electrical sweep. Any such phase shift can be manually nulled (compensated) rendering the retrace coincident with the nominal trace by adjustment of the phasing vernier (20).

During the normal "reading" operation of the instrument it is usually desirable to eliminate the retrace pattern. This is accomplished by the one-shot multivibrator (17) providing a blanking signal to the oscilloscope during one-half of the sine wave sweep. The result is a steady-state "single" sweep or unilateral display of the density versus wavelength in the scanned zone. However, a dual or bilateral display of the same X-Y plot may be presented in superimposed fashion, while maintaining blanking of the retraces. The use of the paraphase sinusoidal sweep makes such a dual display possible with coherent superimposition. Subsequently when the spectrograph plate micrometer screw is moved, the mirror image presentation moves in the opposite direction with respect to the normal presentation. This provides another convenient mode of matching selected components of the pattern as they merge together at the center of the sweep. This method of matching the "mirror" image with the "normal" image is particularly useful when trying to "set" on an unsymmetrical line. With this method it is possible to estimate an equal energy (spectral) distribution on either side of the fiducial line with much better visual discretion than with a single presentation.

Control signals taken directly from the binary counter (12) are used to operate the "AND" gate (18) through manual selection provided by (19), permitting the operator to select either the normal or the mirror image presentation or both. An ON-OFF control for the one-shot multivibrator (17) permits the operator to select or reject the retrace pattern for both of the two paraphase sweeps. Whenever the one-shot multivibrator (17) is in the OFF position permitting viewing of the retrace it is not turned completely off but rather is returned to a minimum time interval (see fig. 5a) which is just sufficient to blank the flyback which occurs during the transition between the alternate sweeps.

2.5. Typical Spectrum Patterns

Some typical patterns for the spectra of thorium are shown in the illustrations figures 6 to 10. Tompkins and Fred (see footnote 1) demonstrated this type of oscilloscope display, in 1951, using a revolving prism as the scanning element. These are Zeeman patterns which have typical symmetry. However, the spectral illustrations show an insufficiently small portion of the Zeeman pattern to reveal its symmetry. In figure 6a a portion of a Zeeman spectrum is shown first, in the "normal" single oscillogram form as resolved by this instrument; and secondly, in 6b, it is shown as it appears with the "mirror-image" oscillogram superimposed.

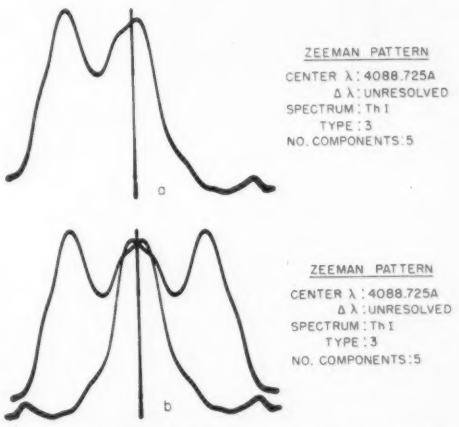

FIGURE 6a. *Portion of Zeeman pattern shown in "normal" presentation.*

FIGURE 6b. *Zeeman pattern of 6a shown as it appears in dual presentation (with mirror image superimposed).*

The latter is the "dual presentation." Figure 7 shows the instrument's ability to resolve some typical fine magnetic-splitting component (Zeeman) spectral lines with a minimum of noise in the oscillogram signal. The oscillograms shown in all the illustrations are unretouched photographs taken directly from the instrument's oscilloscope screen. The spectrograph plates used for these presentations were made with a dispersion factor of 0.881 A/mm.

In figure 8b, the resulting oscillograph pattern of figure 8a representing the density versus wavelength of spectral lines has been superimposed upon a

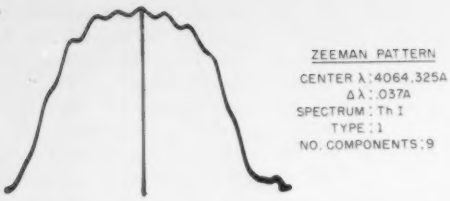

FIGURE 7. *Zeeman pattern, showing fine splitting components resolved without "noise".*

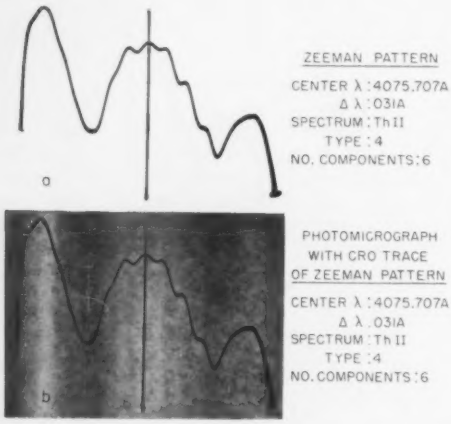

FIGURE 8. *Portion of Zeeman pattern showing (a) oscillograph presentation only, and (b) oscillograph presentation with superimposed photomicrograph of corresponding spectrograph plate.*

photomicrograph of the portion of the spectrograph plate which represents this scanning study. An examination of this photomicrograph concurrently with the associated oscillogram shows the remarkable integrating ability of the scanning system to eliminate the effect of the graininess of the spectrograph plate itself. This is not surprising when one considers that the scanning is accomplished with a line scanner rather than a point scanner. For with the line scanner each horizontal element scanned looks at a much larger equivalent vertical portion of the spectrograph plate than is shown in these photomicrographic illustrations.

2.6. Auxiliary Instrumentation

When the operator tries to read very faint lines or grossly overexposed spectral lines he will find it rather difficult to obtain sufficient amplitude on the vertical deflection of the oscilloscope for adequate resolution. This condition will tempt the operator to increase the vertical gain of the oscilloscope to the point where portions of the pattern will deflect off the face of the oscilloscope. While this mode of operation does yield a better resolution for spectral lines representing very small increments of density, it makes it necessary to repeatedly re-center the display for practically every advancement of the spectrograph plate under the comparator lens. Nevertheless, this mode of operation seems to be highly necessary to enable the reading of very faint lines and very saturated lines but it becomes a most inconvenient procedure, because of the need for frequent re-centering of the display image. This inconvenience may be overcome with an electronic attachment.

In order to avoid constant resetting of the gain and centering controls, automatic electronic centering of a sampled segment is provided. A sampling system raises or lowers the signal trace so that the segment of interest appears in the screen's center regardless of the amplitude or complexity of the signal waveform. An auxiliary piece of equipment provides such automatic vertical centering of the image continuously and simultaneously for all four oscilloscopes. A block diagram of the electronic circuitry which accomplishes this useful automatic centering is shown in figure 9. The principle of

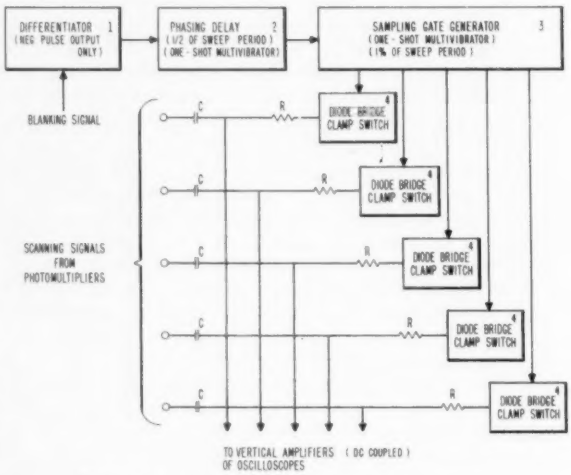

FIGURE 9. *Automatic image centering device.*

operation of this device is relatively simple and consists of the following technique. The leading edge of the blanking signal from the sweep generator circuitry is fed into a differentiator (1) which selects the negative transition of the blanking signal and provides a sharp pulse at that time. This negative pulse triggers a one-shot multivibrator phasing delay (2) which in turn provides a pulse output which occurs at the time the sweep is crossing the fiducial index line. This delayed pulse from (2) is used to trigger the sampling gate generator (3). The sampling gate generator is another one-shot multivibrator which generates a very short pulse whose duration is approximately 1 percent of the sweep

period or sweep length. This sampling gate pulse operates a multiplicity of diode-bridge clamp-switches (4). The diode-bridge clamp-switches in turn provide for momentary grounding of the d–c return end of the a–c coupling resistor (R) only during the time of the sampling gate. The five a–c couplings shown are conveying the output of the five photomultiplier signals to the d–c amplifiers of the corresponding oscilloscopes. Grounding the d–c return resistance of these a–c couplings only when the sweep is crossing the fiducial line causes that part of the display image to always come to ground potential. This makes it possible to initially set the vertical centering of the oscilloscope so that the beam is vertically centered for a zero voltage or grounded input. The resultant displays obtained with this attachment under these conditions will always produce a trace which crosses the fiducial line at the center of the CRO tube, regardless of the magnitude or position of the balance of the display. The diode-bridge clamp effectively provides a d–c return for the a–c coupling at only one point in a repetitive pattern of an asymmetric signal. Since the signal is repetitive, the grounding for a brief instant at the same repetitive phase time will result in the generation of a bias on the load end of the a–c coupling condenser. After a time of about 5RC/d (d denotes duty cycle) a steady state bias voltage is established on the load end of the coupling condenser, and the pulse current thru "R" falls to zero. Thus on subsequent repetitions of the trace, the vertical signal passes thru a zero voltage point as it crosses the fiducial line during the gate-pulse interval. The time required for reaching a steady-state display after advancing the spectrograph plate is conveniently made about 0.2 sec.

Figure 10 shows a detailed schematic of the clamp-switch. The diode-bridge clamp-switch is actuated by a pair of coherent pulses of opposite polarity which are repetitive at any convenient rate. These pulses generate a bias voltage on the bridge end of these coupling condensers (C) which is nearly equal to the peak value of the control pulses. If these two control pulses come from a relatively low impedance driving source, a relatively high peak current will flow in the diodes for the brief time of that pulse, thus providing a very low resistance in all directions around the bridge. This results in the a–c signal being clamped to ground with the relatively low forward resistance of two diodes. In the interim between the control pulses all of the diodes are biased off by the accrued rectified bias charge on the coupling condensers (C). So long as this accrued bias on C exceeds the peak amplitude of the a–c signal to be clamped no clipping disturbance of the a–c signal will occur during the unclamped interval.

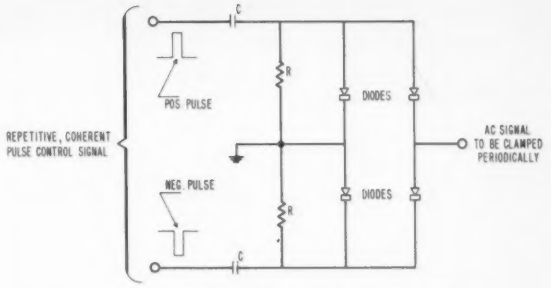

FIGURE 10. *Diode-bridge clamp-switch.*

The author thanks Herbert D. Cook and Louis A. Marzetta for their many helpful technical suggestions, and Paul Allison for his contribution of skilled craftsmanship in the fabrication of mechanical parts.

(Paper 65C1–50)

JOURNAL OF RESEARCH of the National Bureau of Standards—C. Engineering and Instrumentation
Vol. 65C, No. 1, January–March 1961

Viscoelastometer for Measurement of Flow and Elastic Recovery

Richard J. Overberg and Herbert Leaderman

(October 3, 1960)

An account is given of the design, performance, and method of operation of a concentric cylinder rotational viscoelastometer. The instrument is designed for measurement of flow and time-dependent elastic recovery of viscous elastic liquids for temperatures at which the viscosity lies in the range of 10^6 to 10^{12} poises and the elastic recovery is to be studied over a range of time from 1 second to 1 day. It is also suitable for measurement of non-Newtonian flow when the apparent viscosity is not much less than the Newtonian viscosity. The stator is a 1.5 inch precision-bore glass tube, which permits visual observation of the sample. Interchangeable rotors (radius ratios 0.21, 0.58, 0.92) are provided, the smallest for materials which are only slightly non-Newtonian and have a small compliance. Torque is applied by weights through a torque drum. Mirrors on the rotor shaft and a photoelectric recorder permit continuous recording of the rotor position. Mercury slip rings permit monitoring of rotor temperature. The maximum torque is 5×10^7 dyne-cm, while the torque due to static friction is 2.5×10^4 dyne-cm. The maximum surface shear stress is 6.5×10^6 dyne-cm^{-2}. Temperatures from -70 to $+160$ °C have been realized. "End-effect" studies have been made. Instrument compliance, temperature gradient correction, and the effect of inertia and friction on elastic recovery measurements are discussed. Data reduction methods for nonlinear behavior are developed.

1. Introduction

This paper gives an account of the design, performance, and method of operation of a concentric cylinder rotational viscoelastometer for measurement of flow and time-dependent elastic recovery of viscous elastic liquids. The design is based upon that of an earlier simpler instrument which has been previously described [1];[1] the present instrument possesses higher precision, greater experimental convenience, and more versatility than the previous viscoelastometer.

The instrument is designed in the first place to measure linear viscoelastic behavior of low molecular weight polymers, and also of high molecular weight polymers in the rubber-liquid transition region, for the temperature range in which the viscosity lies in the range 10^6 to 10^{12} poises. This represents roughly the range of temperature for which the time scale of elastic recovery lies in the range of 1 sec to 1 day. The viscoelastic behavior of other materials such as certain asphalts can also be investigated. Finally, the instrument can be used for the study of nonlinear elastic and flow behavior over a limited range.

2. Design Principles

The principles used in the design of the instrument and the relation of this method of measuring linear viscoelastic behavior to other methods will be briefly reviewed. It is well-known that noncrosslinked amorphous polymers above the glass-transition manifest a flow behavior which in general is non-Newtonian. Such materials are also viscoelastic, that is, they possess elastic as well as flow properties. Under conditions where the energy storage and the rate of energy dissipation are small, the response to shear stress is linear. The linear viscoelastic behavior in shear of a material may be characterized completely by its behavior in a test with a specified stress history. The most important methods of specification are the response to sinusoidal shear stress or shear strain history (dynamic tests) and the response to step-function shear stress or strain history (creep and stress relaxation tests). In the latter case the shear stress or shear strain is increased stepwise from zero to a given value and maintained constant thereafter. Other stress histories that have been considered are ramp function histories, in which the shear stress or strain is proportional to time [2], and impulse histories in which the stress or strain history varies with time as a delta function [3].

In the first two types of test, the significant range of time or frequency at any given temperature for noncrosslinked amorphous polymers may be of the order of fifteen decades. The practical time or frequency range of any piece of apparatus ranges from about two decades for dynamic tests to a maximum of about six decades for step-function experiments. It appears for such materials that the major effect of change in temperature is to change the time or frequency scale; hence the effective range of a piece of apparatus can be extended by change in temperature of test. The limits of this range depend upon instrumental factors.

From the phenomenological theory of linear viscoelastic behavior it can be shown that in principle the response over the whole significant range of time (or frequency) for any given stress (or strain)

[1] Figures in brackets indicate the literature references at the end of this paper.

history can be related to the response in any other type of test with another specified stress (or strain) history [4]. In practice, rheological data that can be measured directly by one method can be calculated from data obtained by another method only if the latter data are of extremely high precision. For example, the viscosity η and the steady state compliance J_e can be calculated from dynamic data or from stress relaxation data [5, 6]; however, such calculated values are often unreliable. These quantities on the other hand can be measured very simply with the rotational viscometer. Since the measurement of the limiting value of the elastic deformation for noncrosslinked polymers involves large permanent deformations, a simple shear apparatus in which the shear stress is uniform is not suitable, but a rotational method is indicated.

Considerations of the ranges in viscosity and time lead to a design in which the material is contained in a rotationally symmetrical surface with vertical axis and closed bottom. The material is sheared by the relative rotation between the cup and another rotationally symmetric, coaxial surface immersed in the material. Of the various possible designs, that using circular cylinders was chosen to permit accurate construction and alinement of the two surfaces. The Navier-Stokes equation for this geometry cannot be solved; it is necessary to use the solution for infinitely long cylinders together with an empirically determined end-correction. This "end-effect" has been obtained experimentally for ranges of two of the three geometrical parameters. The procedures for obtaining the elastic part of the shear creep compliance, $J(t)-t/\eta$, from elastic recovery measurements over a range of time in a rotational viscometer have been given previously [8].

In the present arrangement, the outer surface (the "cup") is fixed. The arrangement is such that a constant torque can be rapidly applied to or released from the inner cylinder (the "rotor"). Thus the shear stress on any given particle of fluid increases stepwise in time to a constant value and subsequently decreases similarly to zero. A study has been made of the frictional torque in the rotor system. The lower limit of the range in torque for a series of measurements of viscoelastic behavior is chosen to be well above this frictional torque.

In general, the flow and elastic behavior of viscoelastic liquids are found to be nonlinear. The steady flow of a polymeric material manifesting non-Newtonian behavior is associated with normal stress phenomena; in the concentric cylinder arrangement secondary flow will take place, manifesting itself as a rising up of the liquid in contact with the inner cylinder, the so-called Weissenberg effect, together with complicated axial and radial flow [9]. In measurements made with the viscoelastometer the upper limiting value of the torque is such that there is no perceptible disturbance to the free surface. It is then assumed that, over the whole range of torque, liquid particles move essentially in circles around the axis of the instrument and that secondary flow is negligible. Under these circumstances it is often found that the ratio of angular velocity to torque increases linearly with torque. A procedure was given previously for obtaining from such data the relationship between shear stress and rate of shear in a simple shear test [1, 8]. In this paper a more general method due to Pawlowski [10] is given.

The method of Pawlowski has been extended to derive the retarded elastic recovery behavior in simple shear for both finite and vanishing shear stress from nonlinear recovery data obtained in the viscometer.

The lower limiting value of the shear creep compliance J_g of amorphous polymers is of the order of 10^{-10} cm^2/dyne. However, the lowest measurable compliance is determined by the instrument compliance, which is limited by the necessity of reducing the moment of inertia of the rotor system to the minimum. The instrument compliance has been measured using a liquid cooled below its glass transition.

As a result of thermal conduction along the rotor shaft, the temperature of the rotor is slightly different from that of the thermostat. A slight temperature gradient thus exists through the liquid. A method has been developed, based upon relationships relating time-scale and temperature, to correct for this temperature gradient.

It has been demonstrated that the elastic part of the shear creep compliance and the non-Newtonian flow of noncrosslinked amorphous polymers are closely correlated [11]; these quantities cover a wide range of values depending upon the molecular weight distribution. The sensitivity of the present apparatus is varied by using interchangeable rotors of three different diameters. The sensitivity range can be further extended by the use of extra length rotors and stators. Since it is necessary to observe the free surface for manifestation of the Weissenberg effect, precision bore glass tubes are used for stators. This arrangement has the added advantage of allowing direct measurement of depth of immersion, which can vary appreciably over the range of temperatures of observation especially when the clearance between the plane ends is large and the radial gap is small.

3. Description of the Apparatus

The general arrangement of the viscoelastometer is shown diagrammatically in figure 1. An interchangeable rotor A is connected to the Kovar-glass insulating link D, which in turn is attached to the rotor shaft K. Two ball bearings J locate the rotor shaft in the housing V, which is supported by the collar E through a spacing ring H and gage blocks I. The spacing ring H is machined to a thickness corresponding to 0.025 in. clearance between the plane ends of the rotor and stator in the absence of the gage blocks. This clearance may be increased in steps to one inch, by means of gage blocks. The collar E rests on the support ring F which is located on the upper platform X. The stator B, a precision

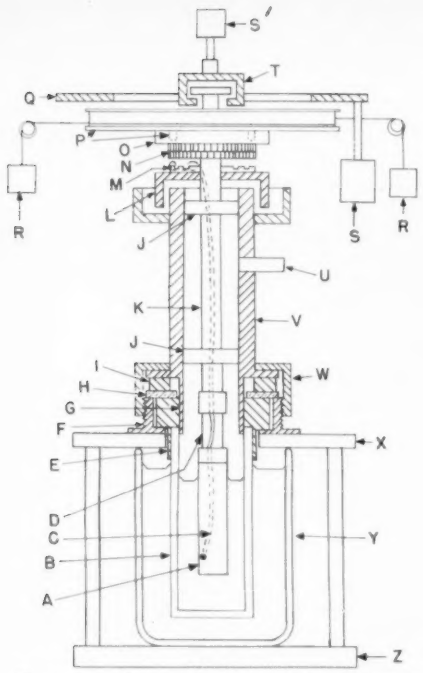

FIGURE 1. *Section drawing of viscoelastometer.*

A, Interchangeable rotor; B, Precision-bore glass stator; C, Rotor thermocouple; D, Kovar-glass insulating link; E, Collar; F, Support ring; G, Stator centering sleeve; H, Spacing ring; I, Gauge blocks; J, Axial thrust ball bearings; K, Rotor shaft; L, Mercury seal; M, Mercury slip-rings for thermocouple contacts; N, Multiple mirror; O, Torque drum adapter; P, Torque drum; Q, Torque drum arresting ring; R, Weights; S, S′, Solenoids; T, Drum removal device; U, Gas inlet tube; V, Rotor shaft housing; W, Locking ring; X, Upper platform; Y, Dewar vessel; Z, Sub-base.

bore glass tube with fused or cemented plane end, is cemented to the metal collar *E*. This is alined coaxially with the rotor by the centering sleeve *G*, which is an extension of the shaft housing. The rotor shaft housing, spacing ring, gage blocks, and stator are clamped together by the locking ring *W*. The shaft housing *V* carries a mercury seal *L* and a gas inlet tube *U*, which may be used to maintain the sample in the stator under an inert atmosphere, or, removing the mercury from *L*, to flush the bearings *J* with an inert gas. The leads from a thermocouple *C* in the rotor terminate in mercury slip rings *M*, attached to the rotating portion of the mercury seal. The upper end of the rotor shaft carries a multiple mirror system *N*, which is part of the recording arrangement and an adapter *O*, for the detachable torque drum *P*, which transmits its torque through four pins. The drum arresting ring *Q* can be pulled down against the torque drum by means of solenoids *S* to prevent rotation of the rotor system to which the weights *R* are attached. Two equal loads apply a pure torque to the drum by means of cords as shown. A solenoid *S′* activates a drum removal device *T*, which serves rapidly to disengage the drum *P* from the adapter *O*, and to press the drum against the arresting ring *Q*.

The stator is surrounded by a constant temperature bath contained in an unsilvered Dewar vessel *Y*. The controlled bath temperature does not vary more than ± 0.02 °C. Experiments have been carried out over the temperature range -40 to 160 °C. The lowest bath temperature that has been reached is -70 °C. The rotor and bath temperature can be monitored continuously during a test, and the rotor thermocouple serves to indicate when the rotor has come to temperature equilibrium following a change in bath temperature. Platinum foil is used for both the stationary and rotating contacts in the mercury rings. The rotor and bath thermocouples, placed side by side in a bath, give the same indicated emf over a range of temperature. Rotation of the rotor causes no change in the emf indicated. The temperatures are measured by means of a potentiometer sensitive to about 2 μv.

A photograph of the viscometer is shown in figure 2. Disassembly is accomplished by lowering the subbase *Z*, seen figures 1 and 2. After the central part of the subbase has been removed the Dewar may be lowered through the table. This arrangement allows the stator tube to be removed from below. At this stage the rotor can be removed from the connecting link, which extends below the platform.

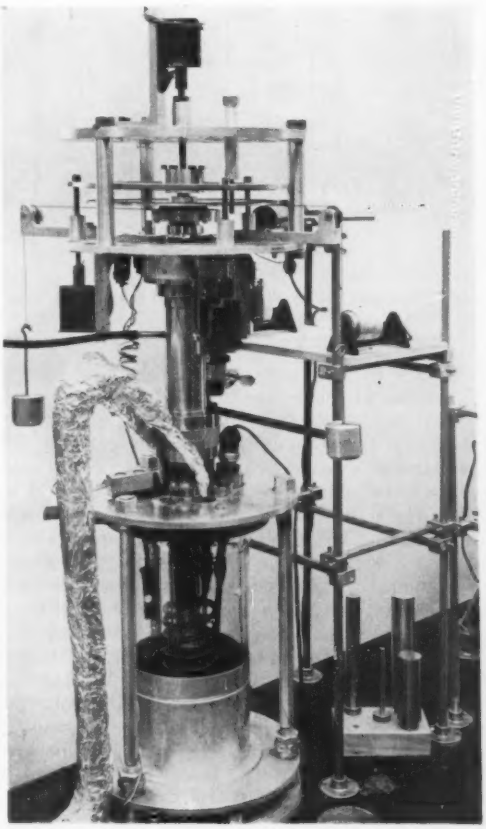

FIGURE 2. *Photograph of viscoelastometer.*

3.1. Rotor and Stator System

Neglecting the effect of the end, the shear stress at the surface of the rotor σ_1 is equal to the torque divided by twice the immersed volume of the rotor and the shear stress on any given cylindrical element varies inversely as the square of the radius. For materials that are only slightly non-Newtonian and for which the steady state elastic compliance J_e is small, the sensitivity of the apparatus is increased by using a small-diameter rotor, and conversely. The set of five interchangeable rotors, of diameters respectively 0.79 cm, 2.22 cm, and 3.50 cm, are shown in figure 3, which also shows the long and

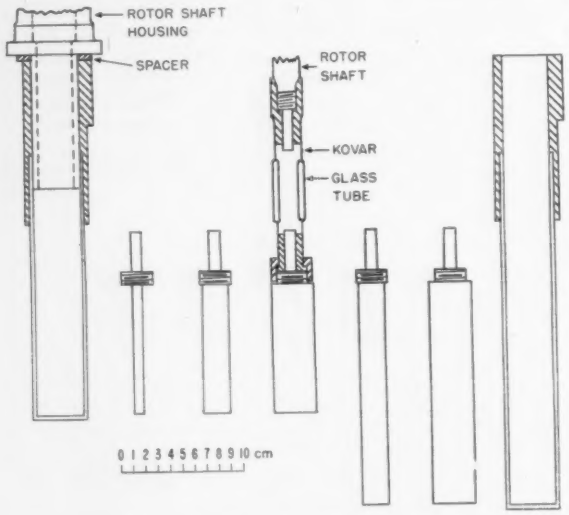

FIGURE 3. *Rotor and stator systems.*

The drawings represent to scale the five rotors, two sizes of stator tubes, and thermal insulating link.

short stators to be used respectively with the two long and three short rotors. The stator tubes are of 3.81 cm internal diameter and 0.32 cm nominal wall thickness, and the steel collars are cold-cemented in a jig by means of an acid proof cement.[2]

The steel collars of the stators are provided with three splines subtending and angle of 45° to the axis of rotation; these rest on similar splines in the support ring referred to previously. In order to remove the stator tube it is merely necessary first to loosen the clamp W seen in figure 1, which presses the collar of the shaft housing against the stator collar. The rotor system is raised slightly; the stator is rotated so that the two sets of splines clear each other, and then the stator is lowered through the platform Z. Shown in figure 3 is the Kovar-glass insulating link and the method of attachment of the link to the rotor and to the lower end of the rotor shaft.

[2] Sauereisen Acid Proof Cement No. 31, Sauereisen Cement Company, Pittsburgh, Pa.

Table 1 gives the range in the shear stress at the surface of the rotor σ_1, and at the surface of the stator σ_0, for the three rotor diameters. The range in values of torque W is from the maximum that has been used, to a minimum taken arbitrarily at about 30 times the friction torque. The depths of immersion in table 1 are reasonable values for the two lengths of rotor.

TABLE 1.—*Values of shear stress at rotor and stator surfaces*

Torque W	Rotor diameter $2a_1$	Depth of immersion h	Shear stress at rotor surface σ_1	Shear stress at stator surface σ_0
dyne-cm	*cm*	*cm*	*dyne/cm²*	*dyne/cm²*
8×10^5 to 4×10^7	3.50	15	2.8×10^3 to 1.4×10^5	2.4×10^3 to 1.2×10^5
8×10^5 to 4×10^7	2.22	7.5	1.4×10^4 to 6.9×10^5	4.7×10^3 to 2.3×10^5
8×10^5 to 4×10^7	0.794	7.5	1.09×10^5 to 5.4×10^6	4.7×10^3 to 2.3×10^4

The sensitivity of the apparatus may be characterized by the ratio of angular rotation of the rotor system per unit torque to compliance of the material. If J_e is the steady-state elastic compliance and if θ_r is the maximum recovery angle in radians, then

$$\frac{\theta_r}{WJ_e}=\frac{1/c^2-1}{4\pi h a_0^2} \tag{1}$$

where h and a_0 are the depth of immersion and the stator radius, and c is the ratio of the rotor diameter to stator diameter. The numerator of the right-hand side ranges from 22 (for the smallest rotor) to 0.2. The practicable range of values of J_e may be estimated by taking reasonable values of θ_r and h equal to 0.2 radian and 7.5 cm, respectively. In table 2 this range is obtained from eq (1) for the largest diameter rotor with the lower limit of the torque in table 2 and for the smallest diameter rotor with the upper limit of torque. From table 2 it is seen that the instrument is suitable for measurement of values of J_e in the range 10^{-4} cm²/dyne to 10^{-7} cm²/dyne.

Fiduciary marks in the form ot circles are scribed on the cylindrical portion of each rotor and are located at exactly 8.89 cm and 16.193 cm from the plane base for the short and long rotor respectively. These marks are required in the case of the long rotors and are helpful with the short rotors for the measurement of depth of immersion, which is accomplished by means of a traveling microscope.

3.2. Torque Application and Release

Details of the arrangement for applying and releasing a constant torque are shown in figure 4. The three lower solenoids in figure 2 actuate the drum-arresting ring C in figure 4; coil springs normally hold this ring against upper stops. The solenoids are first energized by closing the switch F. The push-button

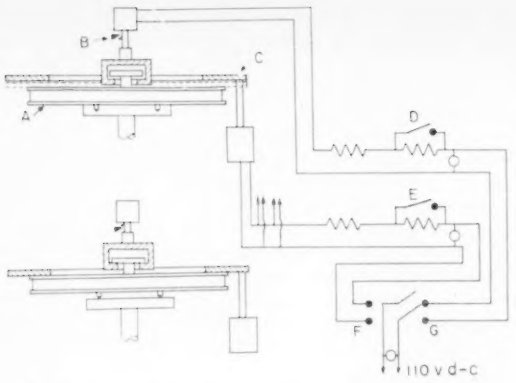

FIGURE 4. *Torque drum arrest and removal device.*
A, Torque drum; B, Catch; C, Drum arresting ring; D, E, F, G, Switches.

E provides a momentary overload which pulls the ring C against the springs into contact with the torque drum A; the weights are then hung from the cords. The contacting surfaces are provided with friction materials, so that the pressure of the ring C on the drum A prevents rotation of the drum. When the switch F is opened, the ring C is returned by the springs as shown in the upper diagram in figure 4, and the drum is thus released. When it is desired to remove the torque, the upper solenoid is similarly energized by the switch G in figure 4. When the overload button D is pressed momentarily, the drum A is pulled off the shaft, and held against the ring C as shown in the lower diagram in figure 4; the friction surfaces again prevent rotation of the torque drum. The rotor system is now free from torque, and retarded elastic recovery can take place. After the weights are removed, the upper solenoid is deenergized. The catch B in figure 3 holds the drum clear of the rotor. The frame carrying the load application and release mechanism is supported on a flange resting on the stationary cup of the mercury seal. This frame together with the torque drum can be easily removed after opening the connectors in the solenoid leads.

The ten-inch diameter torque drum is interchangeable with a drum of 2.5 in. diameter; the necessity for the latter drum can be shown by the following considerations. It has previously been shown that in order to obtain the limiting value of $J(t)-t/\eta$, it is necessary for the preceding flow test to be of duration of the order of 10^{-3} η seconds for low molecular weight polyisobutylene [1]. The same coefficient applies to a series of blends of polyisobutylene fractions in the same molecular weight range [11], and also to a high molecular weight polyisobutylene of the order of one million molecular weight. Thus, if R is the drum radius, W the torque and h the depth of immersion, the distance δ descended by the weights to reach the steady state is given approximately by:

$$\delta = \frac{10^{-3} WR}{\pi h}\left[\frac{1}{4a_1^2} - \frac{1}{4a_0^2}\right] \qquad (2)$$

where $2a_1$ and $2a_0$ are the rotor and stator diameters respectively. Taking h equal to 7.5 cm and W equal to the minimum practicable torque of 8×10^5 dyne-cm, it is found from eq (2) that for the 10-in. diameter drum, δ is equal to 650 cm, 60 cm, and 5 cm, for the small, intermediate, and large diameter rotors, respectively. The maximum range in δ is 120 cm; thus only a small range in values of W is possible for the intermediate size rotor. For the smaller drum the above values of δ are divided by four, and hence a wider range of values of W becomes available for the intermediate size rotor. In order to obtain a range in values of W for the smallest rotor, an even smaller drum and possibly a considerably smaller stator tube would be required.

3.3. Autographic Recording System

The recording system is shown diagrammatically in figure 5. The angular position of the rotor as a function of time is traced on the chart of a slightly modified photoelectric recorder.[3] On the rotor shaft

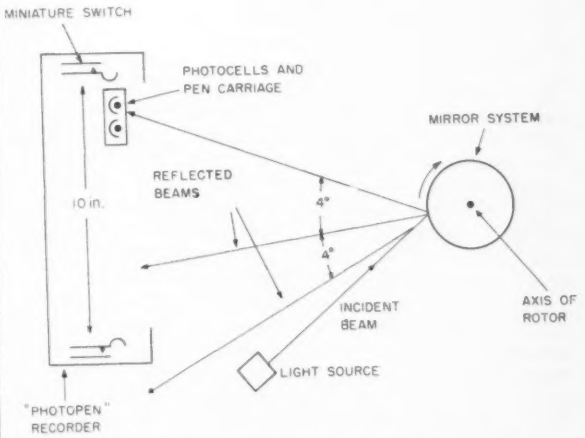

FIGURE 5. *Diagrammatic view of optical recording system.*

are two banks of mirrors; each bank comprises 45 plane, plated, and polished surfaces of a brass block, normals to adjacent surfaces subtending an angle of 8° with each other. The two banks are staggered symmetrically to each other. The mirrors serve to reflect the incident light beam from an adjacent light source on to the pair of photocells on the pen carriage of the recorder. The distance of the recorder from the viscometer is such that 4° rotation of the rotor corresponds to nearly the full chart width of ten inches. This arrangement permits continuous recording of the angular displacement of the rotor.

[3] Beckman "Photopen". National Technical Laboratories, South Pasadena, Calif.

The recorder has been modified so that a continuous record of flow or recovery can be obtained with either continuous or intermittent chart drive. The continuous record is obtained by means of miniature switches at each end of the pen-carriage travel. When the carriage actuates the appropriate miniature switch, the light source is momentarily extinguished, and the pen carriage is caused to travel back until it picks up the next beam. The time for total return of the carriage is about two seconds, thus even if transfer from one beam to the next takes place during the initial rapid recovery, little or no extrapolation is required.

It is desirable, following the initial rapid recovery, to slowdown the speed of the chart, which travels normally at 1 in. per minute. This is done by an intermittent chart drive, which moves the chart for 1 min. in each hour. The device consists of three cams driven at 1 revolution per hour by a synchronous motor. By means of miniature switches the cams switch on and off in the appropriate sequence the light source, servoamplifier of the recorder, and chart drive. The changeover from continuous to intermittent chart drive can be preset by means of a timing clock. This clock, together with the reversal switch for controlling the direction of continuous recording and the switches for application and removal of torque, are mounted in the recorder stand.

Calibration of the recording system was made by measuring the distance travelled by the pen carriage of the recorder when moved from 1 reflected light beam to the adjacent beam, with the rotor stationary. This was done for a total of 97 successive displacements, the rotor system being moved by hand. In this way 360° rotation of the rotor was found to correspond to a total pen-carriage displacement of 778.77 in., thus 1 in. displacement on the chart was equivalent to 0.462° rotation of the rotor. Large angular velocities were obtained from measurement in the chart travel direction of the distance between alternate traces, corresponding to reflections from adjacent mirrors on the same bank, thus giving the time for a nominal rotation of 8°. In the previous measurements the sum of successive pairs of displacements was found to vary from 17.22 to 17.45 in., with a mean of 17.31 in. There is seen to be no necessity for the two banks of mirrors to be staggered precisely at 4° to each other.

The recording system displayed no measurable drift over several hours, thus justifying measurements of elastic recovery over extended periods of time with a balanced photocell arrangement.

4. Performance

Measurements of the friction of the rotor system, end effect calibration, and corrections for instrument compliance and temperature gradient in the test material will be discussed.

4.1. Instrument Friction

In figure 6 are shown some measurements of angular velocity Ω as a function of torque W using a Newtonian liquid, namely, commercial hydroabietyl alcohol, which has a viscosity of about 10^6 poises at 12 °C. It is seen that for all cases, the angular velocity is proportional to $(W-W_f)$, where W_f is the friction torque equal to about 2.5×10^4 dyne-cm, and is independent of temperature, depth of immersion h, rotor diameter $2a_1$, and end clearance d. The circles, squares, and diamonds in figure 6 show the effect of varying respectively the rotor diameter, depth of immersion, and temperature. Thus in measurements of flow behavior, the instrument friction is simply accounted for by taking the effective torque as $(W-W_f)$. The effect of friction on elastic recovery measurements is more complicated and is considered in section 7.

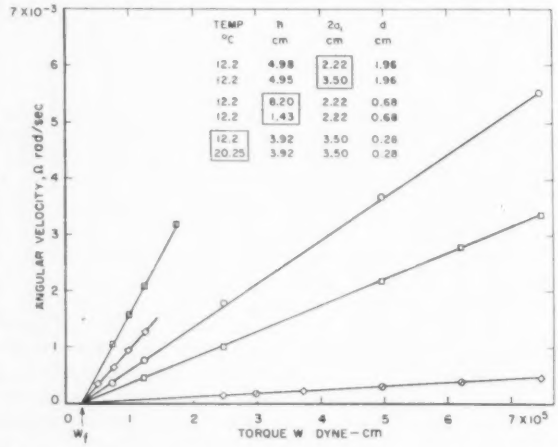

FIGURE 6. *Angular velocity versus torque*; h, *depth of immersion;* $2a_1$, *rotor diameter; and* d, *end clearance.*

4.2. Instrument Constant and End-Effect

It is desired to obtain the instrument constant for the steady flow of a Newtonian liquid in the viscometer. This instrument constant K may be defined as the ratio of $\Omega\eta$ to effective torque $(W-W_f)$ for any given geometry, where η is the viscosity of the liquid. The same instrument constant is applicable for a material manifesting linear viscoelastic behavior, provided that inertia effects can be ignored [8].

The viscoelastometer has been operated with a pool of mercury in the base of the stator, the surface of the mercury extending above the plane surface of the rotor. The test material is floating on the mercury and is located entirely in the annular space between the cylindrical surfaces of the stator and rotor. Under these circumstances the motion of the particles in the test liquid is the same as in a portion of a Couette-type viscometer of infinite length. For this arrangement the instrument constant is then given by:

$$K=\frac{\Omega\eta}{W-W_f}=\frac{1-c^2}{4\pi a_1^2 h}. \tag{3}$$

In eq (3) it is, of course, assumed that the torque due to the mercury is negligible compared to that due to the test liquid.

More usually, the test liquid occupies the space between the plane ends of the rotor and stator, together with the adjoining portion of the annular space between the cylindrical surfaces. Under these circumstances, the torque on the cylindrical portion is modified, and there exists a torque on the plane base of the rotor. For this arrangement it is reasonable to assume that the instrument constant is given by:

$$K=\frac{\Omega\eta}{W-W_f}=\frac{1-c^2}{4\pi a_1^3\left(\frac{h}{a_1}+\frac{\Delta h}{a_1}\right)} \tag{4}$$

where $\Delta h/a_1$ is independent of h/a_1 for sufficiently large values of the latter ratio; $\Delta h/a_1$ thus is a function of two independent geometrical parameters such as c and d/a_1, where d is the distance between the plane ends of the rotor and stator.

The justification for this assumption for a particular geometry is given by the data in figure 7, which shows plots of $(W-W_f)/\Omega$ against h for the intermediate diameter rotor ($2a_1=2.22$ cm) for different values of end clearance, using hydroabietyl alcohol at 12.2 °C as the test liquid. The data for five values of d are fitted statistically to a series of straight lines of the same slope. The results with the smallest end clearance, represented by the broken line in figure 7, were erratic and were not used in calculating the intercepts and best slope.

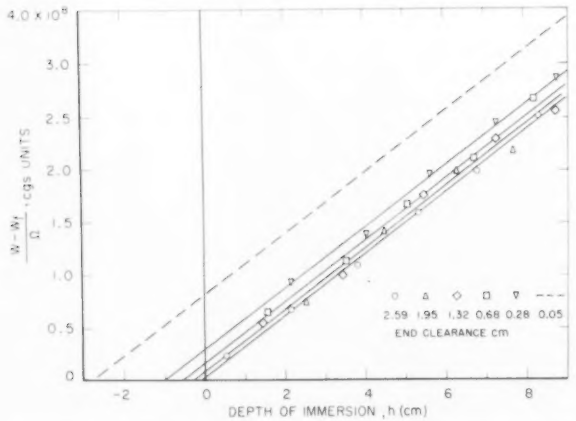

FIGURE 7. *(Effective torque)/(angular velocity) versus depth of immersion for several values of end clearance.*

The "end effect" Δh is the negative of the intercept on the abscissa.

The results of the end-effect measurements are shown nondimensionally in figure 8, where the ratios of end effect to rotor diameter, $\Delta h/2a_1$, are plotted as circles against the ratios of end clearance to rotor diameter. The points appear to fall on a rectangular hyperbola; this is demonstrated by the plot also given in figure 8 of $2a_1/\Delta h$ against $d/2a_1$, in which the results of the observations are represented as squares; the points are seen to fall on a straight line passing through the origin. A crude theory of end effect can be proposed, in which it is assumed that the torque on the cylindrical portion of the rotor is the same as on the same length of infinite rotor, and that the torque on the plane base is the same as that on a circle of the same diameter which forms part of an infinite plate in a rotating disk viscometer. This theory predicts that $2a_1/\Delta h$ is proportional to $d/2a_1$, as shown by the broken line in figure 8. The end effect is seen to be much greater than that predicted by this crude theory.

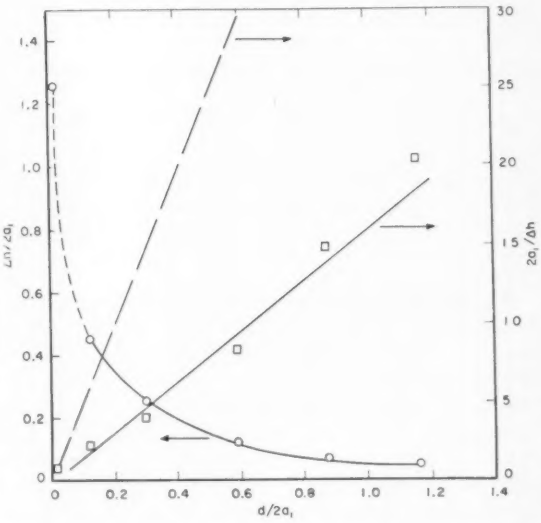

FIGURE 8. *End effect measurements* ○, $\Delta h/2a_1$ versus $d/2a_1$; □, $2a_1/\Delta h$ versus $d/2a_1$. *The broken straight line represents the results of an elementary theory.*

Similar measurements have been made using the large rotor. However, the plot of $(W-W_f)/\Omega$ against h gave very erratic data from which no conclusions could be drawn.

The only significant data in the literature relevant to this end-effect study are due to Wadleigh [12]. For a value of c equal to 0.290, these results agree with the empirical relationships:

$$\frac{2a_1}{\Delta h}=0.64+0.275\,\frac{d}{2a_1}$$

for a range of values of $d/2a_1$ from unity to four.

4.3. Instrument Compliance

The instrument compliance has been measured using hydroabietyl alcohol, cooled below its glass transition, as the test liquid. The rotation of the mirror system as measured by displacement of the trace on the recorder chart was observed for removal of a given torque on the rotor following the usual procedure. The angular rotation was found to be proportional to torque, leading to a compliance of 0.97×10^{-10} radian/dyne-cm. This includes the contribution of the compliance of the hydroabietyl alcohol. Assuming a value of shear modulus of 10^{10} dynes/cm^2 for glassy hydroabietyl alcohol, this contribution is found to be 0.95×10^{-13} radian/dyne-cm. Hence the apparatus compliance C may be taken as 0.97×10^{-10} radian/dyne-cm. These data were obtained using the large-diameter (3.50 cm) rotor; it is assumed that the instrument compliance is the same for the intermediate diameter (2.22 cm) and small (0.79 cm) rotors.

The correction ΔJ due to instrument compliance to be subtracted from the material shear creep compliance calculated from the observed value of (θ/W) is

$$\Delta J=\frac{\pi(h+\Delta h)C}{\left(\frac{1}{4a_1^2}-\frac{1}{4a_0^2}\right)}=\frac{C}{K}. \tag{5}$$

For example, assuming $(h+\Delta h)$ equal to 7.5 cm, then for the intermediate diameter rotor ($2a_1=2.22$ cm), ΔJ is equal to 1.7×10^{-8} cm^2/dyne; for the small diameter rotor (0.79 cm), ΔJ is equal to 1.5×10^{-9} cm^2/dyne.

Thus even with the smallest rotor, it is not possible to measure the lower limiting value J_g of the shear creep compliance of an amorphous polymer. Since this compliance is of the order of 10^{-10} cm^2/dyne, it would be masked by the instrument compliance. However, it would be possible to measure such small values of shear compliance by changing the instrument to an arrangement in which rods of circular or rectangular cross sections are twisted. For example, the compliance of a rod of length 10 cm, diameter 2 cm, and shear modulus 10^{10} dynes/cm^2 is 6.4×10^{-10} radians/dyne-cm; this is considerably greater than the instrument compliance.

4.4. Temperature Gradient Correction

As a result of thermal conductivity along the rotor shaft, the temperature of the rotor is slightly different from that of the thermostat. Measurements of the difference between the rotor temperature T_1 and the bath temperature T_0 show that this difference ΔT (equal to T_0-T_1) varies linearly with bath temperature over a wide range of temperature. Except for natural rubber, there do not appear to exist published data on the thermal conductivity of linear polymers in the liquid state. The thermal conductivity of the Pyrex glass of the stator tube is greater by a factor of seven than the thermal conductivity of natural rubber (at room temperature). It is reasonable to assume the thermal conductivities of linear nonpolar polymers in the liquid state are very similar, and therefore that the temperature of the inside wall of the stator is close to that of the bath, for arrangements with the intermediate and small diameter rotors. It is reasonable to assume also that the temperature in the test liquid varies linearly with the radius. If ΔT is small, then the viscosity of the test liquid varies approximately linearly with radius. With these assumptions, the effect has been calculated of the temperature gradient on steady flow, and also on displacement of the time scale for elastic recovery.

Let η_1 be the viscosity of the liquid at the surface of the rotor, corresponding to temperature T_1, and let η_1 $(1-k')$ be the viscosity at the surface of the stator, corresponding to temperature T_0. Let Ω_0 be the angular velocity for a given torque if the temperature is uniform, and the viscosity and temperature are respectively η_1 $(1-k')$ and T_0. Let Ω_a be the angular velocity for the same torque with the temperature gradient. It can then be shown that

$$\frac{\Omega_a}{\Omega_0}=1-\frac{k'a_0}{a_0+a_1}. \tag{6}$$

For many polymers the coefficient k' can be calculated from known viscosity-temperature relations. Except in the vicinity of the glass transition, the viscosity η at temperature T is related to the viscosity η_1 at temperature T_1 by the expression [13]:

$$\log\left(\frac{\eta}{\eta_1}\right)=A\left(\frac{1}{T^m}-\frac{1}{T_1^m}\right).$$

Then:

$$k'=2.3\ mA\Delta T/T_1^{m+1}. \tag{7}$$

TABLE 2. *Values of J_s for elastic recovery of 0.2 radian, with 7.5 cm depth of immersion*

Torque, W	Rotor diameter $2a_1$	J_s
dyne-cm	*cm*	*cm²/dyne*
8×10^5	3.50	4.5×10^{-8}
4×10^7	0.79	7.8×10^{-9}

From about the glass transition temperature to 100 ° C above this temperature, the viscosity may be represented by a modified form of the Williams-Landel-Ferry relation [13, 14, 15]:

$$\log\left(\frac{\eta_1}{\eta}\right)=\frac{900(T-T_1)}{c_2(c_2+T-T_1)} \tag{8}$$

where c_2 is an adjustable parameter. For this case,

$$k'=2.3\left(\frac{900\ \Delta T}{c_2^2}\right). \tag{9}$$

Now let η_a be the apparent viscosity measured in the viscoelastometer with the temperature gradient. Then from eq (6) the viscosity η_0 for an isothermal viscometer at temperature T_0 is given by:

$$\left.\begin{aligned} \eta_0 &= \eta_a\left(1-\frac{k'a_0}{a_0+a_1}\right) \\ \text{and } \log \eta_0 &= \log \eta_a - \frac{k'a_0}{2.3(a_0+a_1)}. \end{aligned}\right\} \quad (10)$$

Let t_a be the time to reach a specified angular deformation in a creep or recovery experiment in the viscoelastometer with temperature gradient, and let t_0 be the time to reach the same deformation in an isothermal viscoelastometer at temperature T_0. Then

$$\log t_0 = \log t_a - \frac{k'a_0}{2.3\,(a_0+a_1)}. \quad (11)$$

Equations (6), (10), and (11) give the corrections to angular velocity, viscosity, and logarithms of recovery times due to temperature gradient. Thus if ΔT and therefore k' is positive, the logarithmic time scale for elastic recovery corrected to temperature T_0 is obtained by reducing the observed logarithmic time scale by an amount $k'a_0/2.3\ (a_0+a_1)$.

5. Method of Operation

Different filling procedures to obtain bubble-free specimens are used according to whether the material is in the glassy state at room temperature (for example, polystyrene), or is a high molecular weight liquid (for example, polyisobutylene, M_w equal to 1.56×10^6, viscosity at 25 °C about 10^{11} poises) or a low molecular weight polymeric liquid (for example, polyisobutylene, M_v equal to 4.1×10^4, viscosity at 25 °C about 10^6 poises).

In the first case a cylindrical plug is molded, such that the diameter at room temperature is just less than the bore of the stator. The plug is inserted in the bottom of the stator. The whole rotor system is raised so that the tube can be inserted from below as previously described. The Dewar vessel is raised into position from below and the thermostat is set to a temperature corresponding to a viscosity of the polymer in the range 10^7 to 10^8 poises. The rotor system is then released, so that the foot of the rotor presses on the upper surface of the polymer because of the weight of the rotor system. After a period of time of the order of one week, the rotor system has sunk to the limit of its travel, so that its weight is now carried through the gage blocks by the collar at the top of the stator tube. The collar that clamps the stator tube and rotor system to the support ring is finally tightened. A similar procedure has been used in the case of high molecular weight polyisobutylene. In this case an appropriate molding procedure must be used; otherwise air bubbles will appear gradually in the interior of the specimen following removal from the mold.

In the case of a low molecular weight polymer, air is unavoidably entrapped in the material as it is placed on the bottom of the stator. It is therefore heated to reduce its viscosity to 10^5 poises or less, so that the larger air bubbles can rise at a significant rate. When only small air bubbles remain, the rotor system is allowed to sink into position. Tests have been carried out on a low molecular weight polymer in which the stator tube was first filled with an appropriate amount of mercury. When the rotor system was in position, the foot of the rotor was below the mercury surface, and the polymer was in the form of an annulus floating on the mercury.

In carrying out an experiment to measure elastic recovery, the load is applied as discussed earlier. At the appropriate time for load removal the switch reversing the direction of automatic return of the pen carriage is actuated, and the load removed as previously described, just before the pen carriage reaches the limit of its travel. When the recovery has become sufficiently slow, the chart drive is changed from continuous to intermittent motion.

6. Data Reduction for Nonlinear Behavior

The shear stress on a cylindrical annulus varies inversely as the square of the radius. In the region of nonlinear behavior, under suitable conditions, secondary flow is negligible, and it is desired to obtain the behavior in simple shear from the flow and recovery behavior of a material in the viscoelastometer.

It has been mentioned previously that in order to avoid the Weissenberg effect, the maximum measurable apparent fluidity is limited to about twice the zero shear fluidity. Over this range it usually appears that Ω/W varies linearly with W. This is consistent with the empirical Ferry flow law

$$\left(\frac{1}{\eta_a}\right)=\left(\frac{1}{\eta_0}\right)(1+\sigma/G_i) \quad (12)$$

where $(1/\eta_a)$ is the ratio of rate of shear to shear stress σ in simple shear, $(1/\eta_0)$ is the (Newtonian) fluidity, and G_i is a constant (for a given material at a given temperature). If we define a Couette viscosity η_c for a non-Newtonian liquid as that quantity obtained by inserting observed values of Ω and W in the Couette formula, eq (3), with appropriate corrections for Ω, W, and h, then:

$$\left(\frac{1}{\eta_c}\right)=\left(\frac{1}{\eta_0}\right)\left[1+\frac{\sigma_1(1+c^2)}{2G_i}\right]. \quad (13)$$

Thus η_0 and G_i may be obtained conveniently from a plot of $(1/\eta_c)$ against σ_1.

In the general case, this plot is nonlinear, and a method due to Pawlowski [10] is suitable for the determination of the flow behavior in simple shear

using a rotational viscometer, when c is not near unity. Let the rate of shear corresponding to a simple shear stress σ be $f(\sigma)$. Then

$$\Omega=\frac{1}{2}\int_{c^2\sigma_1}^{\sigma_1}\frac{f(\sigma)}{\sigma}\,d\sigma \tag{14}$$

where σ_1 and $c^2\sigma_1$ are the shear stresses at the surface of the rotor and stator walls respectively, and Ω is the corresponding angular velocity. For a particular value of σ_1 equal to k; we obtain from eq (14):

$$2\sigma_1\frac{d\Omega}{d\sigma_1}\Big|_{\sigma_1=k}=[f(\sigma)-f(c^2\sigma)]_{\sigma=k}.$$

If now the torque is reduced in the ratio c^2, the corresponding angular velocity is given by:

$$2\sigma_1\frac{d\Omega}{d\sigma_1}\Big|_{\sigma_1=c^2k}=[f(\sigma)-f(c^2\sigma)]_{\sigma=c^2k}.$$

Hence

$$f(\sigma_1)\Big|_{\sigma_1=k}=2\left\{\sigma_1\frac{d\Omega}{d\sigma_1}\Big|_{\sigma_1=k}+c^2\sigma_1\frac{d\Omega}{d\sigma_1}\Big|_{\sigma_1=c^2k}+\cdots\right\} \tag{15}$$

Thus if Ω is plotted against σ_1, the terms in the brackets on the right hand side are the intercepts AB,CD, etc., as in figure 9; the rate of shear at the surface of the rotor is given by twice the sum of these intercepts.

It is of course necessary to carry the graphical summation only down to a shear stress k^*, below which the flow behavior is substantially Newtonian. The remainder is then

$$\frac{2k^*}{1-c^2}\frac{d\Omega}{d\sigma_1}\Big|_{\sigma=k^*}.$$

This method can be extended to the case of nonlinear viscoelasticity. Assume that a simple shear stress σ is applied at infinite negative time and removed at zero time. Let the decrease in shear strain from zero time to a subsequent time t be $J\sigma(t,\sigma)$. In the case of nonlinear behavior $J(t,\sigma)$, which we will call the recovery compliance, is a function of σ. If now in a rotational viscometer the shear stress at the surface of the rotor with a given constant torque is σ_1, the angular recovery $\theta(t,\sigma_1)$ at a time t following removal of torque is given by

$$\theta(t,\sigma_1)=\frac{1}{2}\int_{c^2\sigma_1}^{\sigma_1}J(t,\sigma)\,d\sigma. \tag{16}$$

The recovery compliance at time t corresponding to a particular value of σ_1 equal to k is given by

$$J(t,\sigma)\Big|_{\sigma=k}=2\left[\frac{d\theta(t,\sigma_1)}{d\sigma_1}\Big|_{\sigma_1=k}+\frac{c^2d\theta(t,\sigma_1)}{d\sigma_1}\Big|_{\sigma_1=c^2k}+\cdots\right]. \tag{17}$$

Thus the recovery behavior in simple shear is obtained from measurements of angular recovery as a function of σ_1.

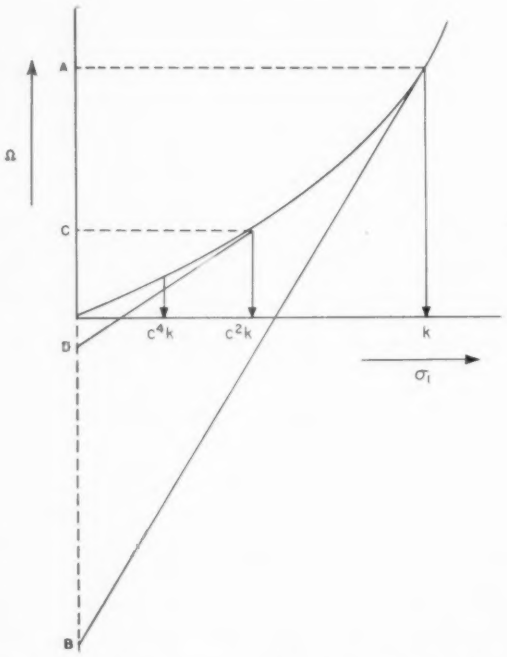

FIGURE 9. *Graphical method of obtaining rate of shear as function of shear stress from plot of angular velocity Ω versus shear stress σ at surface of rotor.*

7. Effects of Inertia and Friction on Recovery

The effects of the inertia and friction of the rotor system on the observed retarded elastic recovery will now be considered. A dynamic representation of the viscoelastometer system is given in figure 10(a). For the purpose of the present discussion the springs representing instrument compliance and glass compliance of the material may be omitted, as in figure 10(b). In the models of figure 10 there is represented to a first approximation the viscoelastic behavior of the liquid under conditions where this behavior is linear; a more exact representation is obtained, of course, by adding further Voigt elements with different retardation times τ_i. The direction of the frictional torque W_f is such as to oppose the deformation of the material.

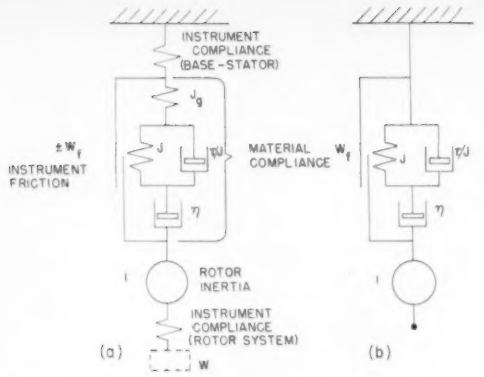

FIGURE 10. *(a) Dynamic representation of viscoelastometer system. (b) Mechanical model for retarded elastic recovery with instrument friction and inertia.*

We assume that a constant torque W is first applied to the system until the steady state is reached, and then instantaneously removed. Just before this instant the spring in figure 10(b) is stretched, and the upper dashpot is stationary; the lower dashpot is extending at a uniform rate. On the removal of the external torque W there occurs a transient loading of the material due to rotor inertia. In addition, contraction of the spring results in a load corresponding to the friction torque W_f, which leads to a steady extension of the lower dashpot. When the rate of contraction of the spring equals the rate of extension of the lower dashpot, contraction of the three-element model representing the material ceases, and relaxation thereafter takes place at constant deformation.

The portion of the record corresponding to removal of load is always "sharp-edged"; there is no perceptible rounding-off due to inertia of the system. The inertia loading on the material can thus be considered as a "spike" of very short duration. The residual elastic deformation of the Voigt element is negligible for times that are long compared to the duration of this spike; there remains to be considered the effect of this transient loading on the flow of the system. This reduces to an apparent material compliance ΔJ. Let I be the moment of intertia of the rotor system, and let $-\omega_1$ and ω_2 be the angular velocities just before and just after removal of torque W. It can then be shown that

$$\Delta J = I(\omega_1+\omega_2)/W\eta. \tag{18}$$

If reasonable values of the parameters are assumed, it appears that ΔJ is negligible for the present viscoelastometer.

In order to estimate the effect of instrument friction on elastic recovery, we will assume as before that the material manifests linear viscoelastic behavior; it can be represented for example by a model consisting of a series of Voigt elements in series with a dashpot. This is loaded by a friction element which exerts a constant torque W_f opposing the direction of deformation of the material. Now let $\theta(0)$ represent the angular position of the rotor at the instant of torque removal, and let $\theta(t)$ be the position at a subsequent time t. If W is the external torque that is removed and if $J(t)-t/\eta$ is the elastic part of the shear creep compliance, it can be shown that

$$J(t)-t/\eta = \frac{\theta(0)-\theta(t)}{K(W-2W_f)} + \left(\frac{W_f}{W-2W_f}\right) t/\eta. \tag{19}$$

The second term results from reduction in recovery due to the flow of the material under the friction load. The instrument constant K is given by:

$$K = \frac{(1-c^2)}{4\pi a_1^2(h+\Delta h)} \tag{20}$$

taking end-effect into account. The previous assumptions lead to cessation of recovery at a time t given approximately by:

$$L(\tau)|_{\tau=t} \simeq \frac{W_f t}{(W-2W_f)\eta} \tag{21}$$

where $L(\tau)|_{\tau=t}$ is the value of the retardation spectrum when τ is equal to t. This analysis assumes that the frictional torque for very small values of angular velocity is the same as that measured for more rapid rates of rotation, as in figure 6. At small angular velocities it appears that W_f can be quite variable, which makes the second term in eq (19) somewhat uncertain. The best estimate of the steady state of shear compliance is thus made by evaluating $J(t)-t/\eta$ by means of eq (19) up to the time corresponding to that at which recovery ceases, and then extrapolating to zero slope on a logarithmic time plot.

In the case of nonlinear behavior the calculation of the effect of friction on retarded elastic recovery becomes more difficult. The observed angular recovery $\theta_0\ (t,\ \sigma_1)$ at a time t following removal of an effective torque $W-W_f$ is less than the "ideal" recovery $\theta\ (t,\ \sigma_1)$ which would be obtained in the absence of a frictional torque W_f opposing the recovery.

If we define a Couette recovery compliance $J_c\ (t,\ \sigma_1)$ corresponding to recovery in a frictionless viscometer following flow in which the shear stress at the rotor is σ_1 (equivalent to an effective torque $W-W_f$), then

$$J_c(t,\sigma_1) = \frac{\theta(t,\sigma_1)}{K(W-W_f)}. \tag{22}$$

If it is assumed that the reduction in recovery at time t is equal to the angular displacement due to a small torque W_f applied at zero time, then

$$\theta(t,\sigma_1)-\theta_0(t,\sigma_1) = W_f K J_r(t,0) + W_f K t/\eta_0 \tag{23}$$

where $J_r\ (t,\ 0)$ is the elastic part of the shear creep compliance at very small shear stresses, and η_0 is

the Newtonian viscosity. Combining eqs (22) and (23), we obtain:

$$\frac{\theta_0(t,\sigma_1)+W_fKt/\eta_0}{K(W-2W_f)}=\frac{(W-W_f)J_c(t,\sigma_1)-W_fJ_r(t,0)}{(W-2W_f)}. \tag{24}$$

As W approaches $2W_f$, the right-hand side of eq (24) is seen to approach J_r $(t, 0)$, thus eq (23) becomes:

$$\theta(t,\sigma_1)-\theta_0(t,\sigma_1)=W_fKt/\eta_0 + W_fK \lim_{W\to 2W_f}\left[\frac{\theta_0(t,\sigma_1)+W_fKt/\eta_0}{K(W-2W_f)}\right]. \tag{25}$$

The nonlinear retarded elastic recovery in simple shear is then obtained using eq (17).

Reversal of retarded elastic recovery. According to the theory of linear viscoelasticity, if the viscoelasticity is only of the relaxational type that can be represented by models consisting only of springs and dashpots, then the elastic part of the creep compliance, $J(t)$-t/η, is a function increasing monotonically with time, as in figure 11. This function reaches an asymptotic limit at infinite time; this limit can be assumed to be reached in a frictionless instrument at a finite time which depends upon the sensitivity of the recorder.

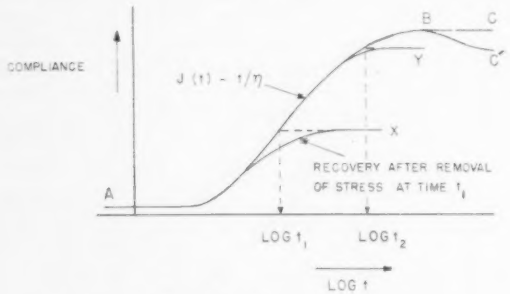

FIGURE 11. *Reversal of retarded elastic recovery.*

Let us assume that the point B in figure 11 corresponding to a time t_3 represents the limit of observability. Then the observable curve is as ABC where the curve beyond B is parallel to the abscissa, and BC represents the apparent asymptote. If recovery observations are made following a time under stress equal or greater than t_3, then these observations should give the curve ABC. If the stress is removed at an earlier time t_1, in figure 11, then the recovery curve is as shown by AX. The total recovery is equal to the elastic component of the deformation at time t_1. If the stress is removed at a later time t_2, then the elastic component corresponding to the asympotote of the curve AX is increased. It is found that if the time under load in the rotational viscometer is sufficiently long, the recovery curve does not tend to an observationally limited asymptote BC, but shows a reversal of the direction of creep recovery as represented by BC′.

This behavior has been observed in a specimen of polystyrene under conditions where the flow and early part of the recovery were linear with torque; the effect became much more marked with increase in torque. It has been observed in a specimen of polyisobutylene in which the foot of the rotor was immersed in mercury. Thus this phenomenon cannot be accounted for by nonlinearity in viscoelastic behavior, by instrument friction, or by secondary flow in the region of the plane ends.

This effect has been previously observed in measurements of the shear creep and recovery in a rotational viscoelastometer on a specimen of asphalt [16]. The instrument was a narrow-gap conicylindrical viscometer, and the viscoelastic behavior was linear and nonthixotropic over the range of the reported data. As in our experiments on polystyrene, the amount of reversal in recovery became much greater with increase in shear stress, and the time corresponding to the maximum recovery was reduced with increase in shear stress. The elastic recovery curves on asphalt were obtained by measuring the total recovery as for example at X or Y following a time under stress equal to t_1 or t_2 in figure 11. Unless one postulates the existence of a nonlinear resonance type viscoelastic behavior superimposed upon a linear relaxation type behavior, no explanation can be given for the existence of this phenomenon observed in the two viscoelastometers with linear polymers and with asphalts. Until this behavior can be accounted for, further uncertainty is added to the interpretation of observed angular recovery data.

8. Nomenclature

$J(t)-t/\eta$ = elastic part of shear creep compliance.
J_g = glass compliance.
σ_1 = shear stress at surface of inner cylinder (rotor).
σ_0 = shear stress at surface of outer cylinder (stator).
$2a_1$ = rotor diameter.
h = depth of immersion.
W = torque.
$2a_0$ = stator diameter.
c = ratio of diameters = a_1/a_0.
J_e = steady-state elastic compliance.
θ_r = total recovery angle.
η = viscosity.
R = radius of torque drum.
d = "end clearance" between plane ends of stator and rotor.
W_f = friction torque.
Ω = angular velocity.
K = instrument constant.
Δh = "end-effect".
C = apparatus compliance.
T_1 = rotor temperature.
T_0 = bath temperature.
η_1 = viscosity at rotor surface.
$\eta_1(1-k')$ = viscosity at stator surface.
Ω_0 = angular velocity of isothermal viscometer.
Ω_a = angular velocity of viscometer with temperature gradient.
$1/\eta_a$ = apparent fluidity in simple shear.
$1/\eta_0$ = Newtonian fluidity ($\equiv 1/\eta$).
η_c = Couette viscosity.
k = value of σ_1 for specified torque.
$J(t,\sigma)$ = recovery compliance (in simple shear, stress σ, recovery time t).
$\theta(t,\sigma_1)$ = angular recovery at time t.

9. References

[1] H. Leaderman, R. G. Smith, R. W. Jones, J. Polymer Sci. **14,** 47 (1954).

[2] T. L. Smith, J. Polymer Sci. **20,** 89 (1956); Trans. Soc. Rheol. **2,** 131, (1958).

[3] H. Leaderman, Elastic and creep properties of filamentous materials, (Textile Foundation, Washington, 1943).

[4] See for example:
(a) B. Gross, Theories of viscoelasticity, (Herrmann et Cie., Paris, 1953).
(b) A. J. Staverman, F. Schwarzl, Linear deformation behavior of high polymers. Chapter in H. A. Stuart, ed. Die Physik der Hochpolymeren, vol. IV, (Springer, Berlin, 1956).
(c) H. Leaderman, Viscoelasticity phenomena in amorphoud high polymeric systems, Chapter in F. R. Eirich, ed., Rheology, theory and applications, vol. II (Academiic Press, New York, N.Y., 1958).

[5] I. L. Hopkins, R. W. Hamming, J. Appl. Phys. **28,** 906 (1957).

[6] K. Ninomiya, J. Coll. Sci. **14,** 49 (1959).

[7] See for example:
(a) S. Oka, Principles of rheometry, chapter in F. R. Eirich, ed., Rheology, theory and applications, vol. III, (Academic Press, New York, N.Y., 1960).
(b) G. Barr, Monograph of viscometry, (Oxford, 1931).

[8] H. Leaderman, J. Polymer Sci. **13,** 371 (1954).

[9] A. F. H. Ward, P. Lord, Proc. second internat. congress rheology, V. G. W. Harrison, ed., (Butterworth, London, 1954).

[10] J. Pawlowski, Koll. Z. **130,** 129 (1953).

[11] H. Leaderman, R. G. Smith, L. C. Williams, J. Polymer Sci. **36,** 233 (1959).

[12] W. H. Wadleigh, BS J. Research **11,** 65 (1933) RP577.

[13] See for example:
T. G. Fox, S. Gratch, S. Loshaek, Chapter viscosity relationships for polymers in rheology, theory and applications vol. I, F. R. Eirich, ed., (Academic Press, New York, N.Y., 1956).

[14] M. L. Williams, R. F. Landel, J. D. Ferry, J. Am. Chem. Soc. **77,** 3701 (1955).

[15] H. Leaderman, Ann. Rev. Phys. Chem. **9,** 179 (1958).

[16] R. N. J. Saal, J. W. A. Labout, J. Phys. Chem. **44,** 149 (1940).

(Paper 65C1–51).

JOURNAL OF RESEARCH of the National Bureau of Standards—C. Engineering and Instrumentation
Vol. 65C, No. 1, January–March 1961

An Ultra Low Frequency Bridge for Dielectric Measurements

Donald J. Scheiber

(October 11, 1960)

The bridge described is capable of measuring the parallel capacitance and resistance of dielectric specimens in the frequency range of 0.008 to 200 cps. It employs no earthing device and is directly connected to a three terminal oscillator. The substitution method is employed. The capabilities of the bridge are experimentally tested by measurements upon known capacitors and resistors and by comparison with results obtained using a Schering bridge near 100 cps. The apparatus is capable of accuracies previously unattained at these low frequencies. Capacitances between zero and 100 pf may be measured to an accuracy of $\pm(0.05\%+0.002$ pf) at frequencies above 5 cps. Below 5 cps the accuracy becomes $\pm[0.05\%+(0.002+2\times10^5/fR_D)$pf], where f is the frequency in cps and R_D is the equivalent resistance in ohms across the detector terminals. Conductances between 10^{-9} and 10^{-15} mhos may be measured to an accuracy of about $\pm(1\%+3f\times10^{-15}$ mhos) when $f\geq0.1$ cps. When $f<0.1$ cps the accuracy is about $\pm(1\%+2\times10^{-16}$ mhos). The dielectric constant (ϵ') of a specimen may be determined to an accuracy proportional to that of capacitance measurements. The loss index (ϵ'') may be determined to an accuracy of about $\pm(1\%+5\times10^{-4}/C_v)$ when $f\geq0.1$ cps and $\pm(1\%+3\times10^{-5}/fC_v)$ when $f<0.1$ cps. Here C_v is the vacuum capacitance of the specimen expressed in picofarads. The effects of stray impedances shunting the bridge ratio arms, are investigated. Useful modifications of the bridge are discussed.

1. Introduction

Extension of the frequency range of dielectric measurements to very low frequencies is important for several reasons. For example, direct comparison can then be made between dielectric and mechanical relaxation effects in important classes of dipolar substances, such as certain polymers, for which dynamic mechanical data is often available only in this frequency region. Related to this is the study of the connection between the dielectric relaxation behavior of an amorphous material and the onset of its glass transition, the latter being closely associated with a striking slowing down of molecular motions that is reflected in a dielectric response in the ultra low frequency region. Another example is provided by the necessity of making dielectric loss measurements over the widest possible frequency range in order to determine fully the shape of dielectric loss peaks. Such studies are extremely useful in elucidating the nature of barrier systems in dipolar crystals, and in understanding the fundamental causes of dielectric loss generally. Unfortunately, little work has been carried out in the ultra low frequency range between the short time scale d–c region and the ordinary a–c bridge region (roughly 0.01 to 20 cps). Together with the fact that it has heretofore proven difficult to simultaneously measure small capacitances and conductances, this has led to a considerable gap in our knowledge of the properties of materials, and the nature of certain molecular mechanisms.

It is also clear that our knowledge of the properties of components; e.g., multimegohm resistors, is far from complete in the ultra low frequency range. The bridge discussed here is capable of providing information of this type.

A major objective of this paper is to describe an a–c bridge that is capable of making accurate measurements of capacitance and (low) conductance between 0.01 and 200 cps, but which is neither cumbersome nor unnecessarily time-consuming to operate. The bridge described meets these requirements, and is therefore well suited for carrying out investigations on the dielectric properties of materials.

Some relevant background information will now be given in order to indicate the nature of earlier bridge designs, and certain problems that are encountered when dealing with ultra low frequency bridge measurements.

At frequencies below about 10 cps, transformer coupling of a bridge and a generator becomes ineffectual. At lower frequencies, the bridge and generator must be directly coupled. The first successful effort to measure dielectric properties down to 0.1 cps was reported by Volger, Stevels, and van Amerongen [1] [1] in 1953. These workers were primarily interested in measurements on high-loss inorganic glasses. They used a three terminal RC oscillator directly coupled to a series resistance-capacitance bridge equipped with a Wagner earthing device. A galvanometer served as the detector. Although explicit details concerning the conductance range and sensitivity are not reported, it is apparent that this arrangement is not well suited for the measurement of low conductances, and it is desirable to extend the range to lower frequencies.

In 1955, Weingarten [2] briefly described apparatus which he had employed to measure the dielectric properties of glasses down to 0.008 cps. Heroux [3]

[1] The figures in brackets indicate the literature references at the end of this paper.

also gives a description of Weingarten's bridge. This three terminal bridge employed no separate guard balancing circuit, such as a Wagner earthing device. A conductance balancing system somewhat similar to that of Cole and Gross [4] was used. The low-frequency apparatus designed by Weingarten was evidently not subjected to a thorough analysis. In particular, an investigation of the effect of impedances to ground within the generator was not given. Since the three terminal generator employed is directly coupled to the bridge, these impedances shunt the bridge's ratio arms, and therefore must not be ignored. However, as will be seen below, Weingarten's basic design is a promising one. When slightly modified and subjected to careful analysis, it permits ready use of the reliable substitution method of measurement, does not require the use of a Wagner earthing device, which is exceedingly wasteful of time at low frequencies, and yields highly accurate results in the capacitance and conductance range of principal interest after certain well-defined and straightforward corrections are applied.

Nakajima and Kondo [5] circumvent the impedances-to-ground problem by operating the generator in a two terminal manner. Their bridge (briefly described elsewhere by Nakajima and Saito [6]) utilizes a Wagner earthing device, a conductance shifter, and an ungrounded or "floating" detector. Dielectric measurements with this apparatus are carried out by the direct method. The substitution method is preferable to the direct method if precise measurements of low conductance are desired. Also, it is desirable to ground one terminal of the detector. As implied earlier, the Wagner earthing device, while sound and accurate, leads to excessive measurement times in the lower end of the frequency range (see below). Hence we chose to use Weingarten's basic design, coupled with a detailed circuit analysis.

The following example indicates why a Wagner earthing device was not employed in the ultra low frequency bridge. At 0.1 cps, using the substitution method with no earthing device, about one half hour is necessary to complete the two balances that are required. With the earthing device, four balancing operations are necessary, consuming at least one hour, even if interaction between the balances is neglected. At 0.01 cps, the use of the earthing device is outright prohibitive from the standpoint of measurement time.[2]

2. Bridge Circuit and Construction

2.1. Bridge Circuit

Figure 1 shows the circuit diagram of the bridge and the output circuit of the three-terminal generator. The values of the components used are given in table 1. In figure 1, C_x and R_x represent the parallel capacitance and resistance to be measured. R_3 and R_4 are precision wire wound, 10^5 ohm resistors. C_3 and C_4 include all capacitances to ground from the points W and Y, respectively. C_3 also includes a two terminal variable capacitor, calibrated to ± 0.1 pf over the range of 100 to 1000 pf.[3] From figure 1, it is apparent that all lead capacitances to ground within the bridge, with one exception, are either across the resistive arms and therefore included in

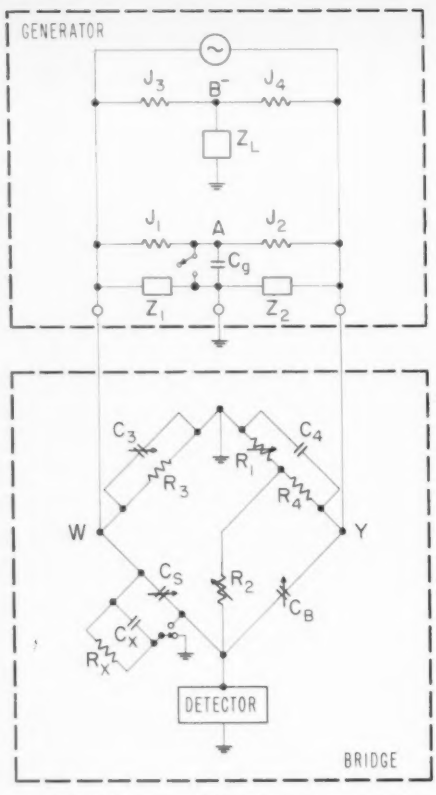

FIGURE 1. *Circuit diagram of low frequency apparatus.* Values of components are given in table 1.

TABLE 1. *Values of components in figure 1*

J_1, J_2	15.8 kohm $\pm 1\%$
J_3, J_4	15 kohm $\pm 10\%$
R_3	1.0019 x 10^5 ohms
R_4	1.0012 x 10^5 ohms
R_1	0 to 111.0 ohms in 0.1 ohm steps
R_2	Interchangeable resistor -10^6, 10^7, 10^8, 10^9, 10^{10} ohms.
C_g	$1\mu f \pm 1\%$
C_s, C_B	10 to 125 pf variable capacitors

[2] At frequencies above about 5 cps, the objection to the earthing device mentioned above disappears, and some benefit accrues from its use since the bridge equations are then simplified. Accordingly, a brief discussion of the application of this device to the present bridge is given in appendix 7.5 for workers interested principally in the frequency range near and above 5 cps.

[3] One picofarad = one pf = one $\mu\mu$f.

C_3 and C_4, or across the detector terminals. The exception is the capacitance to ground from the junction of R_1, R_2, and R_4. Such capacitance is in parallel with R_1, which has a maximum value of about 100 ohms. It can be shown that a capacitance of 1000 pf across R_1 would not detectably affect the bridge balance even at 1000 cps. The lead capacitance in question is certainly less than 1000 pf and therefore is ignored.

The bridge is balanced when the voltage between the detector terminals is zero. Capacitive balance is essentially achieved when (C_s+C_x) equals C_B. The current in R_x is balanced by inserting an equal and opposite current into the detector terminals. This is accomplished by the network consisting of R_1, R_2, and R_4. The gross magnitude of this current is controlled by the value of R_2 (10^6 to 10^{10} ohms). R_1 is variable in 0.1 ohm steps from 0 to 111 ohms, and serves as a fine adjustment on the current. This arrangement provides a relatively smooth and continuous resistive balance.

The three-terminal generator employed is a Hewlett-Packard model 202A. The output circuit of the generator, as received, is included in figure 1. This circuit, especially J_1, J_2, and C_g, affects the operation of the bridge, and should be regarded electrically as part of the bridge. It will be shown later that it is desirable to operate the bridge with C_g shorted. The resistive components of the generator circuit are denoted by J's rather than R's in order to emphasize the fact that they are physically part of the generator circuit, not part of the external bridge.

Null detection. Between 200 and 5 cps the detector system is a battery powered low noise preamplifier (Tektronix Inc., type 122) followed by a wave analyzer (General Radio Co., type 736–A). An unbalance voltage across the detector terminals of about a microvolt peak-to-peak can be detected. The preamplifier has an input impedance of 20 meg paralleled by 50 pf.

Below 5 cps a d-c voltmeter is employed (Beckman Ultrohmeter). The unbalance signal appears as a periodic deflection on the indicating meter. On the most sensitive range, an unbalance signal of about 2×10^{-5} volts can be detected. An input resistance of 10^{11} ohms is employed.

Below 0.1 cps the output of the d-c voltmeter is monitored by a recording potentiometer. With the recording system employed, an unbalance signal of about 2×10^{-5} volts peak-to-peak can be detected. Since considerable time is spent in balancing, measurements below 0.1 cps are made only when the results are of extreme interest.

2.2. Construction

Care was taken to arrange the components as symmetrically and compactly as possible, and to keep capacitances to ground low. Each component is guarded from others by grounded shields [4] to minimize capacitive coupling.

[4] The internal shields of the bridge are not shown in fig. 1 in order to simplify the drawing.

The rotors of the precision three-terminal variable capacitors C_s and C_B are connected together at the detector terminals. These capacitors are so connected because the capacitance to ground from the stators is more nearly independent of the setting than that from the rotors.[5] Connection in this manner assures that the lead capacitances, C_3 and C_4, are nearly independent of the setting of the capacitors C_s and C_B.

The variable resistor, R_1, is a General Radio Company compensated decade resistor, type 670–F. The "Low" terminal of the resistor is connected to ground.

The interchangeable resistors (R_2) are mounted on a two pole, five position, selector switch and the d-c resistance at each setting is known to better than 0.1 percent. The 10^6 and 10^7 ohm resistors are wire wound; the 10^8, 10^9, and 10^{10} resistors are composition types.

The capacitors, C_s and C_B, are calibrated against NBS reference standards to a precision of ±0.001 pf.

The method employed to switch the unknown "in" and "out" is such that when the unknown is "out" it is in shunt with R_3. (See fig. 1.) This is taken into account in deriving the bridge equations. It would be unwise to place a switch in the lead connecting W with the unknown, for switching at this point would alter the capacitance C_3 by an undetermined amount. The change in C_3 would be equal to the capacitance to ground of the lead and electrode connecting the sample to the switch. It would be ill-advised to change C_3 by an undetermined amount, since by analogy with a Schering bridge, this would affect the measurement of resistance. Similarly, one may discard the possibility of simply disconnecting the lead between the unknown and the detector terminal and allowing it to "float", or disconnecting both leads to the unknown. All of these possibilities lead to undefined changes in C_3 and were therefore not employed.

The resistors J_1 and J_2, which come with the generator, are "one per cent" resistors. Since under some conditions of operation these resistors are essentially the bridge's ratio arms, it is perhaps desirable to remove them from the generator and replace them with externally mounted, matched, precision resistors having magnitudes near 15.8 kohms. In this work they were not replaced since they were found to be adequately matched. Inside the generator, their values change slightly after the generator is turned on; but they remain quite stable once thermal equilibrium is established.

3. Bridge Equations

3.1. Effects of the Generator Output Circuit

The generator circuit has no connection to ground other than through the capacitor C_g, or through the stray impedances Z_1, Z_2, and Z_L, shown in figure 1.

[5] With settings of capacitor C_B between 20 pf and 110 pf the capacitance between the rotor and ground increased from 53.10 to 53.87 pf while the capacitance between the stator and ground increased from 17.63 to 17.75 pf.

The impedances, Z_1 and Z_2, shunt the ratio arms and may alter the impedance of the arms. The bridge equations will be worked out without taking formal cognizance of Z_1 and Z_2, but in such a way that their possible effects may be determined.

The impedance Z_L is believed to be primarily capacitive in nature since B^- is connected to the shield of the generator's power transformer. If Z_L be regarded as a capacitor, then we see that the network J_3, Z_L, J_4 is similar to the network J_1, C_g, J_2. Thus, if one establishes the effects of the network J_1, C_g, J_2 upon the bridge the effect of J_3, Z_L, J_4 will have been at least qualitatively predicted.

Since there is no direct connection to ground in the generator, one may ground any point of the output circuit. It is obvious from figure 1 that the network J_1, C_g, J_2 will give rise to frequency-dependent parallel capacitive and resistive shunts across R_3 and (R_4+R_1). (This is easily demonstrated by a Y→Δ transformation.) This will clearly complicate the bridge equation and as is demonstrated later gives rise to undesirable frequency dependent "correction terms". If C_g is removed ($C_g=0$) the output of the "floating" generator is noisy and somewhat unstable, which is undesirable. These difficulties are avoided if one grounds point A of figure 1. This shorts out C_g ($C_g=\infty$) so that J_1 and J_2 are placed across R_3 and (R_4+R_1). Since J_1 and J_2 are 15.8 kohm and R_3 and R_4 are 100 kohm, J_1 and J_2 essentially become ratio arms while R_3, R_1, and R_4 serve as part of the conductance balancing network. This is advantageous since variations in R_1 will now cause less change in the equivalent resistance of the arm. In view of these facts, in practice the bridge is operated with C_g shorted.

Nevertheless, the bridge equations will first be worked out for the case when C_g is in the circuit. This procedure yields general equations which (a) clearly show the effects of C_g, (b) are useful in checking out the bridge, (c) qualitatively predict the possible effects of the network J_3, Z_L, J_4, and (d) can readily be simplified for the case $C_g=\infty$, the mode of operation to be adopted in making routine measurements.

3.2. Derivation of Balance Equations with $C_g=1$ μf

The bridge is balanced by varying C_s, C_B, R_1, and R_2. The value of C_B and R_2 used depends upon the magnitude of C_x and R_x. The values of R_2 and C_B are not changed when switching the unknown in and out.

It is convenient to first transform the Y network formed by R_1, R_2, and R_4 into a Δ network as shown in figure 2(a). The equivalent resistance R_A is in parallel with C_4, R_B in parallel with C_B, and R_E across the detector terminals. These resistances have values given by

$$R_A=R_1+R_4+\frac{R_1R_4}{R_2}$$

$$R_B=R_4+R_2+\frac{R_4R_2}{R_1} \qquad (1)$$

$$R_E=R_2+R_1+\frac{R_2R_1}{R_4}$$

Lumping the impedances in each of the arms, the bridge is now equivalent to the circuit shown in figure 2(b). Here Z_P represents the lumped impedance of the standard capacitor and the unknown when it is in parallel with C_s. The balance condition, derived in appendix 7.1, is

$$\frac{1}{Z_P}\left(r+\frac{Z_g}{Z_A}(1+r)+\frac{J_1}{Z_A}\right)=\frac{1}{Z_B}\left(1+\frac{Z_g}{Z_3}(1+r)+\frac{J_1}{Z_3}\right), \qquad (2)$$

where

$$r=J_1/J_2. \qquad (3)$$

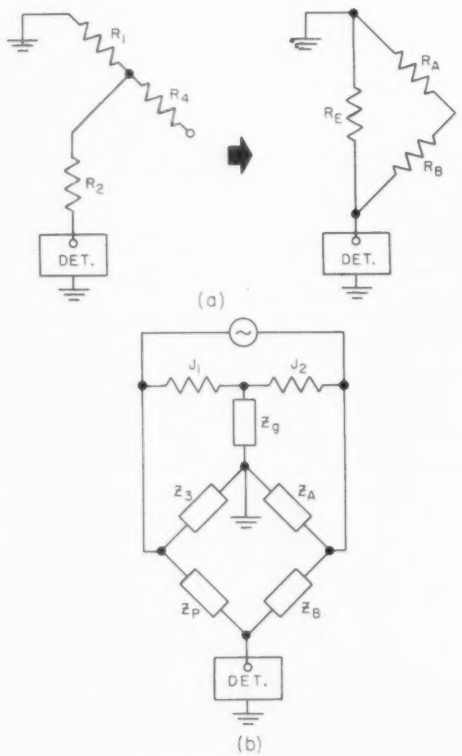

FIGURE 2. *Network transformations.*

a) Transformation of resistive Y network into a Δ network.
b) Equivalent bridge circuit after transformation. The Z's represent lumped impedances.

The impedances [6] in terms of parallel components, are given by

$$\frac{1}{Z_i}=\frac{1}{R_i}+j\omega C_i \tag{4}$$

where index i has values P, B, and 3, and

$$\frac{1}{Z_A}=\frac{1}{R_A}+j\omega C_4,$$

$$Z_g=-\frac{j}{\omega C_g}. \tag{5}$$

Substituting these values into eq (2) one obtains the following, upon separation of real and imaginary parts

$$C_P\left(r+\frac{J_1}{R_A}+(1+r)\frac{C_4}{C_g}\right)+\frac{1}{R_P}\left(J_1C_4-\frac{(1+r)}{\omega^2R_AC_g}\right)$$
$$=C_B\left(1+\frac{J_1}{R_3}+(1+r)\frac{C_3}{C_g}\right)+\frac{1}{R_B}\left(J_1C_3-\frac{(1+r)}{\omega^2R_3C_g}\right), \tag{6}$$

and

$$\frac{1}{R_P}\left(r+\frac{J_1}{R_A}+(1+r)\frac{C_4}{C_g}\right)+C_P\left(\frac{(1+r)}{R_AC_g}-\omega^2J_1C_4\right)$$
$$=\frac{1}{R_B}\left(1+\frac{J_1}{R_3}+(1+r)\frac{C_3}{C_g}\right)+C_B\left(\frac{(1+r)}{R_3C_g}-\omega^2J_1C_3\right). \tag{7}$$

Since the substitution method is employed, equations (6) and (7) apply with the unknown across C_s' and with it disconnected from across C_s.

With the unknown across C_s let the values of R_1 and C_s at balance be denoted as R_1'' and C_s'' respectively. The variable factors of eqs (6) and (7) become

$$\frac{1}{R_P}=\frac{1}{R_x}+\frac{1}{R_s}$$
$$R_A=R_A''$$
$$R_B=R_B'' \tag{8}$$
$$C_P=C_s''+C_x$$

where R_A'' and R_B'' may be computed simply from equations (1) substituting R_1'' for R_1. The parallel resistance, R_s, of the capacitor C_s is included in the equation for R_P^{-1}. Subsequently, it is assumed that R_s is independent of the setting of C_s.

With the unknown "out" we denote the value of R_1 and C_s at balance as R_1' and C_s' respectively. The variable factors in equations (6) and (7) become

$$R_P=R_s$$
$$R_A=R_A'$$
$$R_B=R_B' \tag{9}$$
$$C_P=C_s' .$$

Since the unknown now shunts R_3, $(R_3^{-1}+R_x^{-1})$ replaces R_3^{-1}. Furthermore, C_x now shunts R_3. The magnitude of C_3 is held constant, however, by decreasing the setting of the variable capacitor across R_3 by C_x. By obtaining a capacitive balance, C_s', before C_3 is adjusted, C_x may be determined to a sufficient accuracy as $(C_s'-C_s'')$. C_3 is then adjusted by this amount. (This procedure is possible since the capacitance balance C_s is practically independent of these changes in C_3.)

Substituting eqs (8) and (9) into (6) and (7) results in four equations from which exact solutions for R_x and C_x may be obtained. The exact solutions are given in appendix 7.2, where it is shown that certain terms are small and may be omitted. The parallel capacitance, C_x, and conductance, G_x, of the unknown are given by

$$C_x=\Delta C_s+C_s'\frac{\Delta R_1}{R_4}K+(C_3-C_4)\frac{\Delta R_1}{R_2}K$$
$$+\frac{\Delta R_1}{R_2}(R_3-rR_4-R_1'')L \tag{10}$$

and

$$G_x=\frac{1}{R_x}=\frac{\Delta R_1}{R_2R_4}\left[1+C_s'R_2F\left(1+\frac{\omega^2C_4C_gJ_1^2}{2}\right)\right] \tag{11}$$

where

$$\Delta C_s=C_s'-C_s''$$
$$\Delta R_1=R_1''-R_1' \tag{12}$$
$$\omega=2\pi f,$$

$$K=\frac{1+\omega^2\tau_0^2+R_4/J_2}{(1+\omega^2\tau_0^2)(1+R_4/J_2)} \tag{13}$$

$$L=\frac{C_g}{2R_4}/(1+\omega^2\tau_0^2), \tag{14}$$

$$F=\frac{\omega^2\tau_0^2}{1+\omega^2\tau_0^2}\left[\frac{2}{C_gR_4(1+J_1/R_4)^2}\right], \tag{15}$$

and

$$\omega\tau_0=\frac{\omega R_4C_g}{2}[1+J_1/R_4]. \tag{16}$$

In eq (10) terms which contribute no more than 0.001 pf have been omitted. In eq (11) terms contributing 0.2 percent or less have been dropped.

[6] The notation $j=\sqrt{-1}$ is employed. Unless otherwise stated the units of resistance (R) is ohms; capacitance (C) farads; and frequency (f), cps.

3.3. Evaluation of Terms in the Balance Equations with $C_g=1$ μf

Equations (10) and (11) can be placed in better perspective by numerical evaluation of the quantities F, K, and L.

Using the values of the bridge components given in table 1, eq (16) gives

$$\omega^2\tau_0^2=0.132f^2. \tag{17}$$

Similarly, F, K, and L become

$$F=15.0\,\frac{\omega^2\tau_0^2}{1+\omega^2\tau_0^2}\ \text{(radians/sec)}, \tag{18}$$

$$K=\frac{\omega^2\tau_0^2+7.33}{(1+\omega^2\tau_0^2)7.33}, \tag{19}$$

$$L=\frac{5}{(1+\omega^2\tau_0^2)}\ \text{(pf/ohm)}. \tag{20}$$

The function F has a high frequency maximum value of about 15 rad/sec and drops sigmoidally toward zero at low frequencies. L is also a sigmoidal function which is zero at low frequencies and 5 pf/ohm at low frequencies. Both F and L are half their maximum values when $f=2.8$ cps. The quantity K is plotted against frequency in figure 3. It has a value of 0.136 at high frequencies and rises sigmoidally toward unity at low frequencies. Also shown in figure 3 is the value of K calculated for other values of C_g, along with experimental points. The significance of these points is discussed in section 4.2a.

a. Capacitance Equation

In the equation for capacitance, eq (10),

$$C_x=\Delta C_s+C_s'\Delta R_1K/R_4+(C_3-C_4)\Delta R_1K/R_2 \\ +(R_3-R_1''-rR_4)\Delta R_1L/R_2,$$

it is apparent that ΔC_s is ordinarily the predominant term and the other three are "correction" terms. Let us maximize these correction terms in order to evaluate their importance.

The term $C_s'\Delta R_1K/R_4$ has a *maximum* value of only 0.138 pf. This value is achieved when ΔR_1 is 110 ohms, K is unity, and C_s' is 125 pf. This is usually the most important of the correction terms.

The magnitude of the correction term, $(C_3-C_4)\Delta R_1K/R_2$, depends upon the unbalance (C_3-C_4), which can be experimentally determined or eliminated. The procedure is to short out C_g, and switch the unknown out; i.e., across R_3. At high frequencies (200 cps), with $C_g=\infty$, eq (7) to a close approximation becomes

$$\frac{R_1}{R_2R_4}\left[\frac{1}{J_1}+\frac{1}{R_3}\right]=C_s\omega^2[C_3-C_4]. \tag{21}$$

If one sets R_1 to zero and balances the bridge at 200 cps by adjusting C_3 (this is the method employed in balancing a Schering bridge), then (C_3-C_4) becomes zero. Consequently, the correction term is zero. This desirable condition may become disturbed at lower frequencies however, since C_x, which adds to C_3, may have significant frequency dependence. Under this condition the magnitude of (C_3-C_4) becomes $(C_3-C_4)=[C_x(f)-C_x(200\ \text{cps})]$, where $C_x(f)$ is the value of C_x at the frequency f. Even if (C_3-C_4) were 100 pf, then, with $C_g=1$ μf, the maximum value of the correction term $(C_3-C_4)K\Delta R_1/R_2$ is only 0.011 pf.[7]

The correction term, $(R_3-rR_4-R_1'')\Delta R_1L/R_2$, depends critically upon the unbalance in the resistors J_1 and J_2, and in R_3 and R_4. The ratio r is $0.99859\pm.00004$ (See section 4.2a). Using the values of R_3 and R_4 given in table 1, $(R_3-rR_4-R_1'')$ becomes $(211\ \text{ohms}-R_1'')\pm10$ ohms. The maximum possible value of this correction term is therefore 0.055 pf.

Summarizing the above calculations, it is apparent that in most practical cases the correction terms of eq (10) are small. The largest of these terms, $C_s'\Delta R_1K/R_4$, has a maximum value of only 0.138 pf.

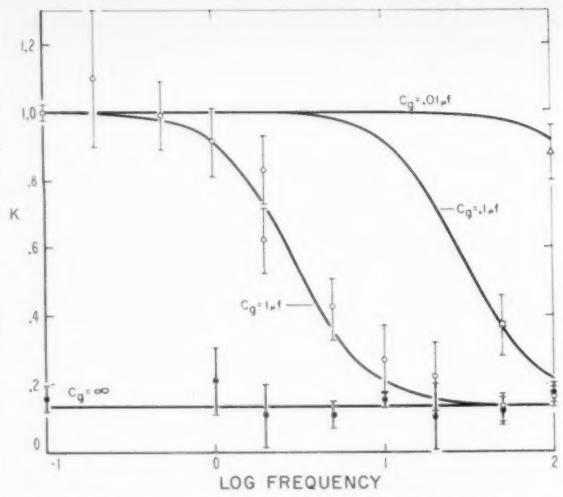

FIGURE 3. *Frequency dependence of the largest correction term in the expression for* C_x.

K determines the frequency dependence of the main correction term of eq (10). The solid lines are calculated using the indicated values of C_g. The experimental points, along with an indication of the experimental error, are shown.

With $C_g=1$μf, the correction term $C_s'K\Delta R_1/R_4$ is strongly frequency dependent, and can attain a maximum value at low frequencies of 0.138 pf ($K=1$). In practice, the bridge is operated with $C_g=\infty$ so that $C_s'K\Delta R_1/R_4$ is independent of frequency, has a maximum value of only 0.019 pf, and can be determined to better than 0.001 pf.

b. Conductance equation

In the expression for the conductance, eq (11),

$$G_x=\frac{\Delta R_1}{R_2R_4}\left[1+C_s'R_2F\left(1+\frac{\omega^2C_4C_gJ_1^2}{2}\right)\right],$$

[7] Further consideration of the possible frequency dependence of (C_3-C_4) due to other factors is given in section 4.2 b.

the product $C''_s R_2 F(1+\omega^2 C_4 C_g J_1^2/2)$ may be regarded as a correction term. Because of sensitivity considerations, discussed in section 3.5, the 10^9 and 10^{10} ohm values of R_2 are never used above 5 cps. (Their use is also confined to low frequencies because of possible frequency dependence in their resistance above 5 cps (see table 2).) At high frequencies the largest value of R_2 employed is 10^8 ohms. Therefore, the largest value of $C''_s R_2 F$ ever encountered is 0.15.

The correction term contains the multiplying factor $(1+\omega^2 C_4 C_g J_1^2/2)$. Setting C_4 equal to 1450 pf$\pm$ 10 percent (this value is determined in appendix 7.4), then $\omega^2 C_4 C_g J_1^2/2$ becomes (0.286 ± 0.029) at 200 cps. Therefore, the total correction becomes $(0.15+0.043\pm 0.004)$.

3.4. Bridge Equations with C_g Shorted

Let us now consider the case in which C_g is shorted ($C_g=\infty$), the mode of operation to be used in practice. With C_g shorted, J_1 and J_2 are in parallel with R_3 and R_4 respectively. This lowers the equivalent resistance of each arm, and furthermore makes the equivalent resistance independent of frequency.

The exact bridge equations for the case $C_g=\infty$ are given in appendix 7.3. Simplified equations which give C_x and G_x to a sufficient accuracy are

$$C_x=\Delta C_s+C''_s\frac{\Delta R_1}{R_4}K+(C_3-C_4)\frac{\Delta R_1}{R_2}K, \qquad (22)$$

$$G_x=\frac{\Delta R_1}{R_2 R_4}[1+C''_s R_2\omega^2 C_4 R_4 K^2], \qquad (23)$$

where

$$K=J_2/(J_2+R_4)=0.136.$$

Notice that one of the correction terms extant in eq (10) is absent in eq (22). Both of the correction terms of eq (22) contain the factor K, which now has the constant value 0.136, whereas in eq (10), K varied with frequency having a maximum value of unity. In eq (22) the correction term involving (C_3-C_4) may be made negligibly small by balancing C_3 and C_4 at 200 cps (see eq (21)). *The term $C''_s K\Delta R_1/R_4$ now has a maximum value of only* 0.019 pf.

The expression for the conductance, eq (23), contains a small frequency-dependent correction term. This term is largest when $C''_s=100$ pf; $R_2=10^8$ ohms, and $f=200$ cps. Using $C_4=1450$ pf$\pm$10 percent, the term becomes 0.05 ± 0.005. This value is much less than its counterpart in eq (11), which is 0.19. It should be noted that the 10 percent uncertainty in C_4 may cause an error of 1 percent or more at frequencies above 200 cps.

Below 9 cps, even if R_2 were 10^{10} ohms, the correction term of eq (23) contributes less than one percent to the total conductance and, therefore, may be ignored.

Since the correction terms in eqs (22) and (23) are smaller and far less dependent upon frequency than those in eqs (10) and (11), *in practice the bridge is operated with $C_g=\infty$ where eqs* (22) *and* (23) *apply.*

The reader is reminded that eqs (22) and (23) apply to substitution measurements only if C_3 is decreased by C_x when the unknown is switched "out." The procedure is outlined in section 3.2.

Inspection of eqs (22) and (23) shows that capacitances between zero and 100 pf are measurable, while conductances between 10^{-9} and 10^{-16} mhos may possibly be measured. The sensitivity of the apparatus, however, places closer limits on these extremes, particularly upon the lower limit of conductance.

3.5. Sensitivity

It is informative to calculate the magnitude of the voltage appearing across the detector terminals due to a small departure from perfect capacitive or resistive balance. The expression for this voltage shows how to improve the sensitivity and predicts the smallest observable impedance unbalance.

The simplified circuit diagram in figure 4 is used in calculating the sensitivity. With C_g shorted, the equivalent resistances of the ratio arms are denoted as R_K and R_L. The impedance, Z_D, which shunts the detector terminals, consists of the input impedance of the detector employed (R_I), paralleled by R_E, as given in eq (1), and by the total capacitance to ground across the detector terminals, C_D. The expression for $1/Z_D$ is

$$\frac{1}{Z_D}=\frac{1}{R_D}+j\omega C_D, \qquad (24)$$

where R_D is the resultant parallel resistance of R_E and R_I.

The voltage developed across the detector terminals, V_D, is given by

$$V_D=\frac{V[R_L/Z_P-R_K/Z_B]}{(R_L+R_K)\left(\frac{1}{Z_D}+\frac{1}{Z_P}+\frac{1}{Z_B}\right)+\frac{R_L R_K}{Z_P}\left(\frac{1}{Z_P}+\frac{1}{Z_B}\right)}, \qquad (25)$$

where V is the applied voltage.

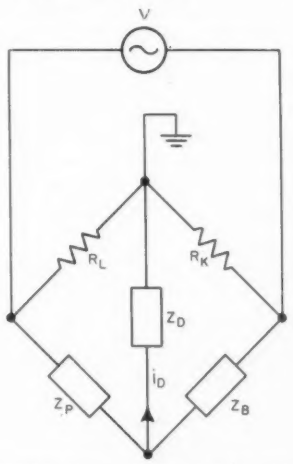

FIGURE 4. *Simplified circuit diagram from which the sensitivity is calculated.*

We now make the approximations that $R_L=R_K$, and that the bridge is sufficiently balanced so that we may set Z_P equal to Z_B in the denominator of eq (25). Equation (25) becomes

$$V_D=\frac{\frac{V}{2}\left(\frac{1}{Z_P}-\frac{1}{Z_B}\right)}{\frac{1}{Z_D}+\frac{2}{Z_B}+\frac{R_L}{Z_DZ_B}}. \tag{26}$$

The term R_L/Z_BZ_D may be dropped from the denominator leaving

$$V_D=\frac{\frac{V}{2}\left[\frac{1}{Z_P}-\frac{1}{Z_B}\right]}{\frac{1}{Z_D}+\frac{2}{Z_B}}. \tag{27}$$

Substituting for the Z's and using the approximation that $2/R_B \ll 1/R_D$ we obtain

$$V_D=\frac{(V/2)R_D[1/R_P-1/R_B+j\omega(C_P-C_B)][1-j\omega R_D(2C_B+C_D)]}{1+\omega^2R_D{}^2(2C_B+C_D)^2} \tag{28}$$

This approximate equation predicts that the bridge is balanced (V_D=zero) when $R_P=R_B$ and $C_P=C_B$.

Let a small departure from capacitive balance be represented by $\pm\,\delta C_P$ such that

$$C_P-C_B=\pm\delta C_P \tag{29}$$

A small conductance unbalance, δG_P, is defined as

$$1/R_P-1/R_B=\pm\delta G_P \tag{30}$$

Equation (28) may be used to calculate V_D when a slight conductance unbalance exists in the presence of perfect capacitive balance. Setting $\delta C_P=0$, and using eq (30) one obtains for the amplitude of V_D.

$$|V_D|=\frac{\left|\frac{V}{2}\right|R_D|\delta G_P|}{\sqrt{1+\omega^2R_D{}^2(2C_B+C_D)^2}}. \tag{31}$$

Therefore,

$$\left|\frac{V_D}{\delta G_P}\right|=\frac{\left|\frac{V}{2}\right|R_D}{\sqrt{1+\omega^2R_D^2(2C_B+C_D)^2}}. \tag{32}$$

The expression for V_D per unit capacitance unbalance in the presence of perfect resistive balance may similarly be derived and is

$$\left|\frac{V_D}{\delta C_P}\right|=\frac{\left|\frac{V}{2}\right|\omega R_D}{\sqrt{1+\omega^2R_D^2(2C_B+C_D)^2}}. \tag{33}$$

Equations (32) and (33) both show that the sensitivity may be increased by lowering C_D. This may be accomplished by minimizing the appropriate lead capacitances and the input capacitance of the detecting device.[8]

In figure 5 is plotted $V_D/\delta C_P$[9] versus (fR_D). Here we have estimated C_D=200 pf, and assumed C_B=60 pf. The peak-to-peak voltage of the generator, V, is 30 volts. Note that in those cases in which $\omega R_D(2C_B+C_D)<1$, $V_D/\delta C_P$ varies linearly with the product (ωR_D). Under these conditions, the sensitivity may be held roughly constant as ω decreases by increasing R_D by a multiple of ten for each decade decreased in ω. Since $1/R_D\simeq 1/R_2+1/R_I$, R_D can be increased by increasing R_2, but can never become greater than R_I. Therefore, *the value of the input resistor of the detector will ultimately limit the sensitivity at low frequencies.* Also, since the conductance must be balanced, one is not entirely free in choice of R_2. Optimum conditions exist when R_2 is made as large as possible while still permitting conductance balance of the bridge. In general the smaller R_x, the poorer the sensitivity to capacitive unbalance.

When $\omega R_D(2C_B+C_D)>1$, $V_D/\delta C_P$ approaches a maximum of

$$\frac{V_D}{0.001\text{ pf}}=\frac{\frac{V}{2}\times 10^{-15}}{2C_B+C_D}=4.7\times 10^{-5}\,\frac{\text{peak-to-peak volts}}{0.001\text{ pf}}.$$

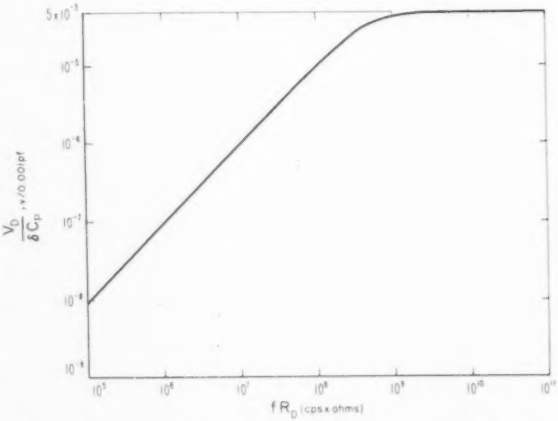

FIGURE 5. *Log-log plot of the voltage appearing across the detector terminals* (V_D) *per increment capacitance unbalance* (δC_P) *versus the product* fR_D.

In figure 6 is plotted $V_D/\delta G_P$ vs. frequency for various values of R_D. The smallest increment in G_P possible with this apparatus (10^{-16} mhos) is chosen for δG_P. Note that when $\omega R_D(2C_B+C_D)>1$, $V_D/\delta G_P$

[8] In order to lower C_D the 250 pf capacitor shunting the input resistor of the Ultrohmeter has been disconnected.

[9] The amplitude symbol, | |, is dropped at this point.

increases as the frequency decreases and is independent of R_D. When $\omega R_D(2C_B+C_D)<1$, $V_D/\delta G_P$ is independent of frequency but increases linearly with R_D. In general, best sensitivity to conductance unbalance is attained at low frequency using high values of R_D.

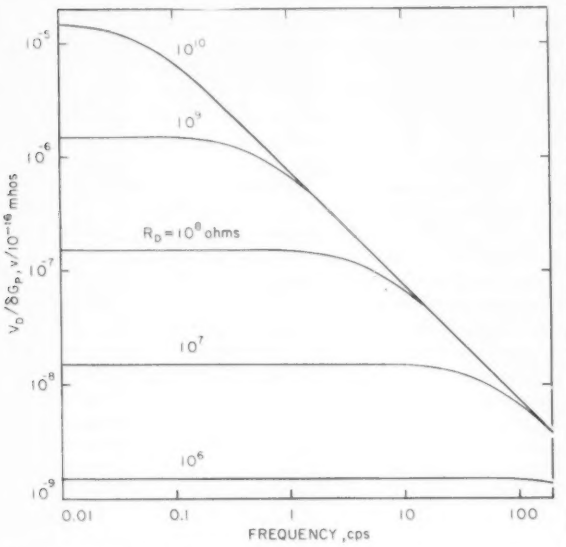

FIGURE 6. *The unbalance voltage per increment conductance unbalance versus frequency.*

Once the sensitivity of the detector employed is ascertained, this graph may be used to determine the minimum detectable conductance unbalance under various operating conditions.

In practice the bridge is operated using the highest value of R_2[10] that will permit resistive balance. This condition also enhances $V_D/\delta C_P$, as was previously discussed.

Equations (32) and (33) give the voltage at the output terminals for a given bridge unbalance. Whether or not this voltage is observable depends upon the sensitivity of the detector. If we denote minimum voltage detectable as v_m, then the smallest capacitive unbalance detectable becomes

$$dC=\frac{v_m}{V_D/\delta C_P}. \tag{34}$$

The smallest detectable conductance unbalance is

$$dG=\frac{v_m}{V_D/\delta G_P}. \tag{35}$$

The accuracy with which dC and dG may be computed depends upon the accuracy with which v_m and C_D are known. It is impossible to determine v_m with great precision. Also the value of C_D employed (200 pf), is merely an estimate. Therefore, values of dC and dG computed from eqs (34) and (35) may be in error by as much as 100 percent.

Calculated values of dC and dG, for various possible conditions of operation, are shown in table 2. These calculated values have proven to be essentially correct experimentally. Since the sensitivity, v_m, of the detector employed,[11] as well as its input resistance, R_I, effect the results, the values of dC and dG will be different if other detection systems are employed.

TABLE 2. *The minimum detectable capacitance unbalance, dC, and minimum detectable conductance unbalance, dG, for various operating conditions.*

Frequency	Detector [a]	R_2	dC	dG	G_m [b]
cps		*ohms*	*pf*	*mhos*	*mhos*
100	I	10^6	<0.001	1.3×10^{-13}	10^{-12}
		10^8	$\lesssim.001$	2.6×10^{-14}	10^{-14}
10	I	10^6	.002	1.3×10^{-13}	10^{-12}
		10^8	$<.001$	1.3×10^{-14}	10^{-14}
1	II	10^6	.2	1.3×10^{-12}	10^{-12}
		10^{10}	$<.001$	2.6×10^{-15}	10^{-16}
0.1	II	10^6	2.0	1.3×10^{-12}	10^{-12}
		10^{10}	<0.001	3.0×10^{-16}	10^{-16}
0.01	III	10^6	20.0	1.3×10^{-12}	10^{-12}
		10^{10}	0.002	1.3×10^{-16}	10^{-16}

[a] Detector I—preamplifier-waveanalyzer, II—Ultrohmeter, III—Ultrohmeter-d-c recorder.
[b] G_m is the conductance change due to a 0.1 ohm change in R_1.

Between 200 and 5 cps capacitance unbalances of 0.001 pf may almost always be detected.

With the Ultrohmeter as detector between 2 and 0.1 cps, dC is less than 0.001 pf unless $fR_D<2\times10^8$ cps-ohm. Then dC is given approximately by

$$dC=\frac{2\times10^5}{fR_D}\ (\text{pf}). \tag{36}$$

At 1 cps with $R_2=10^6$ ohms, dC is 0.2 pf. At 0.1 cps with $R_2=10^6$ ohms, dC is 2 pf, which is a large uncertainty. Fortunately, the situation rarely arises which requires $R_2=10^6$ ohms at 0.1 cps. Most dielectrics have a loss index, ϵ'' less than unity. Since

$$\epsilon''=\frac{1}{\omega R_x C_x}, \tag{37}$$

[10] Maximizing R_1 or equivalently ΔR_1, will also increase the magnitude of the correction term, $C_1'K\Delta R_1/R_4$ which appears in eq (22).

[11] The effective sensitivities of the detectors employed are somewhat frequency dependent, as well as functions of the noise level. At 100 through 5 cps an error voltage of about 2×10^{-6} volts can be detected. A signal of about 2×10^{-5} volts can be detected on the Ultrohmeter at 2 cps and at 0.1 cps. At intermediate frequencies, signals as low as 3×10^{-6} volts are observable. A d-c voltage of 4×10^{-5} volts, however, just gives a detectable indication (about one tenth division deflection). The increased sensitivity of the Ultrohmeter to a low frequency a-c signal is possibly due to the feedback utilized, or to a mechanical "resonance" of the meter's pointer. Using the Ultrohmeter-recorder system below 0.1 cps, a signal of 2×10^{-5} volts is detectable.

if the specimen's equivalent vacuum capacitance, C_v, were about 10 pf, its loss index would have to be near 100 to require use of the 10^6 ohm value of R_2 at 0.1 cps. Similarly, at 0.01 cps, the 10^6 or even the 10^7 ohm range would practically never be required.

The minimum conductance detectable throughout the frequency range is given roughly by the approximate expression

$$G_{xm}=3f\times10^{-15} \text{ mhos when } f\geq 0.1 \text{ cps}$$
$$\text{or} \qquad (38)$$
$$G_{xm}=2\times10^{-16} \text{ mhos when } f<0.1 \text{ cps}$$

(This expression underrates the capabilities of the bridge above 5 cps.)

The minimum detectable loss index is approximately,

$$\epsilon''_m=5\times10^{-4}/C_v(\text{pf}) \text{ when } f\geq 0.1 \text{ cps}$$
$$\text{or} \qquad (39)$$
$$\epsilon''_m=3\times10^{-5}/fC_v(\text{pf}) \text{ when } f<0.1 \text{ cps}.$$

4. Experimental Check of the Bridge

In order to check the bridge experimentally, measurements were made upon resistors and capacitors of known values. Most of these measurements were performed both with $C_g=1$ μf and with $C_g=\infty$. Comparison of the results obtained using the two methods in no case revealed any significant discrepancies.

4.1. Measurements upon Capacitors and Resistors of Known Values

Preliminary measurements were made upon a 5.004 pf fixed reference standard capacitor in parallel with resistors ranging in value from 10^{10} to 10^{14} ohms. The measured value of the parallel capacitance of the resistor itself was subtracted from the measured capacitance of the RC combination to obtain values associated with the standard capacitor. The results of some thirty measurements made at various frequencies within the range of 0.1 cps to 200 cps, averaged to 5.0055 pf with a standard deviation of 0.0013 pf. This agreement is satisfactory, the error being only 0.03 percent.

The results of measurements on resistors are shown in table 3.[12] The d-c values given in the last row were determined to an accuracy of better than 0.5 percent by an independent technique due to Scott [8] in which a variable air capacitor is discharged through the unknown resistor while holding the voltage constant by smoothly decreasing the capacitance. The values obtained at low frequencies agree with the d-c values to well within 1 percent for the 10^9, 10^{10}, 10^{11}, 10^{12}, and 10^{13} ohm resistors. This clearly shows the bridge's ability to accurately measure resistances in this range at low frequencies. At high frequencies however, there is extreme departure from the d-c values for nearly all the resistors. Rough measurements made with a two-terminal Schering bridge near 100 cps essentially corroborate the findings of the low frequency bridge in this region. These results lead to the conclusion that the particular composition resistors measured exhibited a strong frequency dependence.

[12] These resistors were measured in a shielded chamber through which a flow of dried nitrogen gas was maintained. Measurements on the 10^{13} ohm resistor at 100 cps in 50 percent relative humidity showed the conductance to be a decade higher than it was with dry nitrogen flowing. Results below 1 cps were unaffected by this humidity change. Since we have no assurance that the flow of nitrogen removed all surface moisture, it is possible that the increased conductance at high frequencies may be partially due to moisture.

TABLE 3. *Results of measurements on resistors*

Frequency	Measured value in ohms					
	Resistor 1	Resistor 2	Resistor 3	Resistor 4	Resistor 5	Resistor 6
cps						
100	1.125×10^9	0.868×10^{10}	0.563×10^{11}	0.097×10^{12}	0.087×10^{13}	0.013×10^{14}
50	1.160	.895	.678	.214	.104	.021
20	1.167	.949	.803	.427		.037
10	1.169	.960	.874	.59	.258	.062
5			.942	.75	.321	
2	1.173	.980	.980	.87	.420	.120
1	1.173	.983	.990	.95	.54	.160
0.5	1.174	.983	.994	.98	.64	.211
.2	1.174	.983	.999	1.002	.78	
.1	1.173	.983	1.000	1.004	.88	.35
.05	[b]			1.004	.92	.46
.01	[b]			1.006	1.00	.84
d-c[a]	1.173×10^9	$.9835\times10^{10}$	$.995\times10^{11}$	1.002×10^{12}	1.01×10^{13}	1.11×10^{14}

[a] These d-c values are essentially independent of voltage up to 15 volts.
[b] Measurements on resistor 1 at 0.05 and 0.01 cps, were made 1 year after the previous measurements and both gave 1.184×10^9 ohms. The d-c value was redetermined and found to be 1.178×10^9 ohms.

This frequency dependence is understandable in light of the theoretical work of Howe [9]. He considered a cylindrically shaped composition resistor and associated with it a constant capacitance per unit length. He showed that the equivalent parallel resistance and capacitance drop off sharply from their d-c values as the frequency is increased above a certain value. From his work, it can be inferred that the equivalent resistance has decreased about one percent from its d-c value (R) when the product (Rf) is near 10^{12} cps-ohms, and decreases sharply at higher frequencies. Using this rule, a 10^{12} ohm resistor should begin to exhibit a frequency dependence near 1 cps, a 10^{13} ohm resistor near 0.1 cps, etc. Referring to table 3, we see that these predictions are roughly verified.

The frequency dependence of the nominal 10^{14} ohm resistor was further investigated using d-c techniques. The current in the resistor was measured as a function of time, t, after application of 20 volts d-c. The resistance at time t was then calculated using Ohm's law. A frequency, f, was associated with the time interval, t, according to the equation:

$$f=0.1/t. \tag{40}$$

Equation (40) has been proposed and used by Hamon [10]. He has shown that under certain conditions eq (40) may be used to convert from decay current studies of dielectrics to their a-c dielectric properties. Although there is no assurance that the conditions which justify the use of eq (40) are rigorously fulfilled in the present experiment, it is the only such equation which has been justified and it is employed here with reasonable success.

The results of these d-c measurements on resistor 6 are shown in figure 7 along with the results obtained on the low frequency bridge. The two sets of data form a reasonably smooth curve, which gives additional confidence in the accuracy of the low frequency bridge in measurements of high values of resistance. The d-c measurements also provide an independent demonstration of the frequency dependence of these resistors.

The frequency dependence of these resistors makes it impossible to present a clear cut demonstration of the accuracy of the bridge through measurements of fixed, known, conductances across its entire frequency range. Estimates of the accuracy of conductance measurements is based therefore upon (a) sensitivity considerations (eq (38)), (b) the fact that measurements at low frequencies on lower values of resistance are within one percent of the d-c value, and (c) the agreement, at higher frequencies, with Schering bridge measurements (see section 5). The overall accuracy in conductance is therefore about $\pm$ (1 percent + $3f \times 10^{-15}$ mhos) when $f \geq 0.1$ cps, and about $\pm$ (1 percent + 2×10^{-16} mhos) when $f < 0.1$ cps.

From similar evidence the accuracy of capacitance measurements may be estimated. While using the preamplifier-wave analyzer as detector, capacitances can be measured to an accuracy of about $\pm$ (0.05 percent + 0.002 pf). Using the Ultrohmeter below 5 cps the accuracy is about $\pm$ [0.05 percent + (0.002 + $2 \times 10^5/f\ R_D$) pf].

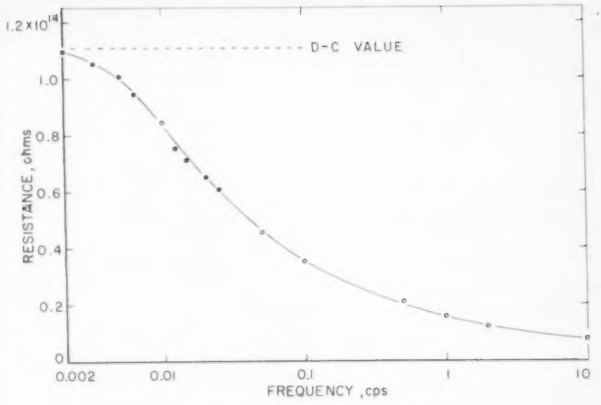

FIGURE 7. *Frequency dependence of a nominal 10^{14} ohm resistor (resistor 6).*

○—low frequency apparatus

●—d-c decay measurement using $f=0.1/t$, where t is the time in seconds after application of the d-c voltage.

4.2. The Effects of Z_1, Z_2, and Z_L

Let us now investigate the effects of the stray impedances to ground within the generator Z_1, Z_2, and Z_L. Referring to figures 1 and 2 it is apparent that any of these impedances may give rise to resistive and (or) capacitive shunts across R_3 and R_A. The possibility exists that these shunts may be frequency dependent. The bridge equations, (10) and (11), show that impedances shunting R_3 or R_A affect the results of substitution measurements only in the *"correction terms"*. Therefore, it is possible to learn something of the magnitude of these stray impedances through an experimental study of these terms.

a. Stray Resistive Shunting of the Ratio Arms

The largest of the correction terms in eq (10) is the quantity, $C_s'K\Delta R_1/R_4$, which has a maximum value of 0.138 pf. Through an experimental study of this term it is demonstrated that no appreciable stray *resistive* shunting of the ratio arms occurs. An understanding of the origin of this term will be helpful in the discussion to follow.

The correction term, $(C_s'\Delta R_1 K/R_4)$, arises from the fact that the equivalent value of one of the ratio arms is dependent upon the setting of R_1. Since R_1 is varied to balance the conductance, R_A will be different for the two bridge balances necessary in the substitution method. If the ratio arms are not the same at the two balances, the capacitance measurement requires a correction.

573960—61——3

It can be shown that if any resistor, which we shall call J_K shunts R_A (such as J_2 shunts R_A when C_g is shorted)[13] then K is given by

$$K=\frac{J_K}{J_K+R_4}. \tag{41}$$

Therefore, through measurements of K it is possible not only to ascertain that a resistor is shunting R_A, but also to determine its magnitude.

The magnitude of K can be determined by performing two substitution measurements of the parallel capacitance and resistance of a resistor. These measurements are made using two consecutive values of R_2. Using values of R_2 having a ratio of ten to one necessitates that the ratio of the ΔR_1's between the two measurements be one to ten. Therefore, the magnitudes of $C_s'\Delta R_1 K/R_4$, will differ by nearly a multiple of ten. The difference in ΔC_s and in ΔR_1 between the two measurements (labeled 1 and 2) are $[(\Delta C_s)_1-(\Delta C_s)_2]$ and $[(\Delta R_1)_1-(\Delta R_1)_2]$ respectively. K is then

$$K=\frac{R_4[(\Delta C_s)_1-(\Delta C_s)_2]}{C_s'[(\Delta R_1)_2-(\Delta R_1)_1]}. \tag{42}$$

The preceding outlines the method used to detect a resistive shunt on R_A. Due to the symmetry of the generator circuit one would expect that if a resistance shunts R_A, one nearly equal in magnitude would shunt R_3. One cannot be certain of this, however, and a method through which a resistive shunt on R_3 may be detected must be devised. The method employed involves observing the change in capacitive balance when the generator terminals are interchanged. At balance the ratio of the capacitances will be determined essentially by the ratio of the resistive arms. If R_3 and R_A are asymmetrically shunted, upon interchange of the generator terminals the capacitive balance will change. With the generator connected as originally shown in figure 1 (i.e., J_1 connected to point W in the bridge), the value of C_s at balance will be called C_{s0}. The value of C_s at balance after interchanging the generator connections (with C_B unchanged) is called C_{si}. From eq (6) with $C_g=\infty$, $J_1=J_L$, and $J_2=J_K$, the ratio of the resistors shunting R_3 and R_A is given to a close approximation by

$$\frac{J_L}{J_K}=1-\frac{(C_{s0}-C_{si})}{2C_B}\left(1+\frac{J_L}{R_A}\right), \tag{43}$$

where J_L represents the resistance shunting R_3 in the original bridge-generator connection. The departure of J_L/J_K from unity is therefore directly proportional to $(C_{s0}-C_{si})/2C_B$. Thus, measurements of $(C_{s0}-C_{si})$ and of K are sufficient to determine J_K and J_L.

[13] Even with $C_g=1\ \mu f$ at frequencies near 100 cps K is $J_2/(J_2+R)=0.136$. This means that the capacitive coupling through C_g is sufficient to effectively shunt R_A by J_2. Near 0.1 cps, however, the value of K is unity, implying that this capacitive coupling is no longer effective. At about 3 cps, where $Z_g\cong 10^5$ ohms, the "crossover" between these two extremes occurs.

The results of these experiments are shown in figures 3 and 8. In figure 3 the curves are calculated from eq (13), which gives K as a function of frequency. The experimental points fall on the calculated curves to within the experimental error. Note that with $C_g=1\ \mu f$, K is unity near 0.1 cps, indicating that there is no effective resistive shunt across R_A. Near 100 cps, K becomes essentially 0.136 as predicted. With $C_g=\infty$, K remains near 0.136, indicating a frequency-independent 15.8 kohm shunt.

At frequencies near 100 cps, the value of K was also experimentally determined with $C_g=0.1\ \mu f$ and $0.01\ \mu f$. This was done to obtain a more sensitive test for stray resistive shunting at high frequencies. These points also fall on the calculated curves to within the experimental error. Therefore up to 100 cps *the stray impedances within the generator give rise to no significant resistive shunt on* R_A. Even a 10^6 ohm shunt across R_A will have no noticeable effect upon the results if the substitution method is employed, particularly if one operates the bridge with $C_g=\infty$.

Figure 8 gives the results of measurements of the change in capacitance balance, upon interchange of the generator-to-bridge connections. The experimental points for $C_g=0$ indicate that no asymmetric resistive shunting exists up to a frequency of 100 cps. Above 100 cps such shunting is evident with $C_g=0$. With $C_g=1\ \mu f$ or $C_g=\infty$, the effect of this asymmetric shunt is lessened, and becomes evident only above 200 cps.

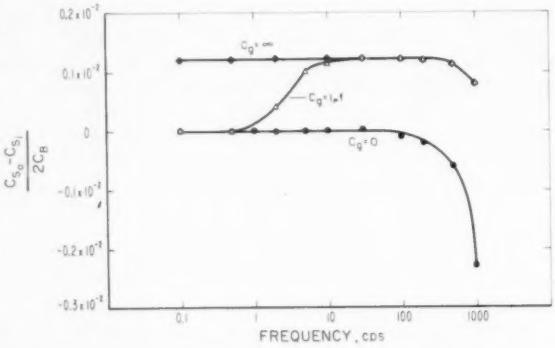

FIGURE 8. *The change in capacitance balance* $(C_{s_0}-C_{si})$ *upon interchange of the bridge-generator connections.*

The change in capacitance balance with interchange of the generator to bridge connection, according to eq (43), serves as a measure of the unbalance of resistive shunts arising within the generator and placed across R_3 and R_A.

Below 200 cps, with $C_g=\infty$, the value of $(C_{s0}-C_{si})/2C_B$, is independent of frequency and is 0.00122. From this one may compute the value of r by using eq (43). Substituting we have:

$$r=\frac{J_1}{J_2}=1-0.00122\left(1+\frac{1.58\times 10^4}{10^5}\right),$$

giving $r=0.99859$.[14]

[14] The ratio r was also determined by an independent d-c technique which gave $r=0.99860\pm.00005$.

The experimental points for $C_x=1$ μf clearly show the "crossover" between asymmetric shunting by J_1 and J_2 at high frequencies, and no shunting at low frequencies.

In summary, it has been shown, through measurements of K and $(C_{s0}-C_{s1})/2C_B$, that the resistance shunting the bridge arms due to the stray impedances in the generator, is most certainly greater than 10^6 ohms, and that *below* 100 cps *such resistive shunting that may exist is symmetrical to within the requirements of this apparatus.*

b. Capacitive Shunts across the Ratio Arms

Any capacitive shunt originating from the stray generator impedances Z_1, Z_2, and Z_L and placed across R_3 and R_4 are included in the total capacitance across these arms, C_3 and C_4 respectively. In appendix 7.4 the value of C_4 is found to be about 1400 pf at 100 cps. It is necessary to know C_4 in order to evaluate the correction term in the conductance equation (eq (23)). It is shown in section 3.2a, eq (21) that (C_3-C_4) can be made zero at 100 cps by adjusting the variable capacitor across R_3. This adjustment eliminates, at high frequencies, a correction term involving (C_3-C_4) from the capacitance equation (eq (22)). However, since C_3 and C_4 contain components which are possibly frequency dependent, it is necessary to verify that (C_3-C_4) remains zero at lower frequencies.

An attempt was made to determine (C_3-C_4) at 0.5 cps by measuring the magnitude of the correction term $(C_3-C_4)\,K\Delta R_1/R_2$ in eq (10). At 0.5 cps, the sensitivity of the Ultrohmeter is best, and with $C_x=1\mu f$, K is near the maximum value of unity. The experimental procedure employed was to first balance C_3 and C_4 at 100 cps. Then at 0.5 cps a substitution measurement of the parallel capacitance of a suitable resistor is made. The quantity

$$C_{mo}=C_x-(C_3-C_4)K\frac{\Delta R_1}{R_2}=\Delta C_s+C'_s\frac{\Delta R_1 K}{R_4}+(R_3-rR_4-R''_1)\frac{\Delta R_1}{R_2}L \quad (44)$$

is then determined from eq (10). Next the generator-to-bridge connections are reversed and C_3 and C_4 balanced once again at 100 cps. Interchanging the generator connection interchanges the generator's contribution to C_3 and C_4. Thus, if (C_3-C_4) is positive at 0.5 cps, upon interchanging it will be negative. Measuring the capacitance of the resistor once again at 0.5 cps one may compute

$$C_{mi}=C_x+(C_3-C_4)K\frac{\Delta R_1}{R_2}=\Delta C_s+C'_s\frac{\Delta R_1 K}{R_4}+\left(R_3-\frac{R_4}{r}-R''_1\right)\frac{\Delta R_1}{R_2}L, \quad (45)$$

from eq (10), with J_1 and J_2 interchanged.[15]

Subtracting C_{mi} and C_{mo} we have

$$C_{mi}-C_{mo}=2(C_3-C_4)K\frac{\Delta R_1}{R_2}. \quad (46)$$

Thus, (C_3-C_4) may be determined.

Measurements were made upon a nominal 10^{10} ohm resistor. This value was chosen as a compromise between two conflicting factors. One must attempt to minimize R_2 so as to make the correction term large, and at the same time maximize R_2 so that best sensitivity to capacitative unbalance is achieved. A compromise is achieved with a value of R_2 of 10^7 ohms. At 0.5 cps, with $R_2=10^7$ ohms, the capacitance can be balanced to about ± 0.005 *pf*. If ΔR_1 =100 ohms the magnitude of $\Delta R_1/R_2$ will be 10^{-5}, which corresponds to a value of 10^{10} ohms for R_x.

The experimental data obtained upon performing this experiment are given in table 4. The experiment was performed twice using two values for C'_s (100 pf and 20 pf). The difference between the average values of C_{mi} and C_{mo} was [0.0755−0.0725] pf=0.003 pf. This is within the experimental accuracy of ± 0.005 pf. If we take this number at its face value, we can compute from eq (46) a value of about 200 pf for (C_3-C_4). If (C_3-C_4) is 200 pf

[15] With J_1 and J_2 interchanged the factor $(R_3-rR_4-R''_1)$ in eq (10) becomes $(R_3-R_4/r-R''_1)$ which, upon evaluation, gives $(-71$ ohms$-R''_1)$. The magnitude of this term depends strongly upon accurate knowledge of the values of R_3, R_4, and r.

TABLE 4. *The parallel capacitance (C_m) of a nominal 10^{10} ohm resistor measured before and after interchanging the generator to bridge connection*

Generator connection	C'_s(pf)	ΔC_s(pf)	$\Delta R_1/R_2$	a(pf)	b(pf)	C_m(pf)
Ordinary	100. 000	−0. 003	74. 3/10^7	0. 072	0. 005	0. 074
Ordinary	20. 000	+0. 052	74. 5/10^7	. 014	. 005	. 071
Interchange	100. 000	. 010	74. 5/10^7	. 072	−0. 005	. 077
Interchange	20. 000	. 065	74. 5/10^7	. 014	−0. 005	. 074

a$=K\Delta R_1\,C'_s/R_4$; b$=(R_3-rR_4-R''_1)\;\Delta R_1 L/R_2$, ordinary; b$=(R_3-R_4/r-R''_1)\;\Delta R_1 L/R_2$, interchange; $C_m=\Delta C_s+$a+b; and $R''_1=\Delta R_1$.

These data, obtained at 0.5 cps, together with eq (46), indicate that (C_3-C_4) remains negligibly small at low frequencies.

at 0.5 cps, with $C_g=\infty$, the maximum value of the correction term $(C_3-C_4)\ \Delta R_1 K/R_2$, is obtained with $R_2=10^6$ ohms and is less than 0.003 pf. This is well below the uncertainty in capacitive balance under similar conditions, which is determined from eq (34) as ± 0.06 pf. Therefore, (C_3-C_4) *remains sufficiently low that its effect upon capacitance measurements is always less than the limits of sensitivity.*[16]

5. Measurements upon Dielectric Materials

As a final check upon the performance of the bridge (particularly near the high frequency end) measurements were made upon dielectric specimens and compared with results obtained using a two terminal Schering bridge (General Radio 716–C).

The two materials chosen were polymethylmethacrylate (PMMA), which has a fairly high value for the loss index (ϵ''); and a specimen of fused silica, which has a low loss index. These specimens were circular disks whose physical dimensions are given in table 5.

TABLE 5. *Dimensions of the disk shaped dielectric specimens*

Material	Thickness	Area of plane face	C_v
PMMA	0. 1627 cm	11. 310 cm²	6. 155 pf
Fused silica	. 1435 cm	7. 554 cm²	4. 661 pf

In order to eliminate series air films, the plane surfaces of the PMMA specimens were covered with tin-foil-petrolatum electrodes while the fused silica specimen received electrodes of evaporated gold.

A brief description of the experimental technique used in measuring ϵ' and ϵ'' follows. (A more complete description is given in ref. [7].) A micrometer holder, having plane circular electrodes 2 in. in diameter was employed. The diameters of the specimens were less than that of the electrodes in order to assure that the field within the specimen was uniform. The dielectric constant is computed from the measured parallel capacitance, C_x, according to the equation

$$\epsilon'=\frac{C_x-C_h}{C_v}+\frac{t_s}{t_h}, \tag{47}$$

where t_h is the separation of the electrodes with the sample between, t_s is the specimen thickness, and C_h is the capacitance of the holder measured without the specimen in place and with the electrode separation equal to t_h. The loss index is obtained from eq (37).

The results of measurements made at room temperature upon the PMMA specimen are shown in figure 9. No visible discontinuity exists in the data obtained on the two bridges. The data in the region in which the frequencies overlap is also presented in table 6. The maximum difference in ϵ' is 0.0016. This is a difference of only 0.05 percent. The values of ϵ'' agree to within 0.2 percent.

TABLE 6. *Comparison of dielectric constant and loss index obtained on the low frequency apparatus and on a Schering bridge for PMMA.*

Frequency	ϵ'		ϵ''	
	L. F. bridge	Schering bridge	L. F. bridge	Schering bridge
cps				
50	3. 3625	3. 3617	0. 2060	0. 2064
75	3. 3089	3. 3080	. 1961	. 1965
100	3. 2733	3. 2717	. 1879	. 1877

Results for the specimen of fused silica are presented in figure 10. The difference in the values of ϵ' obtained on the two bridges is, as before, 0.05 percent. The ϵ'' data of figure 10 may be joined by a smooth curve even though there is a difference of 0.00035 in the values measured at 100 cps. This difference is well within the stated accuracy of the Schering bridge, and may thus be largely associated with the scatter of the Schering bridge data. The values of ϵ'' obtained on the low frequency apparatus fall within 0.0001 of the drawn curve, which is in keeping with our calculated accuracy of $\pm\ (1\%+5\times 10^{-4}/C_v(\text{pf}))$.

6. Comments and Discussion

It has been demonstrated (section 4.2) that the stray impedances in the generator Z_1, Z_2, and Z_L produce no ill effects upon the operation of the bridge. The fact that this is true for the particular generator employed does not necessarily imply that the same is true of another generator, even though it be of the same manufacture. If another generator were employed, it would be necessary to perform those experiments which demonstrate the effects of those impedances.

It has been shown that it is preferable to operate the bridge with C_g of figure 1 shorted. In this mode of operation, where eqs (22) and (23) apply, the correction terms are small in magnitude and essentially frequency independent.

In its present state, this apparatus can be profitably employed to investigate the dielectric properties of materials at low frequencies. The present meas-

[16] A mathematically simplified method of measuring C_3-C_4 is given here. If one replaces C_g with a resistor R_g, then (C_3-C_4) can be measured at low frequencies without using eq (10) which contains frequency dependent terms. If $R_g=500$ kohms, then eq (22) is valid if one uses a larger value of K. (R_g is inserted in order to increase K and thus increase the correction term containing (C_3-C_4).) The value of K becomes $R_m/(R_m+R_4)$ where R_m (the equivalent resistance shunting R_3) is $J_2+R_g(1+J_2/J_1)$. Since $J_2=15.8$ kohms, $J_2/J_1\cong 1$, and $R_g=500$ kohms, then $R_m=1.016\times 10^6$ ohms and $K=0.91$.

The experimental procedure outlined previously is unchanged but now from eq (22),

$$C_{m0}=\Delta_0'C+C_t'K\frac{\Delta R_1}{R_4}=C_x-(C_3-C_4)K\frac{\Delta R_1}{R_2},\ \text{where } K=0.91.$$

This expression contains no frequency dependent correction terms, thus the analysis of the results obtained when the terminals are interchanged is simplified.

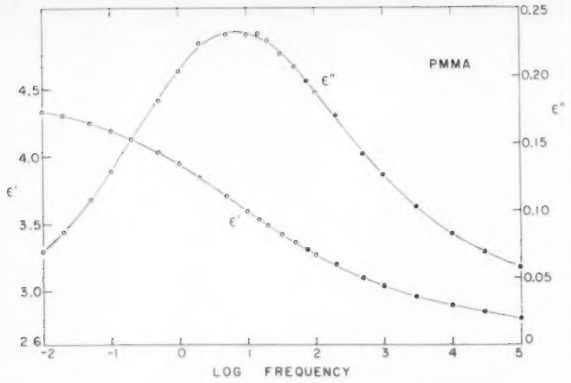

FIGURE 9. *Dielectric constant, ϵ', and loss index, ϵ'', versus log frequency for desiccated specimen of PMMA at 23.7 °C.*

○—low frequency apparatus
●—Schering bridge

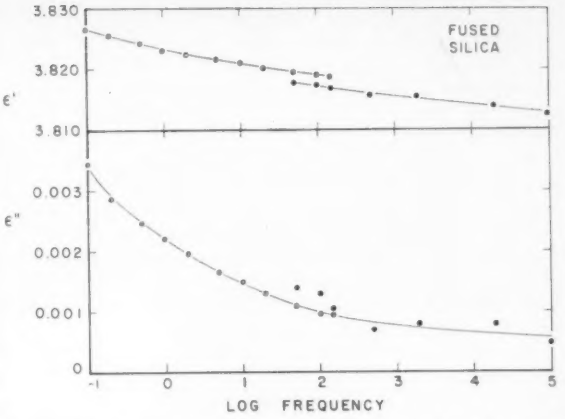

FIGURE 10. *Dielectric constant, ϵ', and loss index, ϵ'', versus log frequency for specimen of fused silica at 24.2 °C.*

○—low frequency apparatus
●—Schering bridge
The difference in the value of ϵ' measured on the low-frequency apparatus and that obtained on the Schering bridge at 100 cps is only 0.05%.

urable range of capacitances, 0 to 100 pf, could be extended through use of larger range variable capacitors, C_s and C_B. This alteration would make two minor changes in the behavior of the bridge. The correction terms of eqs (22) and (23), whose magnitude depends upon C_s', would be correspondingly increased, and the sensitivity to bridge unbalance would be decreased under certain conditions as shown in eqs (32) and (33).

The range of conductance presently measurable, 10^{-15} to 10^{-9} mhos, is adequate for most purposes. It is appropriate, however, to consider means whereby higher values of conductances may be measured. Since $G_x=\Delta R_1/R_2R_4$, higher values of conductance may be measured by decreasing R_2 and/or R_4, or by increasing ΔR_1.

Eqs (22) and (23) remain adequate approximations if any of the above alternations are made. If R_4 is lowered to 10^4 ohms, the correction term $C_s'\Delta R_1K/R_4$, of eq (22), would increase from a maximum of 0.019 pf to 0.85 pf. A correction term of this magnitude is almost too large to be tolerated. Furthermore, if R_4 were 10^4 ohms, the correction term of eq (23) would become almost doubled in magnitude. Decreasing R_4 is therefore not recommended.

If the minimum value of R_2 were made 10^5 ohms, and R_4 remained 10^5 ohms, conductances of 10^{-8} mhos could be measured, and the correction terms of eqs (22) and (23) would not be altered. It should be mentioned, however, that if R_2 were 10^5 ohms, the capacitive sensitivity at low frequencies would suffer severely. (See eq (33) or eq (36)).

If the range of ΔR_1 were increased to 10^3 ohms, the following effects would result. From eq (23), it is apparent that conductances previously measurable with a particular value of R_2 would become measurable on the next higher value. Therefore, under most circumstances, the sensitivity to capacitance unbalance would increase (see eq (36)). If ΔR_1 were increased to 10^3 ohms, however, the maximum value of the corrections in eq (22) would be increased by a factor of ten. The maximum of $C_s'\Delta R_1K/R_4$ would become 0.189 pf, which is not excessively large.

Either of the last-mentioned alterations offer possibilities of increasing the range of measurable conductances without adversely affecting bridge accuracy. If used together; i.e., $R_2=10^5$ ohms, $\Delta R_1=10^3$ ohms, while $R_4=10^5$ ohms, conductances as high as 10^{-7} mhos could be measured.

It is informative to compare the performance of this apparatus with that of other low-frequency bridges. In table 7 the frequency range, the capacitance and conductance ranges, and the sensitivity of this apparatus is compared with that of two other bridges. Referring to table 7, it is apparent that the apparatus studied here (a) may be operated about a decade higher in frequency, (b) has better conductance sensitivity and (c) has, in general, better capacitance sensitivity. Both the bridge of Weingarten and that of Nakajima measure capaci-

TABLE 7. *Comparison of three low frequency bridges*

Bridge	Conductance		Capacitance		Frequency range
	Range	Sensitivity [a]	Range	Sensitivity	
	(mho)	*(mho)*	*(pf)*	*(pf)*	*(cps)*
Weingarten [2]	10^{-5} to 10^{-14}	$\sim 5\times10^{-15}$	to 1000	~0.1	10 to 0.008
Nakajima [5]	10^{-7} to 10^{-13}	$\sim 10^{-13}$	to 800	~0.2	10 to 0.008
This apparatus	10^{-9} to 10^{-15}	$\sim 3\times10^{-16}$	to 100	~0.001	200 to 0.008

[a] The sensitivities given here are valid for frequencies near 0.1 cps. A detailed discussion of the sensitivity of this apparatus is given in section 3.5.

tances near 1000 pf. The present bridge may be modified to do so also. The bridge of Nakajima can measure conductances as high as 10^{-7} mhos. Alterations of the present bridge, whereby conductances of this magnitude can be measured, have previously been discussed.

The present bridge has been subjected to a detailed theoretical and experimental analysis, which gives confidence, within the limits stated, in the absolute values of the dielectric properties obtained with it. It is well suited to the investigation of dielectric relaxation phenomena in materials where the loss is low, and where molecular mechanisms lead to long relaxation times.

7. Appendix

7.1. Derivation of the Bridge Balance Equation [17]

Referring to figure 2(b) we see that the Y network consisting of J_1, Z_g, J_2 may be transformed into a Δ network containing an impedance across Z_3 which we shall call Z_n and an impedance across Z_A which we shall call Z_m.

The transformation equations are

$$Z_n=J_1+Z_g\left(1+\frac{J_1}{J_2}\right)$$
$$Z_m=J_2+Z_g\left(1+\frac{J_2}{J_1}\right). \tag{A-1}$$

The balance equations of the resulting Wheatstone network can be written as

$$\left[\frac{Z_3Z_n}{Z_3+Z_n}\right]Z_B=\left[\frac{Z_AZ_m}{Z_A+Z_m}\right]Z_P \tag{A-2}$$

Setting $J_1/J_2=r$, substituting for Z_n and Z_m in this expression one obtains the balance condition stated in eq (2), i.e.

$$\frac{1}{Z_P}\left[r+\frac{Z_g}{Z_A}(1+r)+\frac{J_1}{Z_A}\right]=\frac{1}{Z_B}\left[1+\frac{Z_g}{Z_3}(1+r)+\frac{J_1}{Z_3}\right]. \tag{A-3}$$

7.2. Exact Solutions of the General Bridge Equations

The exact solutions of the bridge balance equations with C_g in the circuit are obtained by combining eqs (6), (7), (8), and (9) and solving for C_x and $1/R_x$. The solution for C_x is

$$C_x=C_s'-C_s''+A+B+C+E \tag{A-4}$$

where

$$A=\frac{C_g'}{D}\left(\frac{1}{R_A'}-\frac{1}{R_A''}\right)R_A''\left[1+\frac{R_A''}{R_B'}+\frac{\omega^2R_A''J_1C_g^2}{(1+r)^2}\left(r+\frac{J_1}{R_A''}+\frac{J_1}{R_B'}\right)\right]$$
$$-\frac{C_B}{D}\left(\frac{1}{R_B''}-\frac{1}{R_B'}\right)R_A''\left[\frac{R_A''}{R_3}+\frac{\omega^2R_A''J_1C_g^2}{(1+r)^2}\left(1+\frac{J_1}{R_3}\right)\right],$$

$$B=\frac{C_g}{D}\left(\frac{1}{R_B''}-\frac{1}{R_B'}\right)\frac{R_A''}{(1+r)}\left[1+\frac{R_A''}{R_B'}-\frac{rR_A''}{R_3}\right],$$

$$C=\frac{C_3}{D}\left(\frac{1}{R_B''}-\frac{1}{R_B'}\right)R_A''\left[1+\frac{R_A''}{R_B'}+\frac{\omega^2R_A''J_1C_g^2}{(1+r)^2}\left(r+\frac{J_1}{R_A''}+\frac{J_1}{R_B'}\right)\right]$$
$$-\frac{C_4}{D}\left(\frac{1}{R_B''}-\frac{1}{R_B'}\right)R_A''\left[\frac{R_A''}{R_3}+\frac{\omega^2R_A''J_1C_g^2}{(1+r)^2}\left(1+\frac{J_1}{R_3}\right)\right],$$

and

$$E=\frac{1}{DR_s}\left(\frac{1}{R_A''}-\frac{1}{R_A'}\right)\frac{C_gR_A''^2}{(1+r)}\left[r+\frac{(1+r)(C_4+C_B)}{C_g}+\frac{\omega^2J_1^2C_g(C_4+C_B)}{(1+r)}\right].$$

The expression for the conductance is

$$G_x=\frac{1}{R_x}=\frac{1}{R_B''}-\frac{1}{R_B'}+M+N+O+P+Q, \tag{A-5}$$

where

$$M=\frac{1}{D}\left[C_g'\left(\frac{1}{R_A'}-\frac{1}{R_A''}\right)-C_B\left(\frac{1}{R_B''}-\frac{1}{R_B'}\right)\right]\left[\omega^2R_A''^2C_g\left(\frac{C_4}{C_g}+\frac{r}{(1+r)}\right)+\frac{\omega^4\tau_1^4}{(C_4+C_B)}\right],$$

$$N=\frac{(C_3-C_4)}{D}\left(\frac{1}{R_B''}-\frac{1}{R_B'}\right)\left[\omega^2R_A''^2C_g\left(\frac{C_4}{C_g}+\frac{r}{(1+r)}\right)+\frac{\omega^4\tau_1^4}{(C_4+C_B)}\right],$$

$$O=\frac{1}{D}\left(\frac{R_A''}{R_3}-1-\frac{R_A''}{R_B'}\right)\left(\frac{1}{R_B''}-\frac{1}{R_B'}\right)\left[1+\frac{\omega^2J_1R_A''C_g^2(r+J_1/R_A'')}{(1+r)^2}\right],$$

$$P=\frac{(1-r)}{D}\left(\frac{1}{R_B''}-\frac{1}{R_B'}\right)\frac{\omega^2R_A''^2C_g^2}{(1+r)^2}\left[\frac{J_1}{R_A''}+r+(1+r)\frac{C_4}{C_g}\right],$$

[17] The author wishes to thank F. K. Harris for suggesting this derivation of eq (A-3).

and

$$Q=\frac{R''_A}{DR_s}\left(\frac{1}{R'_A}-\frac{1}{R''_A}\right)\left[1+\frac{\omega^2 J_1 R''_A C''^2_g}{(1+r)^2}\,(r+J_1/R''_A)\right].$$

In eqs (A-4) and (A-5), D is given by

$$D=1+R''_A/R'_B+\omega^2\tau_0^2+\omega^4\tau_1^4, \tag{A-6}$$

where

$$\tau_0^2=\frac{C''^2_g R''^2_A}{(1+r)^2}\left[\left(r+\frac{J_1}{R''_A}+(1+r)\,\frac{C_4}{C_g}\right)^2+\frac{J_1}{R'_B}\left(r+\frac{J_1}{R''_A}\right)+\frac{(1+r)C_B}{C_g}\left(r+(1+r)\,\frac{C_4}{C_g}\right)-\frac{2J_1C_4(1+r)}{R''_A C_g}\right]$$

and

$$\tau_1^4=C''^2_g C_4(C_4+C_B)R''^2_A J_1^2/(1+r)^2.$$

Approximate solutions with $C_g=1\mu f$. Let us now evaluate the various terms of eqs (A–4) and (A–5) and drop those which are clearly unimportant. We shall deal first with the case wherein C_g is 1μf and begin by evaluating $\omega^2\tau_0^2$ and $\omega^4\tau_1^4$. In order to do so we must obtain the value of C_4. In appendix 7.4, C_4 is determined to be 1450 pf ±10 percent. Additional leads may be employed in the future, thus increasing C_4. It will however, be assumed that $C_4\leqq 2000$ pf. Using the values for the constant parameters given in table 1, and the value of 0.99859 for r, (determined in section 4.2 a), we obtain $\omega^4\tau_1^4\leq 3.89\times10^{-9}f^4$. Since $R'_B\geq 10^9$ ohms, $R''_A\simeq R_4\simeq 10^5$ ohms, and $C_B\leq 125$ pf, the expression for $\omega^2\tau_0^2$, to an accuracy of about 0.8 percent, becomes

$$\omega^2\tau_0^2=\frac{\omega^2 C''^4_g J_2^2}{(1+r)^2}\left(1+\frac{R_4}{J_2}\right)^2. \tag{A-7}$$

Upon evaluation this becomes: $\omega^2\tau_0^2=0.132\ f^2$. At frequencies less than about 600 cps $\omega^2\tau_0^2\geq 100$ $(\omega^4\tau_1^4)$. Since the bridge is operated with $f<600$ cps, then $\omega^4\tau_1^4$ is negligible. To an accuracy of 0.8 percent or better, D is given by

$$D=1+\omega^2\tau_0^2. \tag{A-8}$$

In order to evaluate the terms in eqs (A–4) and (A–5) the following identities are used

$$\frac{1}{R'_A}-\frac{1}{R''_A}=\left(1+\frac{R_4}{R_2}\right)\frac{\Delta R_1}{R'_A R''_A}$$

$$\frac{1}{R''_B}-\frac{1}{R'''_B}=\frac{R_4}{R_2}\,\frac{\Delta R_1}{R'_A R''_A}. \tag{A-9}$$

These relationships are derived from eq (1) of section 3.2.

Since $R_s\geq 10^{11}$ ohms the quantity E in eq (A–4) contributes less than 0.001 pf and may therefore be omitted. The expressions for A, B, and C, which may contribute terms greater than 0.001 pf, may be reduced to the following with the aid of eqs (A–7) (A–8), and (A–9)

$$A'=C'_s\,\frac{\Delta R_1(1+\omega^2\tau_0^2+R_4/J_2)}{R_4(1+\omega^2\tau_0^2)(1+R_4/J_2)},$$

$$B'=\frac{C_g\Delta R_1(R_3-rR_4-R''_1)}{2R_4R_2(1+\omega^2\tau_0^2)}, \tag{A-10}$$

and

$$C'=(C_3-C_4)\,\frac{\Delta R_1(1+\omega^2\tau_0^2+R_4/J_2)}{R_2(1+\omega^2\tau_0^2)(1+R_4/J_2)}.$$

In eqs (A–10) use is made of the approximations

$$R''_A\simeq R'_A\simeq R_4\simeq R_3,$$

$$J_1\simeq J_2, \tag{A-11}$$

and

$$rC_g\gg(1+r)C_4.$$

The approximations (A–11) are accurate to about 0.1 percent. These approximations are not applied however in simplifying the expression $(1+R''_A/R'_B-rR''_A/R_3)$. From eq (1) this becomes $(R_3-rR_4-R''_1)/R_3$ to an accuracy of about ±10 ohms/R_3.

The expression for C_x becomes

$$C_x=C'_s-C''_s+A'+B'+C'. \tag{A-12}$$

Further evaluation of A', B', and C' is given in section 3.3.

In the equation for G_x, eq (A–5), it can be shown that the terms O and P will constitute less than 0.2 percent of G_x, and may be omitted since $|R''_A/R_3-1|<0.001$ and $(1-r)<0.002$. Also since $(C_3-C_4)<600$ pf (see section 3.2a), N is less than 0.2 percent of G_x and may be omitted if $f\leq 200$ cps. Q may be omitted to an accuracy of at least 0.1 percent since $R_s\geq 10^3 R_2$. M can become significant and is retained. Using eqs (A–7), (A–8), (A–9), and (A–11) the expression for the conductance may be written

$$G_x=\frac{\Delta R_1}{R_2R_4}\,[1+M'] \tag{A-13}$$

where

$$M'=\frac{C'_s R_2}{R_4C_g(1+J_1/R_4)^2}\left[\frac{\omega^2\tau_0^2}{1+\omega^2\tau_0^2}\right](2+\omega^2C_4C_gJ_1^2). \tag{A-14}$$

This expression for M' is accurate to at least 0.8 percent. Further discussion of eq (A–13) is given in section 3.3.

7.3. Exact Solutions of Bridge Equations with $C_g=\infty$

The bridge is ordinarily operated with $C_g=\infty$. The exact solutions, eqs (A–4) and (A–5), of the bridge balance conditions are simplified with $C_g=\infty$. The solution for C_x is

$$C_x=C'_s-C''_s+a+c+e \tag{A-15}$$

where

$$a=\frac{J_1}{d}\left[C'_s\left(r+\frac{J_1}{R''_A}+\frac{J_1}{R'_B}\right)\left(\frac{1}{R'_A}-\frac{1}{R''_A}\right)-C_B\left(1+\frac{J_1}{R_3}\right)\left(\frac{1}{R''_B}-\frac{1}{R'_B}\right)\right],$$

$$c=\frac{J_1}{d}\left(\frac{1}{R''_B}-\frac{1}{R'_B}\right)\left[C_3\left(r+\frac{J_1}{R''_A}+\frac{J_1}{R'_B}\right)-C_4\left(1+\frac{J_1}{R_3}\right)\right],$$

$$e=\frac{(C_B+C_4)}{d}\frac{J_1^2}{R_s}\left(\frac{1}{R''_A}-\frac{1}{R'_A}\right).$$

The conductance is given by

$$G_x=\frac{1}{R''_B}-\frac{1}{R'_B}+m+n+p+q, \qquad \text{(A-(16)}$$

where

$$m=\left[C'_s\left(\frac{1}{R'_A}-\frac{1}{R''_A}\right)-C_B\left(\frac{1}{R''_B}-\frac{1}{R'_B}\right)\right]\frac{\omega^2 J_1^2 C_4}{d},$$

$$n=\frac{(C_3-C_4)}{d}\left(\frac{1}{R''_B}-\frac{1}{R'_B}\right)\omega^2 J_1^2 C_4,$$

$$p=\left[(1-r)+\frac{J_1}{R_2}\left(1-\frac{R_3}{R''_A}\right)-\frac{J_1}{R'_B}\right]\left(\frac{1}{R''_B}-\frac{1}{R'_B}\right)\frac{(r+J_1/R''_A)'}{d}$$

$$q=\frac{J_1}{R_s d}\left(r+\frac{J_1}{R''_A}\right)\left(\frac{1}{R'_A}-\frac{1}{R''_A}\right),$$

and

$$d=\left(r+\frac{J_1}{R''_A}\right)^2+\frac{J_1}{R'_B}\left(r+\frac{J_1}{R''_A}\right)+\omega^2 J_1^2 C_4(C_4+C_B).^{18}$$

Approximate solution with $C_g=\infty$. With the aid of eq (1) and the values given in table 1, the factors in the expression for d can be evaluated. Noting that $J_1/R'_B<2\times10^{-5}$, and that $\omega^2 J_1^2 C_4\,(C_4+C_B)<2\times10^{-3}$ when f$\leq$200 cps, d becomes,

$$d=(r+J_1/R''_A)^2, \qquad \text{(A–17)}$$

to an accuracy of at least ±0.2 percent.

In eq (A–15), since $R_s\geq10^7$ ohms, the term e is less than 0.001 pf and may be omitted. The terms a and c, which may be greater than 0.001 pf, are simplified using eqs (A–9), (A–17), and (A–11), and become

$$a'=\frac{C'_s\Delta R_1}{R_4(1+R_4/J_2)},$$

$$c'=\frac{(C_3-C_4)\Delta R_1}{R_2(1+R_4/J_2)}. \qquad \text{(A–18)}$$

Our expression for C_x becomes

$$C_x=C'_s-C''_s+a'+c'. \qquad \text{(A19)}$$

Further discussion of eq (A–19) is given in section 3.4.

In the expression for G_x (eq (A–16)), the term p may be dropped since $|R_3/R_A-1|<0.001$ and $(1-r)<0.002$. Also, n may be omitted to an accuracy of 0.1 percent or better, since f$\leq$200 cps and $(C_3-C_4)<2500$ pf. The term q may be dropped since it is less than 0.1 percent when $R_s>R_2/100$. The quantity m, however, is not always negligible and must be retained.

Using eqs (A–9), (A–17), and (A–11) the expression for G_x may be written:

$$G_x=\frac{\Delta R_1}{R_4R_2}\,[1+m'], \qquad \text{(A–20)}$$

where

$$m'=\frac{C'_s R_2\omega^2 R_4 C_4}{(1+R_4/J_2)^2}. \qquad \text{(A–21)}$$

Detailed consideration is given eq (A–20) in section 3.4.

7.4. Measurement of C_4

The total capacitance, C_4, which shunts R_A, is best measured at 100 cps where the effects of a capacitive shunt will be most pronounced. To further enhance the relative importance of C_4, the effective value of the resistive ratio arm should be maximized. At 100 cps with either $C_g=\infty$ or $C_g=1$ μf, R_3 and R_A are effectively shunted by J_1 and J_2. If $C_g=0$ however, no resistive shunting of R_3 and R_A occurs, so that the equivalent resistance is maximized. Accordingly C_4 is best measured at 100 cps with $C_g=0$.

The method by which C_4 can be measured is developed from eqs (6) and (7). Setting $C_g=0$, these equations become

$$C_P=C_B\frac{R_A}{R_3}+C_3\frac{R_A}{R_B}-C_4\frac{R_A}{R_P} \qquad \text{(A–22)}$$

and

$$\frac{1}{R_P}=\frac{R_A}{R_BR_3}+\omega^2R_A(C_PC_4-C_BC_3). \qquad \text{(A–23)}$$

Substituting for $1/R_P$, eq (A–22) becomes:

$$C_P=C_B\frac{R_A}{R_3}+\frac{R_A}{R_B}\left[C_3-C_4\frac{R_A}{R_3}\right]-\omega^2C_4R_A^2(C_PC_4-C_BC_3). \qquad \text{(A–24)}$$

---

[18] The exact solutions of the bridge equations given by eqs (A–4), and (A–5) and by (A–15) and (A–16) are expressed in terms of the equivalent resistances of arms A and B, i.e., in terms of R_A and R_B. For the case where R_1 is a variable resistor, eqs (1) and (A–9) are used to evaluate terms containing R_A and R_B. However, if a different resistive device were employed to balance the conductance, eqs (A–4) and (A–5) or eqs (A–15) and (A–16) may still be employed. In particular, if R_1 were a resistive voltage divider whose variable contact was connected to R_2, these general equations would still apply. Equations similar to eqs (1) and (A–9) can be derived for the case wherein R_1 is a resistive voltage divider, and with these, the exact equations simplified.

The proposed use of a resistive voltage divider in place of a variable R_1 would tend to hold the total resistance of R_A more nearly constant thus reducing the magnitude of correction terms arising from changes in R_1.

If R_1 is set to zero, (so that according to eq (1), $R_B=\infty$), and the bridge is balanced by varying C_s and C_3, with no unknown in the circuit, eqs (A–22) and (A–23) give:

$$C'_s=C_BR_4/R_3,$$

and

$$C'_sC_4=C_BC'_3,$$

or

$$C_4=\frac{C_B}{C'_s}C'_3=\frac{R_3}{R_4}C'_3 \qquad \text{(A–25)}$$

Here we have assumed the parallel resistance of the capacitors C_B and C_s to be infinite. The values of C_s and of C_3 at balance are denoted as C'_s and C'_3 respectively.

If C_3 is now increased from C'_3 by an amount ΔC_3, the bridge may be rebalanced by adjusting R_1 and C_s. Equation (A-24) becomes

$$C'_s=C_B\frac{R''_A}{R_3}+\frac{R''_A}{R''_B}\left[C'_3+\Delta C_3-C_4\frac{R''_A}{R_3}\right]$$

$$-\omega^2C_4R''^2_A[C''_sC_4-C_B(C'_3+\Delta C_3)], \qquad \text{(A–26)}$$

where

$$R''_A\cong R_4+R''_1$$

and

$$R''_B\cong\frac{R_2R_4}{R''_1}.$$

Here C''_s and R''_1 represent the values of C_s and R_1 at balance after increase of C_3.

With the help of eqs (A-22) we may write

$$\left[C'_3+\Delta C_3-C_4\frac{R''_A}{R_3}\right]=\Delta C_3-C_4\frac{R''_1}{R_3}$$

$$[C''_sC_4-C_B(C'_3+\Delta C_3)]=C_4\Delta C_s-C_B\Delta C_3, \qquad \text{(A–27)}$$

where

$$\Delta C_s=C''_s-C'_s.$$

Substituting these quantities into eq (A-26) and subtracting (A-25) yields this solution for C_4

$$C_4=\frac{C_B\Delta C_3}{2\Delta C_s}-\frac{R''^2_1}{2R_2R_3R''^2_1\omega^2\Delta C_s}$$

$$\pm\frac{1}{2}\left\{\left[\frac{R''^2_1}{R_2R_3R''^2_1\omega^2\Delta C_s}-\frac{C_B\Delta C_3}{\Delta C_s}\right]^2\right.$$

$$\left.-\frac{4}{\omega^2R''^2_1}\left[1-\frac{C_BR''_1}{\Delta C_sR_3}-\frac{\Delta C_3}{\Delta C_s}\frac{R''_1}{R_2}\right]\right\}^{1/2} \qquad \text{(A–28)}$$

The experiment outlined above was performed at 100 cps, with $C_B=100$ pf and $R_2=10^6$ ohms. After the initial balance, C_3 was increased by 100 pf. The balance was restored when $\Delta C_s=0.099$ pf and R_1 was set to 38.8 ohms. Using these results, and the minus sign before the square root, the solution of eq (A-28) is

$$C_4=1450 \text{ pf}.$$

In order to test the accuracy of the method the experiment was repeated after adding 1000 pf to C_4. The result obtained for (C_4+1000 pf) was 2310 pf. Comparison of these values shows that the result for C_4 is accurate to about 10 percent. This accuracy is adequate for setting an upper limit on C_4.

The value of C_4 employed is

$$C_4=1450 \text{ pf}\pm 10\%. \qquad \text{(A–29)}$$

7.5. Bridge Circuit with Wagner Ground

If one desires to operate the bridge in such a manner that the generator's impedances to ground do not affect the balance conditions then a Wagner earthing device may be used as shown in figure 11. In this case the impedances J_1, J_2, and C_g (see fig. 1) have been removed from the generator. Stray impedances to ground which may exist in the generator are now in shunt with the arms of the Wagner ground consisting of R_7, R_8, and C_7, where their effects may be balanced out.

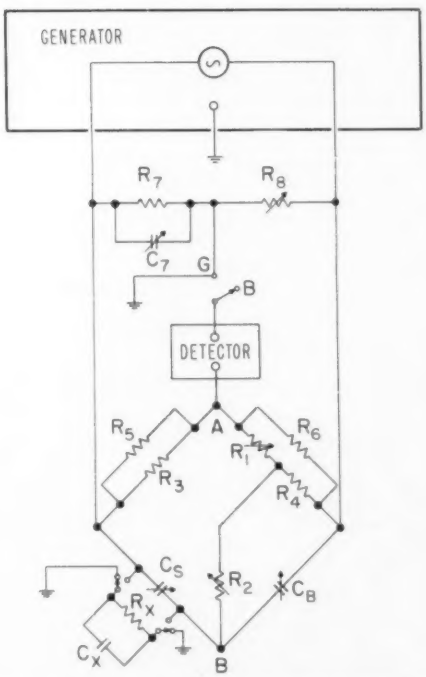

FIGURE 11. *Proposed circuit which includes a Wagner ground.*

C_s and R_s are the unknown impedances; C_B and C_B variable capacitors; $R_3=R_4=10^3$ ohms; $R_5=R_6=R_7=R_8=20$ kohm (R_8 variable); R_1, variable from 0 to 111 in 0.1 ohm steps; R_2 interchangeable 10^3 to 10^6 ohms; C_7, variable capacitor, 100 to 1000 pf.

With this circuit it is possible to balance out stray impedances to ground which may exist within the generator.

The circuit is balanced as follows: with the detector in position G, R_8 and C_7 are varied to achieve a null. With the detector in position B, C_s and R_1 are varied to attain a null. The change in R_1 will slightly affect the original balance so that balance with the detector at G will have to be reestablished, etc. The circuit is balanced when a null is obtained sumultaneously at points G and B. By repeating this balancing procedure with the unknown "out" and then "in", C_x and R_x may be determined in terms of the impedances C_s, R_1, R_2, R_3, R_4, R_5, and R_6. The solutions for the unknowns become to a very good approximation;

$$C_x = C_s' - C_s'' + \frac{C_s'(R_1'' - R_1')R_6}{R_4(R_6 + R_4)} \qquad \text{(A-30)}$$

and

$$G_x = \frac{R_1'' - R_1'}{R_2 R_4} \qquad \text{(A-31)}$$

Here it is assumed that the stray capacitances across R_5 and R_6 are less than 10 pf.

R_5 and R_6 are placed in shunt with R_3 and $(R_1 + R_4)$ respectively. Being lower in value they effectively determine the magnitude of the equivalent resistive ratio arms. Their purpose is to reduce the variation in the total value of the resistance of the arm which results from changes in R_1.

Twenty kilohms was selected as the magnitude of R_5, R_6, R_7, and R_8 so that the load on the generator would be comparable to that shown in figure 1. Perhaps lower values of resistance could be employed without overloading the generator but this point has not been investigated.

The sensitivity of this apparatus will be formally identical with that described previously by eqs (32) and (33) as long as coupling between points A and ground, and B and ground is negligible.

The author is grateful to F. K. Harris, F. R. Kotter, J. D. Hoffman, and William P. Harris for their constructive reviews of the manuscript. John I. Lauritzen, Jr., is given special acknowledgement for his participation in many helpful discussions.

---

8. References

[1] J. Volger, J. M. Stevels, and C. van Amerongen, Philips Res. Rept. 8, 452 (1953).
[2] I. R. Weingarten, Annual Report of the Conference on Electrical Insulation, 1955, Page 53. (More complete details on the low frequency bridge were obtained through private communication.)
[3] L. Heroux, J. App. Phys. **29,** 1639 (1958).
[4] R. H. Cole and P. M. Gross, Jr., Rev. Sci. Inst. **20,** 252 (1949).
[5] T. Nakajima, and D. Kondo, Bull. Electrotech. Lab. (Tokyo) **20,** 641 (1956).
[6] T. Nakajima, and S. Saito, J. Poly. Sci. **31,** 423 (1958).
[7] A. H. Scott, D. J. Scheiber, A. J. Curtis, J. I. Lauritzen, and J. D. Hoffman, Dielectric properties of semi-crystalline polychlorotrifluoroethylene (Manuscript in preparation).
[8] A. H. Scott, J. Research NBS **50,** 147 (1953).
[9] G. W. O. Howe, Wireless Engr. **12,** 291 (1935).
[10] B. V. Hamon, Proc. Inst. Elec. Eng. **99,** pt. IV (Monograph No. 27, 1952).

(Paper 65C1–52)

JOURNAL OF RESEARCH of the National Bureau of Standards—C. Engineering and Instrumentation
Vol. 65C, No. 1, January–March 1961

The Ephi System for VLF Direction Finding*

G. Hefley, R. F. Linfield, and T. L. Davis

(August 11, 1960)

A new system of VLF direction finding has been developed and tested by the National Bureau of Standards, Boulder, Colorado. The system has been named "Ephi" (E–ϕ) because the bearing of the transient signal is determined from the relative phase (ϕ) of the vertical electrical field (E) received at spaced antennas. The advantage of this scheme compared to conventional crossed-loop techniques is that it minimizes siting and polarization errors. A minimum of three antennas must be used to resolve directional ambiguity, and the preferrred antenna location is at the vertices of an equilateral triangle with baselines equal to $\frac{1}{3}$ to $\frac{1}{10}$ wavelength (at 10 kc). Appropriate phase detectors, delay lines and coincidence circuits are used to obtain a directional code in preset sectors. Within practical instrumentation limits any number of sectors of variable widths can be operated simultaneously and each can be rotated in azimuth.

1. Introduction

Direction-finding techniques used for the location of transient signals (such as sferics) usually employ crossed-loop antennas. The accuracy of such systems is limited largely by the siting and polarization errors involved.[1,2] A system of direction finding which has been developed by the National Bureau of Standards minimizes these errors, and has certain other features which make it particularly useful in various types of sferics studies. The new system has been named "Ephi" (E–ϕ) because the bearing of the transient signal is determined from the relative phase (ϕ) of the vertical electric field (E) received at spaced antennas.

In this system, spaced vertical antennas replace the loops and a minimum of three antennas must be used to resolve directional ambiguity. The antennas are closely spaced, preferably in the range of $\frac{1}{3}$ to $\frac{1}{10}$ wavelength. The relative time of arrival or phase of a signal at the antennas depends on the geometric configuration of the antennas and the direction of the signal source. In general, the optimum configuration for three antennas is at the vertices of an equilateral triangle. In this case, the sides of the triangle define the baselines of three hyperbolic grids with a mutual azimuthal spacing of 120 degrees.

Since the antenna spacing is a small fraction of a wavelength, differences in the immediate environment of the antennas are minimized. Experimental results thus far have not revealed any siting or environmental errors even when the individual antenna sites were purposely chosen with radical dissimilarities. The present experimental evidence, however, is not adequate to establish positively that siting errors are eliminated in this system.

A unique aspect of the Ephi system is that the relative time of arrival of signals from any direction or number of directions is anticipated rather than measured after recording. When finite tolerances are placed on the relative times of arrival which are anticipated, signals are accepted from a sector whose width is governed by the tolerances. Whenever a signal is received, a sector identification code is generated which may be used for selectively recording data with respect to direction. Within practical instrumentation limits any number of sectors of different widths can be operated simultaneously and independently of each other.

2. System Geometry

In a system using three antennas in the configuration of an equilateral triangle, the distance from a signal source to each antenna (fig. 1) is defined by the following equations:

$$d_A=\sqrt{R^2+r^2-2\,rR\,\cos\theta}$$

$$d_B=\sqrt{R^2+r^2-2\,rR\,\cos\,(120-\theta)}$$

$$d_C=\sqrt{R^2+r^2-2\,rR\,\cos\,(120+\theta)}.$$

The differences in the time of arrival of the signal at the antennas are proportional to the differences in the distance to the source.

$$(d_B-d_A)k=T_{B-A}$$

$$(d_C-d_B)k=T_{C-B}$$

$$(d_C-d_A)k=T_{C-A}$$

where $k\approx 5.37$ μsec/statute mile, the inverse velocity of radio wave propagation near the surface of the earth.

*Contribution from the Central Radio Propagation Laboratory, National Bureau of Standards, Boulder, Colo.

[1] F. Horner, The accuracy of the location of sources of atmospherics by radio direction-finding, Proc. IEE, **101**, 383, (1954).

[2] H. G. Hopkins and B. G. Pressey, Current direction-finding practice, Proc. IEE, **105**, 307, (1958).

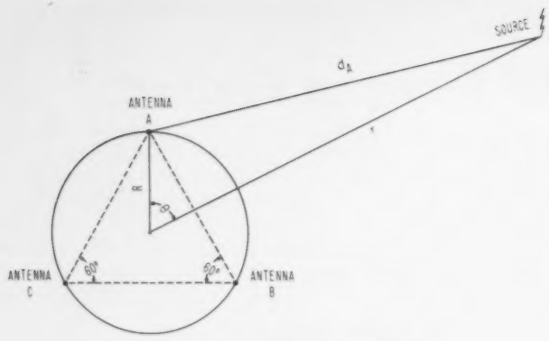

FIGURE 1. *System geometry.*

It is convenient to let the baseline $R\sqrt{3}$ equal unity. Figure 2 is a polar plot of the time or distance differences normalized to a baseline of unit length, with $r \gg R$. The exact values of these differences obviously depend on the ratio r/R, but when the distance to the source is 10 baseline units or more the condition $r \gg R$ is satisfied for most purposes. At a distance of 10 baseline units the values shown in the figure are in error by approximately 0.5 percent.

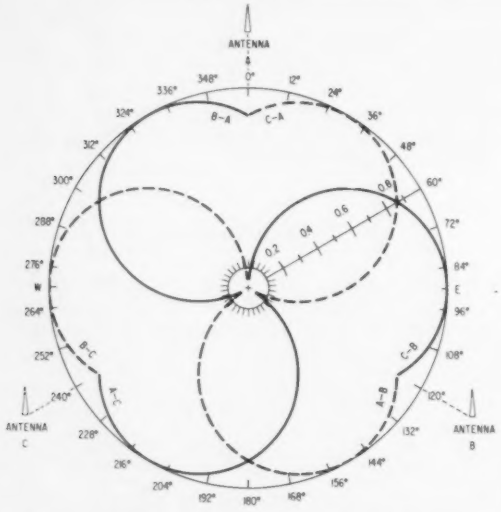

FIGURE 2. *Normalized time or distance differences.*

Since the antennas are closely spaced the differences in arrival time are small. It is, therefore, necessary to resolve these small differences rather precisely in order to provide satisfactory azimuthal sensitivity. The means by which this resolution is accomplished and the technique by which the direction of a signal is anticipated are interrelated and can best be explained together.

The significant steps in the process are:

1. Identical antennas and band-pass filters are used to derive pulses from the transient signals. A relatively large bandwidth (order of 60%) is required to provide short pulse rise and decay times.

2. The phase of the sinusoidal waveform or pulse is used to define the arrival time of the signal. The first axis crossing of the waveform is used to define a precise point in time which is independent of the amplitude of the signal, and a very short trigger is generated at this point.

3. A signal from a particular azimuth is recognized by introducing the delays required to produce coincidence. The early triggers are delayed in time until they are coincident with the trigger from the most distant antenna. These triggers then initiate rectangular waveforms as shown in figure 3. The time coincidence of the three waveforms is detected by circuitry which generates a new trigger. This indicates the occurrence of a signal at a particular azimuth and is produced as long as all three waveforms have full amplitude at any one time. The duration of the rectangular waveform, therefore, determines the width of the sector in which the signal must originate to produce a coincidence trigger.

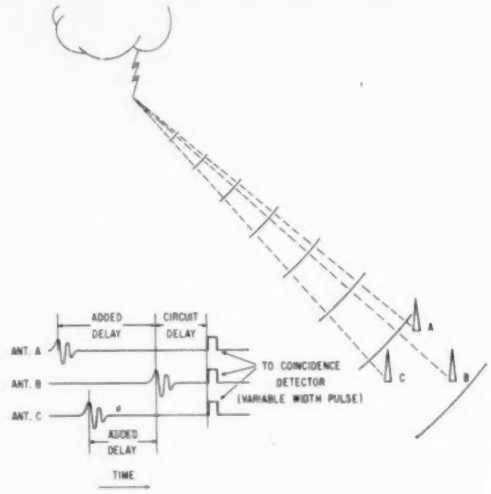

FIGURE 3. *Sector determination.*

The pulse width is also directly related to the baseline length. For example a 1-deg sector requires a pulse width of approximately 0.05 μsec with a 1-mile baseline, but the same sector width can be obtained with a 0.25 μsec pulse if a 5-mile baseline is used. The advantages of the longer baseline from an instrumentation standpoint are obvious.

The linear relationship between sector width and pulse width holds only for relatively small sector widths (less than about 12 deg), but since it is usually desirable to employ much narrower sectors the nonlinear effects will not be discussed.

Certain secondary azimuthal and range errors also limit bearing accuracy. There is a small cyclic change in sector width which varies with the azimuth setting, and another source of inaccuracy arises from the use of one set of delays for all ranges. In the experimental system the delays were computed for a 5,000 mile range. This introduces a calculable error

at other ranges but it is significant only in the vicinity of the antenna system. The error in bearing may amount to several degrees for sources only a baseline length away, but when the distance to the source is greater than about 10 baseline lengths the error becomes so small it may be neglected. With further refinement these systematic azimuthal errors could be reduced or eliminated by introducing appropriate correcting circuits in the equipment.

3. Instrumentation

The circuitry which is necessary to accomplish the basic functions described in the preceding section involves a very high degree of phase matching stability. The functional scheme of the system is shown in figure 4. The experimental equipment installed near Brighton, Colo. (about 20 miles northeast of the Denver airport) is shown in figure 5.

In the choice of antennas, two considerations are of major importance. First, the mutual impedance among the antennas must be negligible and second, the complex impedance of each antenna must be made as insensitive as possible to environmental changes. The mutual impedance is minimized by physical separation of the antennas and by extremely loose coupling between the antennas and the resonant circuits (see fig. 6).

The antennas which have been used to date are of the type shown in figure 7. The height is 125 ft and the measured capacity is approximately 515 $\mu\mu f$.

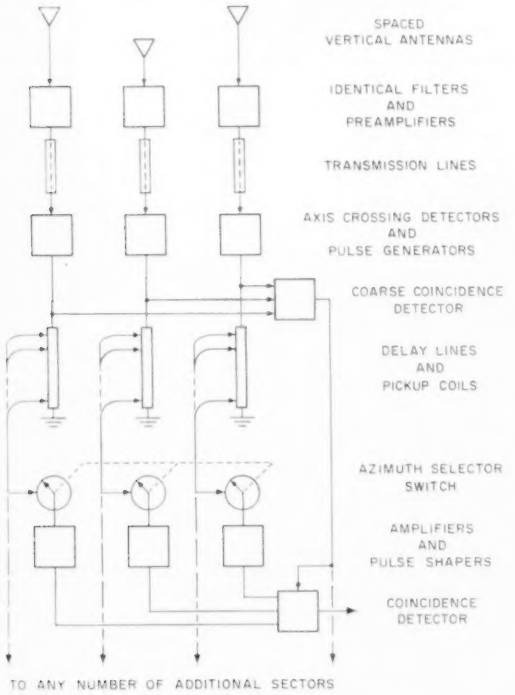

FIGURE 4. *Functional system diagram.*

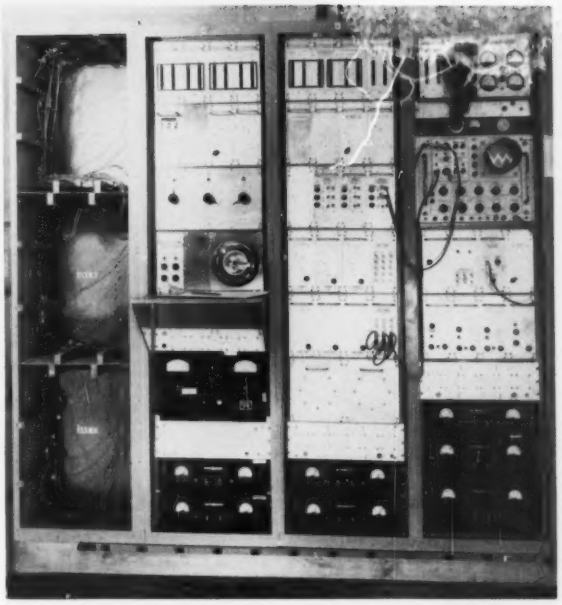

FIGURE 5. *Ephi equipment at Brighton station.*

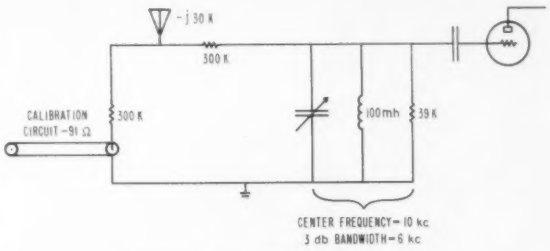

FIGURE 6. *Antenna coupling circuit.*

When an antenna of these proportions is used, the presence of a person near the base has very little effect on the antenna characteristics. Some further practical advantages of such a large antenna are that the magnitude of its impedance makes it more feasible to use passive circuit elements prior to the first grid thus reducing intermodulation by undesired signals. By virtue of the large effective height, very loose coupling can be used without degrading the overall noise figure of the receiving system.

The principal requirements for the preamplifiers, located at the base of each antenna, are large dynamic range and high power. The large dynamic range is necessary because of the widely varying amplitudes of the transient signals. High power is needed to insure a good signal-to-noise ratio at the receiving end of the transmission lines. While coaxial cable is used, it is not perfectly shielded and is, therefore, subject to pickup from power lines, and also the same transient signals received by the antennas induce small voltages in the transmission lines.

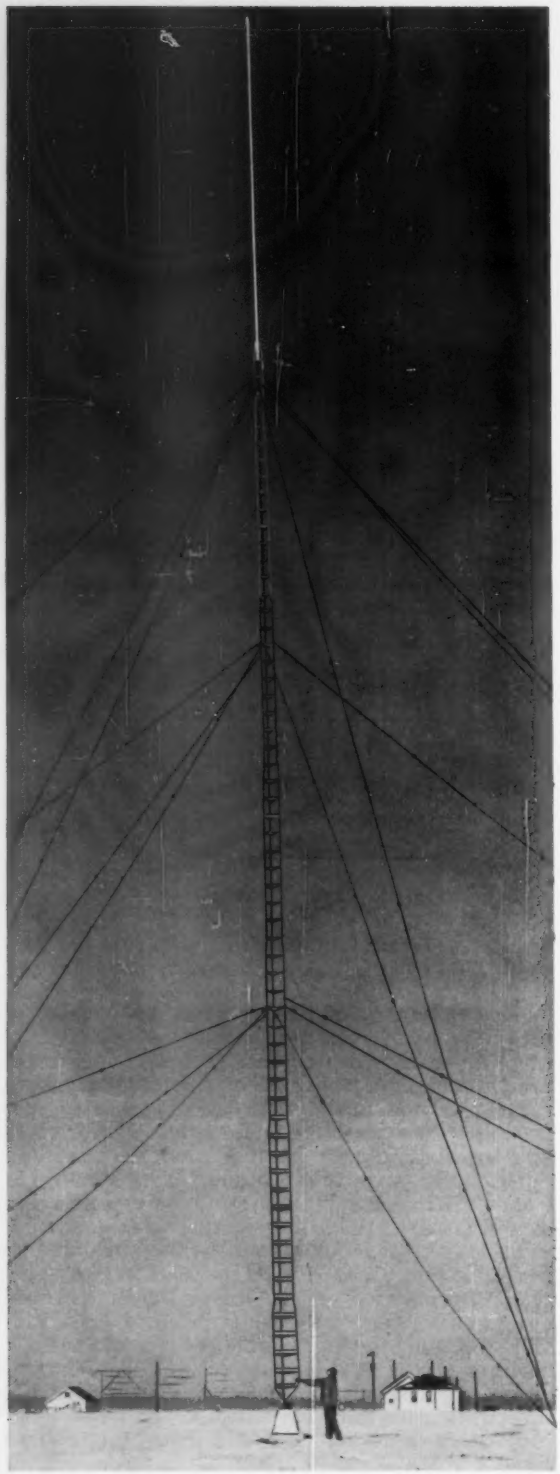

FIGURE 7. *Ephi system antenna.*

These voltages are similar to those from the antennas but are not in the same phase. As a result it is especially important that the undesired pickup be made negligible compared to the desired signals from the antennas.

The transmission lines leading from the preamplifiers to the centrally located equipment are adjusted so that transmission times are equal. These lines feed identical axis-crossing detectors and pulse generators. The basic functions of these circuits were described in the preceding section, but are shown in greater detail in figure 8. The first axis crossing of detectable amplitude defines the arrival time of the signal. The band-pass filtering which is done in part at the preamplifier and completed at the input to the axis-crossing detector produces a sinusoidal waveform of the nature shown in figure 8. Over a wide range of input levels the first axis crossing occurs within the linear range of the amplifiers. Saturation at the later axis crossings does not affect the amplifiers since these crossings are rejected by the coarse coincidence circuit.

The different steps in the coincidence detection process are shown in figure 9. The coarse coincidence detector selects the first complete set of axis-crossing triggers. In general, the first set will be complete, but regardless of how perfectly the three separate circuits are matched, a number of critical input levels exist which determine which axis crossing will produce the first trigger. At such critical levels all the axis-crossing detectors may not produce the first trigger at the same crossing as illustrated by the dotted trigger in figure 9b.

The duration of the coarse coincidence pulse is made somewhat greater than the maximum time difference. The coarse coincidence detection is, therefore, not a function of azimuth.

As indicated in figure 9d, when all four coincidence pulses are added, the combined amplitudes exceed a threshold. When this occurs a new trigger is generated which is used to signify the occurrence of a signal in that sector. To increase the reliability of the coincidence detector the pulses are added in a nonlinear manner. The circuit elements used to provide the nonlinear addition are shown in figure 10.

The cathode followers are biased so that maximum rated current is drawn in the absence of an input signal. In the arrangement shown, the cathode coupling resistors are relatively large but the cathode impedance of the tubes is maintained at a minimum. The negative going input pulses have large amplitude and drive the grids well beyond cutoff. When the tubes are cut off the output impedance rises to the value of the cathode coupling resistors.

The change in impedance of each tube is of the order of 10:1. Consequently, the output voltage which is supplied to the threshold detector is relatively small unless all four input pulses are in coincidence.

The triggers which mark the axis crossings are fed into three identical sets of tapped delay lines. These delay lines are shown functionally in figure 4

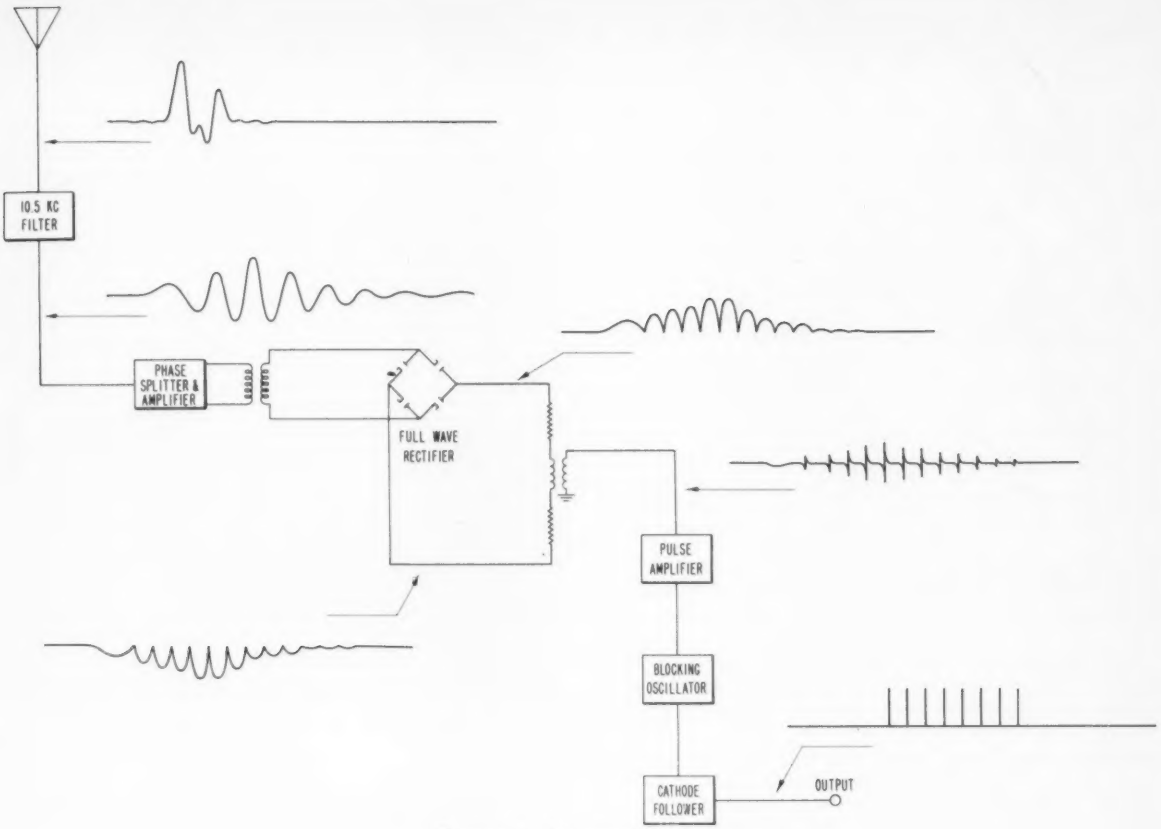

FIGURE 8. *Axis crossing detector.*

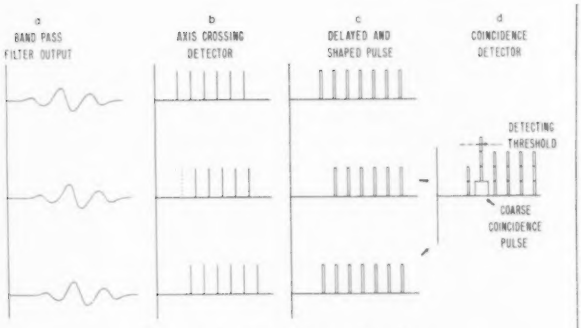

FIGURE 9. *Coincidence detection.*

while the actual lines used in the experimental equipment may be seen in the left hand cabinet in figure 5. The location of the taps is determined by the increment of azimuth desired between adjacent sectors and the time difference functions shown in figure 2. The desired combination of taps is selected by three switches mounted on a common shaft. An example of the delay values required for 6 deg increments of azimuthal switching is shown in figure 11.

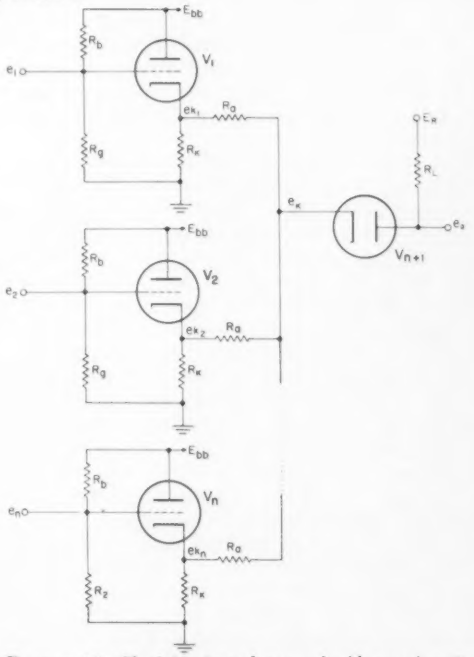

FIGURE 10. *Variable impedance coincidence circuit.*

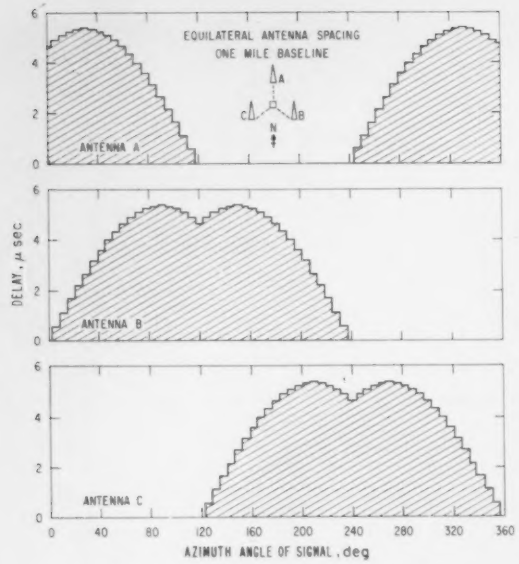

FIGURE 11. *Example of delay values required.*

The manner in which the delay lines are tapped is rather unique and is quite important from a standpoint of making the instrumentation practical. The delay line used is of the distributed constant, magnetic core type, which is commercially available in a wide range of delay and bandwidth characteristics. For this application, a particular virtue of the delay line is that it is not perfectly shielded. Consequently, when pulses at high amplitude are fed into the line they can be detected at any desired delay by a coil placed around the outside of the delay line. There is an attenuation of the order of 40 db between the delay line input and the pickup coil, but this loss is easily recovered by appropriate amplification.

The outstanding advantages of this method of tapping the delay line are that the taps can be located precisely at the desired delay point simply by moving them along the line, and (within practical limits) as many pickup coils as desired may be used on the same delay line because of the very loose effective coupling between the coils and line. Figure 12 is a photograph of the delay line and pickup coils for one antenna in the experimental equipment.

The location of the delay lines relative to the control panel at the Brighton Ephi station is shown in figure 5. The azimuth control switches for three sectors are located in the rack next to the delay lines. Each is a 3-section switch which controls the delay increments for all 3 antennas. Any number of additional sectors could be operated without additional delay lines or pickup coils, but each would require a separate amplifier, pulse shaper, coincidence detector, and another 3-section switch. The Brighton Ephi equipment provides for switching at 6-deg intervals of azimuth, however switching could be done at other intervals, with the proper number and placement of the pickup coils.

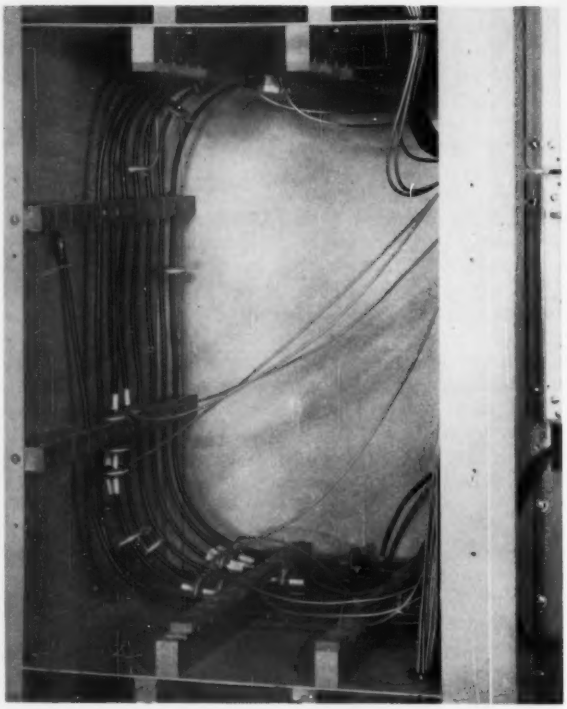

FIGURE 12. *Pickup coils on delay line.*

The pulses or triggers from any desired combination of pickup coils are amplified and used to trigger three identical, monostable multivibrators. These multivibrators produce the rectangular waveforms discussed earlier in connection with figure 3. In the discussion of system geometry it was assumed that these waveforms were perfectly rectangular. In practical circuitry the rise and fall times are finite but sufficiently short to warrant the assumption. In the experimental equipment these times are approximately 0.1 μsec and the duration of the waveforms is adjustable from approximately 0.2 to 7.0 μsec. With a 4-mile baseline (such as is used at Brighton) this is equivalent to a 1 to 40 deg range in the choice of sector widths.

It is evident that all the circuitry in the three separate channels from each antenna to the input of the coincidence detector is critical with respect to phase and time delays. While corresponding circuits are made as nearly identical as possible, each channel is provided with a separate phasing adjustment so the overall transmission times can be made identical. These phasing adjustments are made as follows:

A pulse signal generator, at the centrally located equipment is permanently connected to each preamplifier (see fig. 6) through coaxial cables of identical electrical length. The signal generator pulses, therefore, arrive at each antenna simultaneously.

This condition is equivalent to the occurrence of signals on the perpendicular bisectors of the three baselines defined by the antennas. Therefore, six headings at a mutual spacing of 60 deg are defined at which the different pairs of pulses at the input to the coincidence detector must be coincident. The phasing adjustments are used to achieve this condition.

At the same time the phasing adjustments are made the sensitivity of the three channels is also equalized. In sferic studies it is frequently desirable to measure simultaneously rates of occurrence relative to several threshold sensitivities. In order to do this the sensitivity of the sector channels is set equal to or slightly greater than the maximum sensitivity needed while the various threshold values are established separately.

4. Discussion

The Ephi system of direction finding is capable of appreciably greater accuracy than systems using crossed-loop antennas. Correlation of data obtained at the Brighton station with visual and radar weather observations has shown a high degree of bearing accuracy, but until a second Ephi station is completed, or a suitable artificial sferics generator becomes available, it will be difficult to make a precise determination of bearing errors. Present indications are that these errors will amount to less than 1 degree except for signal sources at very short distances from the Ephi station.

In addition to applications of a strictly direction-finding nature (such as the location of thunderstorm areas, hurricanes, etc.) the Ephi system provides a versatile tool for more general investigations of sferics. The triggers produced in the equipment when a sferic arrives from an accurately defined sector facilitate the use of oscilloscopes, counters, and other circuitry for studies such as the following:

1. Observation and photography of sferic waveforms.
2. Directional noise studies, or sferic rates as a function of azimuth.
3. Special analyses of the amplitude and phase of sferics.
4. Correlation of sferics with particular types of meteorological phenomena.
5. Propagation studies using transient signals.

When several sectors are used additional identifying or coding information can be obtained which further extends the variety of analyses possible.

The authors acknowledge the contributions of R. H. Doherty and E. L. Berger in the equipment development and the assistance of C. A. Samson in the preparation of this paper.

Most of this work was done for the Air Force Cambridge Research Center, Air Research and Development Command, CSO&A No. 58–28 (AFCRC).

(Paper 65C1–53)

JOURNAL OF RESEARCH of the National Bureau of Standards—C. Engineering and Instrumentation
Vol. 65C, No. 1, January–March 1961

Fast Counting of Alpha Particles in Air Ionization Chambers*

Z. Bay, F. D. McLernon, and P. A. Newman

(October 24 1960)

It was assumed in the past that counting of alpha particles in air-ionization chambers could only be based on the collection of ions since electrons produced in the alpha track quickly form negative ions in electronegative gases. This leads to time resolutions of the order of a millisecond. It is shown in the present work that the motion of the electrons before attachment produces a sharp initial rise in the pulse profile which, although small, can be detected and utilized for high speed counting. Time resolutions of the order of a few microseconds with good signal-to-noise ratios are realized in atmospheric air, and therefore counting speeds similar to those in non-electronegative gases are obtained.

1. Introduction

In ionization chambers containing electronegative gases the electrons produced by high energy particles are quickly captured forming negative ions. Since a counting operation consists of detecting voltage pulses caused by the motion of charges between opposite electrodes, it was generally assumed [1, 2] [1] in the past that the speed of such operations was limited by the drift velocities of ions, about 10^3 cm/sec at atmospheric pressure and 1 kv/cm field strength. Thus the total charge collection time for ions is of the order of a millisecond in chambers of usual design. The resolving time of a counting arrangement (chamber and electronic equipment) can be made less than a millisecond by the use of differentiation and pulse shaping techniques [1]. Using these techniques in preliminary experiments we have realized resolving times of about 0.1 millisecond for the counting of the alpha particles from Po^{210}. This limited speed of counting is especially disadvantageous for ionization work in air, which is electronegative due to its high concentration of oxygen. Since several of the ionization constants are defined or related to those in air, air is a very important gas in ionization work. Besides, air is the most convenient filling gas for an ionization chamber counter. Therefore, it seems desirable to achieve higher counting speeds in air.

It is well known that much higher counting speeds (shorter resolving times) for alpha particles can be achieved in ion chambers containing non-electronegative gases. In these the counting operation is based on the collection of electrons. Since the drift velocity of electrons under similar conditions is three orders of magnitude higher than that of ions, the dead time of such counters can be made as small as a few microseconds.

It appears that the possibility of increasing appreciably the speed of alpha counting in air ion chambers has been overlooked in previous work. Before attachment the electrons move with a high-drift velocity and thus produce a sharp rise in the pulse profile. Although small, this sharp rise can be detected. Basing the operation on this sharp pulse, one obtains time resolutions as small as a few microseconds, even in an ion chamber at atmospheric pressure. Thus counting speeds comparable to those in ion chambers with non-electronegative gases are achieved.

2. Estimated Electronic Pulse

In a parallel plate ionization chamber, the pulse, $P_e(t)$, due to the motion of electrons (neglecting the ionic motion) is given by [2]

$$P_e(t)=\frac{Q_e}{C}\frac{vt}{d}, \tag{1}$$

where t is the time, d the plate separation, C the chamber capacity, v the electron drift velocity and Q_e the total electronic charge.

According to data available [3, 4], it is a reasonable estimate that in air at atmospheric pressure and for field strengths of 1 kv/cm, electrons travel, on the average, a distance of the order of a millimeter before being attached. Thus with $\overline{vt}=0.1$ cm, $d=5$ cm, $C=10$ pf and $Q_e=2.4\times10^{-14}$ coulombs for about 5 Mev alpha particles, $P_e\sim50$ μv.

This estimate of $\overline{vt}$, and thus P_e, is uncertain due to inaccuracies in the electron attachment coefficient [5], h, (probability of attachment per collision) measured at reduced pressures and extrapolated to atmospheric pressure. Bradbury [6] has shown that h in O_2 and air is pressure dependent and recently Hurst and Bortner [7] have shown that α (the probability of attachment per cm per mm Hg pressure) in N_2–O_2 mixtures depends on the partial pressures of both gases.

*A preliminary report on this work was published in reference 11.
[1]Figures in brackets indicate the literature references at the end of this paper.

Due to the short path and high drift velocity, the electronic pulse rises to the height estimated above in approximately 0.1 μsec. This pulse can be taken as a step function for an amplifier with 400 kc/s bandwidth which gives an output pulse rise time of less than 1 μsec. It is known [1, 8, 9] that such amplifiers can be made to operate with input noise levels of a few microvolts. Therefore the above estimate indicates the possibility of using the electronic component of the alpha pulse for fast counting in air and observations verified this expectation.

3. Experimental Details

The construction of the ionization chamber and the block diagram of the electronic equipment is shown in figure 1. The grounded preamplifier chassis, *d*, supports the ionization chamber, providing for a short connection between the chamber electrode and the first grid. The high voltage plate, *a*, is a flat circular disk of 100 mm diameter. It is entirely supported by the high voltage cable jack, *e*, mounted on the grounded cylindrical housing, *c*. The Po^{210} alpha source, *h*, deposited on Palladium coated 25mm diameter silver disks (as used in the radioactivity standardization program at the National Bureau of Standards), is placed on the pulse electrode, *p*. Changing of sources can be quickly done by lifting the housing, *c*, without removing the chamber voltage. After replacing *c*, counting can be immediately resumed. The pulse electrode, *p*, is mounted in the center of the lucite plate, *g*, which also holds the guard ring, *f*. The guard ring is kept at dc ground potential through a 10^9 ohm resistor and serves to reduce the effective capacity of the pulse electrode to ground. The measured high frequency capacity of *p*, was 6 pf in this arrangement as compared with 12 pf in previous experiments without the guard ring.

In order to obtain rather high electric field strengths (~4 kv/cm) at relatively low chamber voltage (5–6 kv) the electrode separation (distance between *a* and *h*) was chosen about 1.5 cm. It is true that with this condition the alpha particles spend only a portion of their total energy (5.3 Mev, corresponding to a full range of 3.8 cm in atmospheric air) in the chamber gas producing ionization dependent upon the angle of emission; but this is permissible in counting experiments as dealt with in the present paper. In other experiments [10] where the counting of alpha particles was connected with a simultaneous measurement of the total ionization for Po^{210} alpha particles (and for which experiments the counting technique described here has been developed) the electrode separation was chosen longer than the full range and correspondingly higher chamber voltages (up to 20 kv) have been applied. Experiments showed that the small electrode separation as applied here still gives adequate signal-to-noise ratios even for the smallest alpha energy expended in the gas.

The chamber voltage (either positive or negative at plate A) is introduced through a smoothing RC "T" filter to diminish the ripple present in the output of the high voltage supply and to reduce pickup disturbances.

In the course of development two preamplifiers have been successfully used. One is a simple RC coupled two stage amplifier using 6AK5 pentodes. The input pentode was selected for low grid current and battery operated with low plate and screen voltages of about 20 v. The rise time of this preamplifier was 0.5 μsec for a step function input.

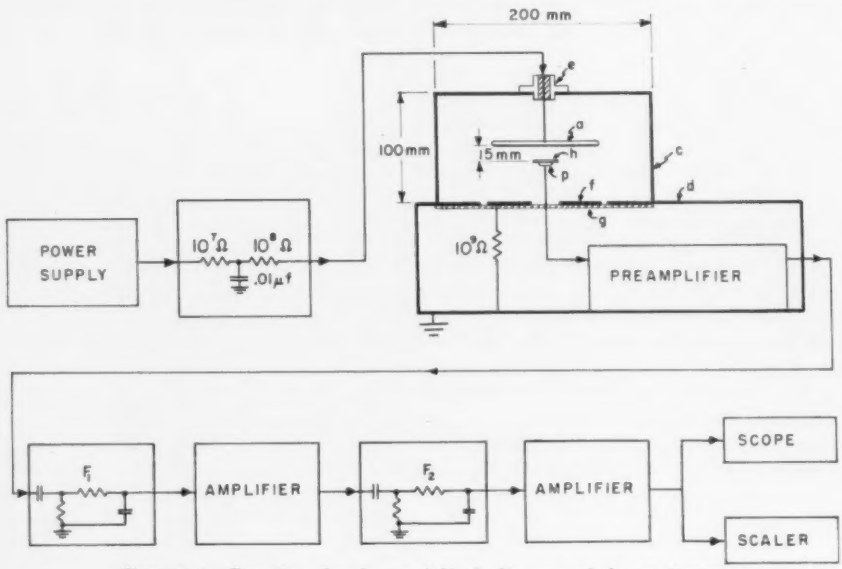

FIGURE 1. *Counting chamber and block diagram of the equipment.*

Wide-band amplifiers are used so that the pulse shaping is exclusively done by the filters F_1 and F_2.

For lower noise level a cascode input type preamplifier [8] similar to that described by C. Cottini et al. [9], was used with the pulse electrode connected to the floating input grid. While changing the chamber voltage this grid is shunted by a 100 μf condenser to prevent excessive charging of the floating grid.

The output pulse shape was controlled by the use of two filters, F_1 and F_2 in figure 1. Each filter contained a high and low pass RC network with equal time constants. The amplifiers were designed to have bandwidths in excess of a megacycle. Since this is much greater than the bandpass of the filters, the amplifiers have negligible effect on the output pulse shape. In each filter one of three different time constants, of 1, 2, and 4 μsec, could be selected by switches.

When both filters have been inserted in the amplifier chain and the time constant of 1 μsec was used, the rms noise as related to the input was $\sim$6 μv for the pentode-preamplifier, and $\sim$3 μv for the cascode type preamplifier.

4. Results and Discussion

For networks of time constants of the order of a microsecond, the pulse profile after the appearance of an alpha track in the chamber can be considered to be composed of a step pulse caused by electrons before attachment, followed by a long rise (linear in the first approximation) due to ionic motion. The presence of both components in the alpha pulse profile is clearly shown by figures 2a, b, and c, photographs of the output pulses on an oscilloscope when only one filter, F_1 with RC=1, 2, and 4 μsec respectively, and the cascode preamplifier is used. The fast rising and decaying part of the output pulses is due to the short electronic motion while the approximately constant tail is caused by the long uniform motion of the ions. For comparison output pulses were photographed in figures 2d, e, and f with the same settings of the equipment but introducing pulser step pulses which, instead of having been followed by a slow linear rise like the alpha pulses, decayed in 350 μsec. The negative slope of this decaying part of the pulser pulses is negligibly small as compared to the positive slope of the alpha pulses resulting from the motion of the full ionic charge through the entire chamber separation. It is seen from figures 2d, e, and f that while these output pulses successfully simulate the electronic components of the alpha pulses, the constant tails are missing.

The triggering level is chosen such that the scope is triggered with about equal frequency ($\sim$60/sec) on the alpha pulses and on noise. The noise observed when using the pulser (figures 2d, e, and f) is smaller than that obtained for alpha pulse operation (figures 2a, b, and c). This is readily explained by the low output impedance of the pulser (100 ohm) coupled to the preamplifier grid as compared to the high impedance when the grid is floating. The time scale is 5 μsec per division and the amplifier gain is the same ($\sim 10^6$) in all pictures of figure 2.

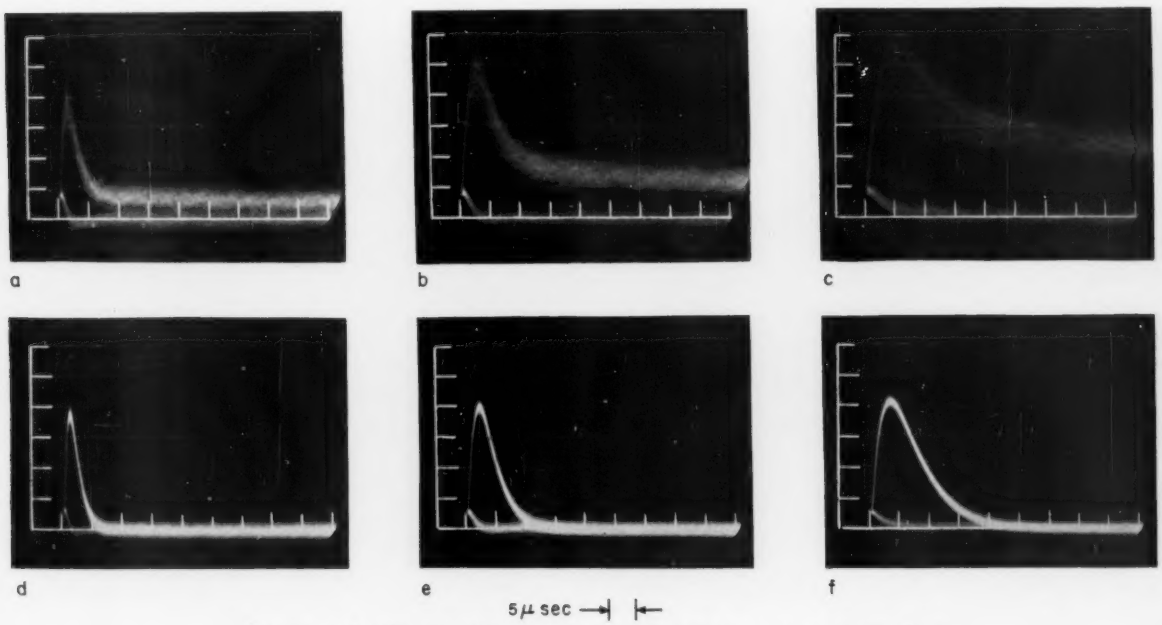

FIGURE 2. *Oscilloscope photographs of the output pulses using one filter F_1.*

Pictures a, b, and c are of alpha pulses with filter time constants of 1, 2 and 4 μsec respectively. The first short pulse is caused by the fast motion of electrons before attachment, the long tail (the height of which increases with increasing filter time constant) is the contribution of the slow ionic motion. For calibration pictures d, e and f, corresponding to a, b and c, are taken with 87 μvolt step pulses from a pulser. The overall amplifier gain is the same ($\sim 10^6$) in all pictures and the time scale is 5 μsec/division.

The output voltage, $V_1(t)$, after the filter F_1, is

$$V_1(t)=a\frac{t}{RC}e^{-\frac{t}{RC}}+\alpha\left[RC-(RC+t)e^{-\frac{t}{RC}}\right] \quad (2)$$

where a is the amplitude of the step input appearing at $t=0$, and α is the constant slope of the linear rise beginning at $t=0$. While the first term reaches (at $t=RC$) a maximum of ae^{-1}, which is thus independent of RC, the second term approaches the value α RC (proportional to the ionic charge collected within one RC) and depends on RC. This proportionality of the amplitude of the tail with increasing RC is clearly shown in figures 2a, b, and c. The amplitude of the electronic component appears to be independent of RC, thus proving that the duration of the free electronic motion, before attachment is shorter than the smallest applied RC=1 μsec. After subtracting the ionic contribution of the output pulse and using the calibration step pulses of the pulser in figures 2d, e, and f (each taken with 87 μv amplitude), the electronic input pulse from the alpha tracks was calculated to be ~80 μv. This value agrees with the estimate given above. It should be recalled that the estimate was rather uncertain due to the lack of precise knowledge of the attachment coefficient in atmospheric air. Also, the field in the chamber is not uniform and the alpha energy spent in the chamber is dependent on the angle of emission.

It is interesting to note that by the use of a proper chamber geometry, uniform field and uniform alpha energy, the techniques presented here could be used for an experimental determination of the electron attachment coefficient at pressures higher than usually permitted in other methods of measurement.

For alpha particle counting with the shortest resolving times the introduction of another filter F_2 appears useful. The output voltage after F_2 is

$$V_2(t)=a1/2\left(1-\frac{t}{3RC}\right)e^{-\frac{t}{RC}}+\alpha\frac{1}{3!}\frac{t^3}{(RC)^2}e^{-\frac{t}{RC}} \quad (3)$$

There are two advantages of the use of $V_2(t)$ as compared to $V_1(t)$.

The second term in $V_2(t)$ is diminished in amplitude (a maximum of $\frac{9}{2}e^{-3}\alpha$ RC ~0.23 α RC appears at $t=3$ RC) and cut short in time as compared with the long tail in $V_1(t)$.

The great advantage for a counting experiment is provided by the first term in $V_2(t)$ which passes through zero at $t=3$RC, giving thereby an output pulse duration (approximate resolving time of counting at low discrimination levels) independent of the spread in amplitude a of the alpha pulses. These pulses have a maximum of

$$a\frac{(3-\sqrt{3})^2}{2}\left(1-\frac{3-\sqrt{3}}{3}\right)e^{-(3-\sqrt{3})}\sim 0.13a$$

at $t=(3-\sqrt{3})$RC ~1.27 RC, a minimum (undershoot) of ~40 percent of the maximum at $t=(3+\sqrt{3})$RC ~4.7 RC.

Figures 3 a, b, and c demonstrate these expected pulse shapes for the alpha pulses taken with the use

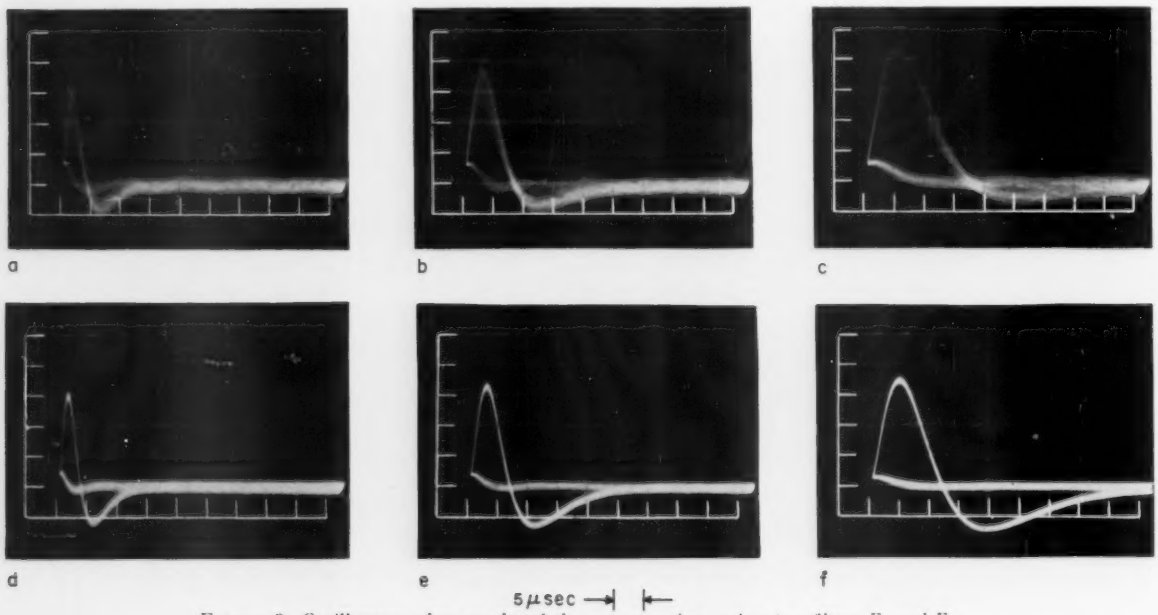

FIGURE 3. *Oscilloscope photographs of the output pulses using two filters F_1 and F_2.*

Pictures a, b, and c are of alpha pulses with filter time constants of 1, 2, and 4 μsec respectively. For calibration pictures d, e, and f, corresponding to a, b, and c, are taken with 100 μvolt step pulses from a pulser. Comparison with figure 2 shows that the use of the second filter F_2 nearly eliminates the contribution of the slow ionic motion from the alpha pulses and results in short pulse periods (resolving times) independent of the amplitudes. The overall gain is the same (~10^6) in all pictures and the time scale is 5 μsec/division.

of the two filters F_1 and F_2 with time constants 1, 2, and 4 μsec respectively. Figures 3 d, e, and f are taken with calibration step pulses of 100 μv amplitude from the pulser. The amplifier gain is the same ($\sim 10^6$) in all pictures of figure 3.

At RC = 1 μsec (figs. 3 a and d) the alpha pulse and the calibration pulse are similar and both of ~3 μsec duration since the contribution of the slow ion pulse is small at this time constant. As the time constant increases (figs. 3 b and c), the contribution of the ion pulse becomes larger. This results in a compensation in part of the undershoot of the electronic pulse and also in a delay of the zero crossing (the pulse duration is larger than 3 RC). The time scale is 5 μsec per division. Due to the nonuniformity of the chamber geometry for the different alpha tracks at different angles within a 2 π solid angle, the alpha amplitudes display a spread of ~30 percent. This is not disturbing in counting experiments. As seen in figure 3, there is a definite and sufficient gap between the noise and the smallest alpha amplitudes even with the dead time of ~3 μsec.

Comparison of our counting results with those of the Radioactivity Section of the National Bureau of Standards (using a methane flow 2 π—proportional counter) showed agreement to better than 0.1 percent indicating that our counting efficiency is very nearly 100 percent.

5. References

[1] A. B. Gillespie, Signal, noise, and resolution in nuclear counter applications (Pergamon Press, London, 1953).
[2] D. H. Wilkinson, Ionization chambers and counters, p. 66 (University Press, Cambridge, 1950).
[3] D. H. Wilkinson, ibid ref. 2, pp. 31–42.
[4] L. B. Loeb, Basic processes of gaseous electronics, p. 381 (University of California Press, Berkeley, Calif., 1955).
[5] L. B. Loeb, ibid ref. 4, p. 402.
[6] N. E. Bradbury, Phys. Rev. **44**, 883 (1933).
[7] G. S. Hurst and T. E. Bortner, Phys. Rev. **114**, 116 (1959).
[8] Oak Ridge National Laboratory Drawing Q–2069A–2 (E. Fairstein).
[9] C. Cottini, E. Gatti, G. Giannelli, and G. Rozzi, Il Nuovo Cimento **3**, 473 (1956).
[10] Z. Bay, P. A. Newman, and H. H. Seliger, Rad. Research (to be published).
[11] Z. Bay, F. D. McLernon, P. A. Newman, Bull. Am. Phys. Soc.; II 5, 355, K10, (1960).

(Paper 65C1–54)

JOURNAL OF RESEARCH of the National Bureau of Standards—C. Engineering and Instrumentation
Vol. 65, No. 1, January–March 1961

X-Ray Diffraction Measurement of Intragranular Misorientation in Alpha Brass Subjected to Reversed Plastic Strain

C. J. Newton and H. C. Vacher

(July 26, 1960)

A monochromatic misorientation goniometer was built and used to examine the character of X-ray diffraction spots from 70 percent copper, 30 percent zinc alpha (cartridge) brass specimens subjected to unidirectional and reversed plastic deformation. A two-exposure, moving and stationary film technique was employed. Numerical measurements of the average subgranular misorientation, amounting to several hundredths of a degree, were obtained at different stages in one complete cycle of 1 percent plastic strain amplitude. About 60 percent of the misorientation was recovered when the plastic strain was reversed, leaving a residual misorientation at zero net strain that increased linearly with the cumulative strain.

1. Introduction

Since an X-ray diffraction technique can provide information relating to the structure of metals on the atomic lattice scale, there is a continuing search for applications of this kind of tool in the study of structure-sensitive properties. The usefulness of the techniques has often been lost because of the difficulty of separating the numerous factors that can affect the diffraction of X-rays from crystals. The purpose of the investigation described in this paper was to devise a relatively simple method for measuring a single one of these factors—misorientation—and observe how it varied during reversed plastic deformation of a ductile polycrystalline metal. By misorientation in a grain, or disorientation as it is sometimes called, is meant the angle through which the atomic lattice planes are elastically or plastically bent or fragmented.

The distortion in Laue patterns of X-ray diffraction spots, commonly called "asterism," from single crystals subjected to shear strain has long been observed [1][1]. Such spot blurring is a qualitative indication of lattice distortion. In 1925, J. Czochralski [2] reported that the asterism in a Laue pattern of a twisted aluminum crystal was decreased when the specimen was twisted backwards. Similar qualitative experiments were made in the present study. Both transmission and back-reflection Laue patterns were made from a single grain in a very large-grained aluminum specimen that was subject to forward and reversed bending. The set of transmission Laue patterns may be seen in figure 1. The greatest recovery of sharpness of the spots came not at the recovered zero bending position but at the negative bending position past zero; this interesting behavior remains to be explained. In recent years a more sophisticated Laue pattern technique, the focused spot method, has been employed by C. A. Julien and B. D. Cullity [3] to show the partial recovery of Laue spots after reversed twist or bending in aluminum crystals.

For studies of polycrystalline metals, much work has been done with the phenomenon of the broadening of characteristic X-radiation diffraction rings or lines in Debye-Scherrer patterns [4]. If the material is not so fine-grained as to give continuous lines in the pattern, a large number of discrete spots may be observed in the line position. Each spot is a diffraction from a known set of atomic lattice planes in an individual crystallite, and the blurring of such spots in cold-worked polycrystalline metals may yield information of interest. A study reported in 1940 by W. A. Wood and P. L. Thorpe [5] on the behavior of the crystalline structure of brass under slow and rapid cyclic stresses showed no recovery of tangential spot blurring on the Debye-Scherrer diffraction rings upon reversal of the static strains of the specimens. In 1953, however, W. A. Wood and R. B. Davies [6] showed that if the strains were small enough, about 1 percent in copper, there was a partial recovery in the spot blurring when the strain was reversed. In the present study, similar behavior was observed in the diffraction patterns from aluminum, copper, and steel rods subjected to torsional straining. The set of patterns from the copper rods at various stages in one cycle of strain may be seen in figure 2.

In 1951, A. J. Reiss, J. J. Slade, and S. Weissmann [7] described a method for studying the breadth of the reflecting range of individual crystallites in a polycrystalline specimen. Using a specimen with grains coarse enough that a spotty Debye-Scherrer pattern was obtained, they recorded the stationary

[1] Figures in brackets indicate the literature references at the end of this paper.

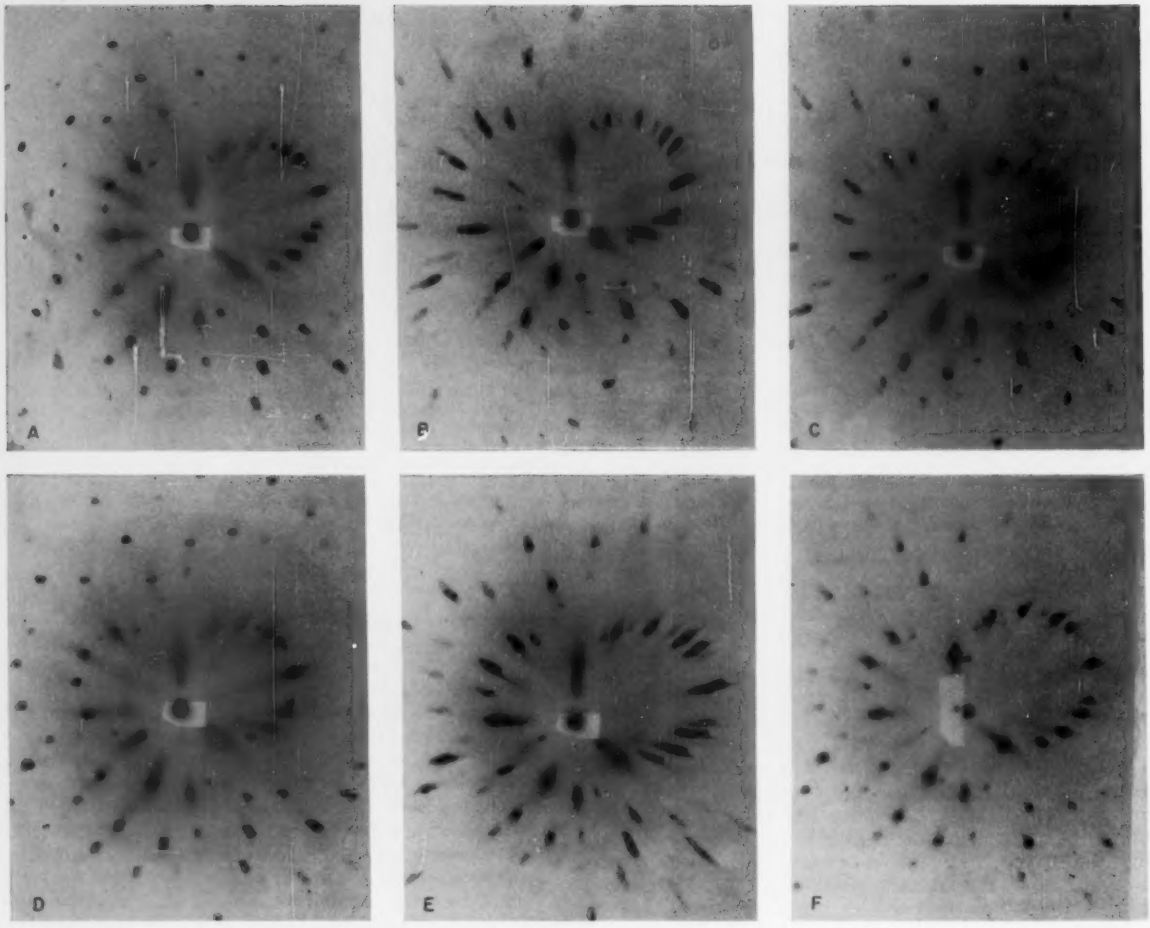

FIGURE 1. *Set of transmission Laue patterns of large aluminum grain in specimen bent through 1¼ cycles of plastic deformation.*
A. Annealed (zero position); B. positive bending; C. zero position; D. negative bending; E. zero position; F. positive bending.

pattern several times on the same film; between exposures small discrete changes were made in the angular setting both of the specimen and of the film. Since that paper was published, S. Weissmann and his coworkers have continued to refine the rather complex instrumentation and technique to contribute many studies based upon it [8], which were not concerned directly, however, with the effects of reversed plastic strain.

C. S. Barrett [9] has described a scheme for rotating a film and off-center specimen together, "permitting the spread of a Laue spot in all directions without altering the wavelength of the reflected beam." In 1954, E. Kappler and R. Mock [10] described a somewhat similar method for obtaining the range of reflection from a single crystal. Two diffraction patterns were called for in their procedures. First, the single crystal specimen was rotated and the diffraction pattern was recorded on a stationary film; and second, the diffraction pattern was recorded on a moving film, which rotates about the same axis as the crystal but at twice its angular velocity. The first pattern yielded data relevant to the range of lattice constant variation in the crystal; the second pattern related to the range of orientation.

In recent years there have been several studies related to the problem of fatigue of metals, in which essentially ordinary Debye-Scherrer X-ray patterns have been made of materials subjected to cyclic stresses. In 1957, a study was made by L. M. Clarebrough, M. E. Hargraves, G. W. West, and A. K. Head [11] on polycrystalline copper that had been reduced 25 percent by rolling and then fatigued to fracture. High-angle diffraction patterns were made during the course of fatigue. At first the patterns showed very diffuse lines; but, as the fatiguing process continued, the lines grew sharper until the α_1–α_2 doublet was clearly resolved. This phenomenon, sometimes called "work softening," has been reported by many workers, including T. Brown and R. K.

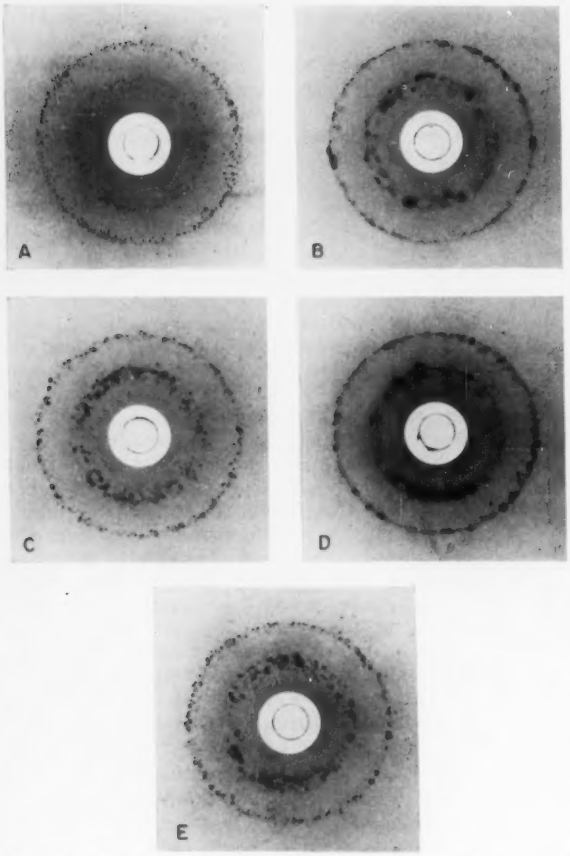

FIGURE 2. *High-angle X-ray diffraction patterns from copper rod at stages in one cycle of torsion.*

A. Annealed, zero twist; B. twisted clockwise 45°; C. twisted counter-clockwise to zero position; D. twisted counter-clockwise to −45°; E. twisted clockwise to zero position.

Ham [12], W. A. Wood and R. L. Segall [13], and M. L. Ebner and W. A. Backofen [14]. These studies are among those that emphasize the need for quantitative study of individual X-ray diffraction spots as affected by reversed plastic deformation.

Although the instrument and related procedure developed by Weissmann [8] and colleagues give the most complete information in this type of investigation, it was thought that a less complex method would suffice for the quantitative determination of misorientation. The interesting effects of reversed deformation do not appear to have been studied adequately in a quantitative manner, so the emphasis in this investigation was on measurements of misorientation at different stages of plastic straining, both forward and reversed.

2. Quantitative Measurement of Misorientation

In order to obtain a measure of the angle of misorientation, that is, the range of orientation in the distorted crystallite over which diffraction may occur, a special instrument, based upon the ideas of a double-crystal spectrometer, as may be seen in the diagram in figure 3, was designed and built. Although the procedure developed was for the measurement of the intragranular misorientation in coarse-grained polycrystalline specimens, it could be modified for work with single crystals. Shown in the photograph, figure 4, the instrument, which might be called a monochromatic X-ray misorientation goniometer, was built around three essential parts: (1) A manually adjustable mount for a stationary first crystal, *M*, ordinarily a strongly diffracting, monochromating single crystal; (2) a motor-driven oscillating mount for a second crystal, ordinarily the polycrystalline specimen, *S*, under study; and (3) a film holder circle with its center coincident with the axis of oscillation of the second crystal. The holder, *F*, might remain stationary or might oscillate synchronously with the specimen at the same angular velocity. Interchangeable film holders were provided, one for a semicylindrical strip film, the other for a small flat film. Most of the work was performed with the latter, using dental film because of its single-layer emulsion and resolving power higher than that of the usual X-ray film.

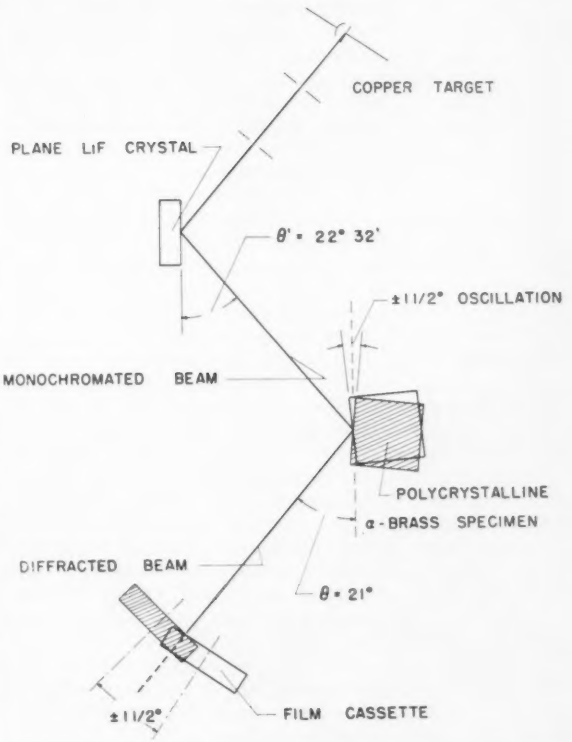

FIGURE 3. *Schematic diagram of the monochromatic misorientation goniometer.*

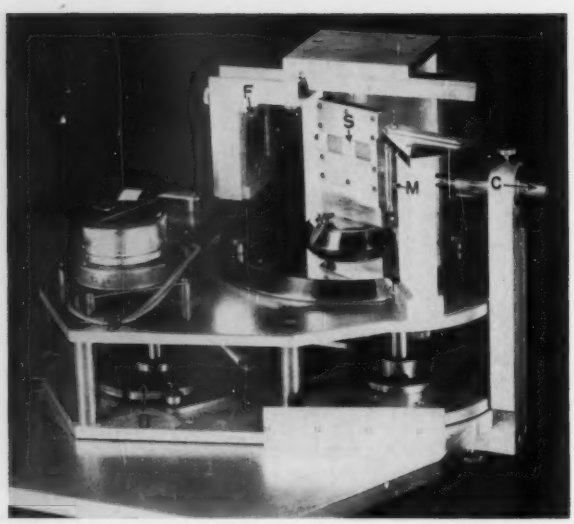

FIGURE 4. *Photograph of the monochromatic misorientation goniometer.*

M. Monochromating crystal; S. mounted brass specimen; F. flat-film holder; C. collimator; D. driving cam.

In this discussion, the term "broadening" of a diffraction spot means an increase of radial distance on the film over which blackening occurs; that is, it is an apparent increase in the range of Bragg angle over which diffraction takes place. Many factors contribute to the breadth of a spot in an X-ray diffraction pattern. Among the most important of these are (1) size of the diffracting crystallite, (2) lack of fine collimation, (3) lack of monochromatization, (4) randomly directed elastic strains of the lattice, and (5) micromisorientation. The first four factors, and possibly other instrumental factors, may all contribute in varying degrees to the broadening of spots whether the film is stationary or oscillating with the specimen. Only, however, in the latter case, that is, when the film is moving, does the fifth factor, misorientation, become important. By subtracting one-half the average breadth of many spots measured on a stationary film pattern from the average measured on a moving film pattern from the same specimen, a figure is obtained that represents the misorientation broadening. The average breadth on the stationary film must be divided by two because a linear distance on it corresponds to twice the angle of diffraction as compared to the same distance on the moving film.

In principle, the goniometer could also be used to determine the average microstrain, or range of atomic layer spacing, by comparing the stationary film spot breadths on the pattern from an annealed specimen with the pattern from the plastically deformed condition under study. It was observed, however, that this strain broadening was very small and probably within the limits of uncertainty in the measurements. It was not pursued in the present study.

Since the measurement of misorientation depended on the difference in broadening between stationary and moving film patterns, it was important to minimize the broadening due to the first four factors listed above; this consideration influenced many of the experimental details, including the choice of sample material. The metal used for the quantitative investigation was annealed alpha brass (70% Cu–30% Zn) with an average grain diameter of 0.035 mm. This grain size was sufficiently large so that it did not cause "small particle" broadening, but small enough so that the quantity it added to the "reflection breadth" (about 0.007 mm) was much less than the probable error of measurement of spot broadening. X-ray examination of the material indicated no preferred orientation.

The broadening due to lack of collimation and lack of monochromatization was minimized by using copper radiation and a lithium fluoride monochromating crystal. The Bragg angle for the strong (200) diffraction from this crystal is about 22½°, while the diffraction angle for the (111) ring from alpha brass is about 21°. Since these were the diffractions used in this study, the diffracting planes in the monochromator and specimen could be set nearly parallel to each other. This setting minimized dispersion [15] in the X-ray beam. The specimen was continuously oscillated about this position by a motor-driven, 3° cam mechanism. For comparable amounts of film density, exposure times for stationary film patterns were 6 hr and for moving film patterns, 10 hr, except for some few special cases of very diffuse patterns. Development of the films was carried out under as nearly constant conditions as practical. A typical pair of films, stationary and moving, is shown in figure 5.

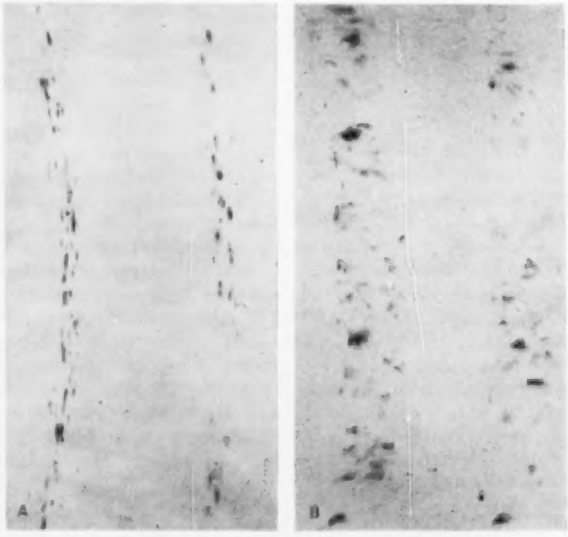

FIGURE 5. *A pair of patterns made with the monochromatic misorientation goniometer with* Cu K*α radiation showing the (111) and (200) diffractions from brass, which had been extended 1 percent.*

A. Stationary film; B. moving film.

The brass was received in 1 by ⅜ in. bars, from which specimens 7½ in. long, with a gage length of 1.250 in. and a reduced cross section measuring 0.625 by 0.373 in., were machined. These dimensions were chosen so that a single specimen could be both plastically extended and compressed, could carry resistance wire strain gages nearly an inch long, and could provide sufficient test volume to allow the preparation for X-ray studies of three sections, with surface normals making angles of 0, 45, and 90°, respectively, with the axis of the applied load. It was desired to make observations on different sections in order to ascertain any directional effects in the misorientation that might occur due to the angle of the surface with respect to the axis of plastic deformation or due to the sign of the deformation.

The plastic extension was performed using Templin grips; the plastic compression was made possible by the careful machining of the ends of the specimens and by the use of massive steel guides around the specimen undergoing compression. The routine of the mechanical testing and strain measurements, along with a discussion of the difficulties that sometimes arise because of false negative permanent strains observed at small values of permanent set with resistance wire strain gages, has been previously reported [16].

The specimens from which the X-ray diffraction patterns were made were cut from the uniformly deformed gage length of the test specimens, with the normals to the surfaces to be polished each making a known angle, 0, 45, or 90°, with the axis of the applied load. The sections were mounted without heat in acrylic cement and carefully electropolished until, as verified by back-reflection X-ray diffraction patterns, all surface disturbance was removed.

On each diffraction film, 25 spots were measured. These were selected at random except that none was more than 12° from the equatorial region so that any azimuthal correction could be neglected and none was so near the edge of the diffraction band as to be obviously incomplete. Their breadths were measured parallel to the equatorial plane of diffraction on each pattern with a traveling microscope of about four-power magnification, reading directly to the nearest 0.01 mm. This type of diffuse spot measurement requires considerable practice, and allowance must be made for subjective factors, such as judgment of the edge of a spot, when data taken by different observers are to be compared.

From the difference between the average of spot breadths on the moving film and one-half the average on the stationary film, one obtained the contribution to the broadening from the misorientation present within grains in the polished surfaces of X-ray specimens sectioned at each of the three angles specified above from the deformed test specimens. This misorientation is given in the data table. It is difficult to state a meaningful value for the reliability of these data; they were arrived at from readings of two observers and involve several averaging procedures. A reasonable value for their significance is an average uncertainty of about ±0.02°, except for one set of patterns made after an extension of the specimen of 2.2 percent. The spots on the stationary film patterns in this case were not significantly different from those observed on the other stationary films and were measured in the same manner. On the moving film patterns from this specimen, however, the spots were so diffuse that they could not be measured even after prolonged exposure. Only a visual estimate could be made of their average breadth, which was about 1.5°.

Results of intragranular misorientation measurements

State of plastic deformation			Average misorientation			
			45° Section	Cross section	Longitudinal section	Condition average
Annealed initial condition						6
Cycle position	Net strain	Cumulative strain				
Positive cycle	%	%	1/100 deg	1/100 deg	1/100 deg	1/100 deg
¼ (E)	+1	1	33	27	23	28
½ (E–C)	0	2	13	12	10	12
¾ (E–C–C)	−1	3	67	38	28	44
1 (E–C–C–E)	0	4	25	18	11	18
Negative cycle						
¼ (C)	−1	1	32	18	28	26
½ (C–E)	0	2	18	9	15	14
Large strain, unidirectional, 2.2 percent						150

Probable error in average about ±0.02°, except for case of 2.2 percent strain where it is about ±0.50°.
E—Extended 1 percent.
C—Compressed 1 percent.

The average misorientation is plotted in figure 6 as a function of the cumulative plastic strain for one cycle of 1 percent amplitude.

3. Discussion

The misorientation reported in the data table and on the graph is the average contribution to the breadth of the diffraction spots arising from the misorientation within the diffracting grains. The fact that a small amount was observed with the material in the initial condition indicates the sensitivity of the method, since the evidence of mechanical tests, metallography, and the sharpness of ordinary back-reflection X-ray patterns indicated that the brass was well annealed. This misorientation is actually the range of angle of the family of atomic planes in the metal grain from which diffraction takes place. Both plastic lattice bending and small-angle fragmentation may contribute to this spot-broadening factor; their effects are not separable by this technique.

The maximum average values of misorientation were observed in specimens cut so that their surfaces made an angle of 45° with the loading axis. The

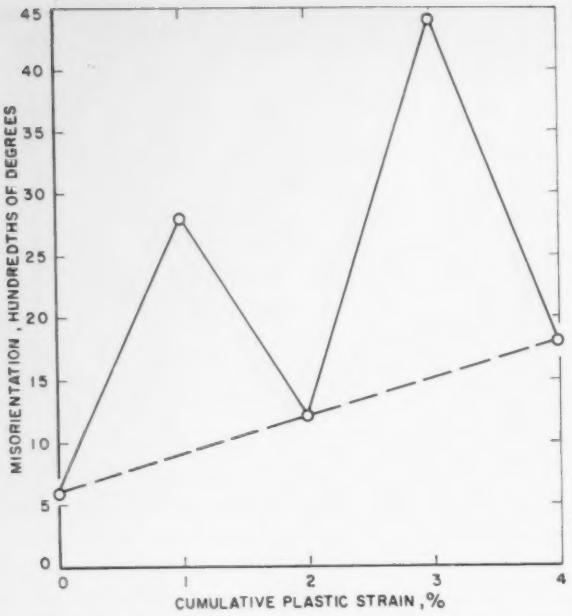

FIGURE 6. *Average misorientation versus cumulative strain for one cycle of plastic strain of 1 percent amplitude.*

directions of maximum shear stress were also at 45° to this axis. Because the angles of incidence and diffraction of the X-ray beam with respect to the polished surface were maintained equal, the diffraction planes (111) were parallel to this surface. The (111) plane is also the preferred plane of slip in this material. Hence, in the 45° section the observed diffraction spots came from crystals in which the angle between the slip plane and the maximum shear stress could be as small as zero. Since the smallest angle between (111) planes is 70°32′, in the diffracting crystals of the longitudinal and transverse sections the angle between the slip plane and the direction of maximum shear stress could not be smaller than about 25°; and it is significant that the misorientation observed in the latter cases was always smaller than that of the 45° specimens. These results emphasize the sensitivity of the method, and show that the lattice distortion of individual crystals in a polycrystalline matrix is related to their orientation.

The partial recovery of the misorientation with reversal of strain measured here in a quantitative manner is in agreement with those earlier qualitative observations on X-ray diffraction patterns cited in the introduction to this paper. These observations demonstrate that at least part of the lattice distortion is recoverable, and imply that, when the stress that has led to the generation and flow of dislocations in a crystal is reversed, at least part of the behavior of the dislocation system may also be reversed.

The average values of misorientation, 0.26° and 0.14°, observed in the two stages of the negative half cycle (i.e., begun with compression), as compared to the values 28 and 12 for the corresponding stages of the positive cycle, are symmetric, as expected in view of the shear nature of plastic deformation by slip in face-centered cubic metals. It was not felt necessary to carry the negative cycle any further under these circumstances.

The linear increase in the average residual misorientation at zero net strain is an interesting phenomenon. It indicates a permanent amount of disorder not recoverable by reversal of stresses on the dislocation system and is perhaps ascribable to the capture of dislocations at permanent pinning points due to plastic lattice bending carried so far that dislocations in other slip planes are generated. It would then be expected that the residual misorientation would be associated with the cumulative work-hardening of the metal, which Wood [17] found to increase nearly linearly with the first few cycles of reversed plastic deformation. Such a correlation is obscured by the reversible misorientation and by the Bauschinger effect, but it is hoped that further investigation will clarify the relationship.

The increase in misorientation when the unidirectional plastic strain was doubled was surprisingly large. It may reflect the increasing number of slip systems that must become active when individual crystals are forced to accommodate to the highly inhomogeneous strain in the polycrystalline aggregate.

4. Conclusions

The instrument and procedure described, while of only moderate complexity, permit quantitative measurements of intragranular misorientation in polycrystalline metals that are believed to be sufficiently precise for many purposes. Application of the technique to alpha brass specimens deformed in tension and compression showed that:

(1) Misorientation was highly sensitive to plastic deformation, the average value increasing from 0.06 to 0.28° when the annealed material was deformed plastically 1 percent.

(2) A large part of the misorientation was eliminated when the plastic strain was reversed.

(3) The residual misorientation increased linearly with increasing cumulative strain.

(4) The misorientation measured on surfaces parallel to directions of maximum shear stress was larger than that measured on surfaces either parallel or perpendicular to the loading axis.

The authors acknowledge the cooperation of colleagues at the National Bureau of Standards who made significant contributions to this investigation: in particular, A. N. Greaf, who built the goniometer, and H. E. Utech and P. D. Sarmiento, who assisted with the X-ray specimens and patterns.

5. References

[1] C. S. Barrett, Structure of metals, 2d ed., pp. 414–420 (McGraw-Hill Book Co., Inc., New York, N.Y., 1952).

[2] J. Czochralski, Mettallkunde und physicallische Forshung, Z. Metallkunde **17,** 1 (1925).

[3] C. A. Julien and B. D. Cullity, A study of deformed and recovered aluminum crystals by a new X-ray technique, Acta Metallurgica **1,** 588 (1953).

[4] B. D. Cullity, Elements of X-ray diffraction, pp. 263–69 (Addison-Wesley Publishing Co., Inc., Reading, Mass., 1956).

[5] W. A. Wood and P. L. Thorpe, Behavior of the crystalline structure of brass under slow and rapid cyclic stresses, Proc. Roy. Soc. London [**A**] **174,** 310 (1940).

[6] W. A. Wood and R. B. Davies, Effect of alternating strain on the structure of a metal, Proc. Roy. Soc. London [**A**] **220,** 255 (1953).

[7] A. J. Reiss, J. J. Slade, and S. Weissmann, A new X-ray diffraction method for studying imperfections of crystal structures in polycrystalline specimens, J. Appl. Phys. **22,** 665 (1951).

[8] S. Weissmann, Lattice inhomogeneities and substructures in crystalline materials, Engr. Research Bul. No. 39 (Rutgers Univ., New Brunswick, N.J., 1956).

[9] C. S. Barrett, loc. cit., p. 421.

[10] E. Kappler and R. Mock, An X-ray method of determining the distribution curve of the lattice constant and the distribution curve of the lattice misorientation on the same location on a single crystal specimen, Naturwissenschaften **41,** 330 (1954).

[11] L. M. Clarebrough, M. E. Hargreaves, G. W. West, and A. K. Head, The energy stored in fatigued metals, Proc. Roy. Soc. [**A**] **242,** 160 (1957).

[12] T. Broom and R. K. Ham, The hardening and softening of metals by cyclic stressing, Proc. Roy. Soc. [**A**] **242,** 166 (1957).

[13] W. A. Wood and R. L. Segall, Softening of cold worked metals by alternating strains, J. Inst. Metals **86,** 225 (1958).

[14] M. L. Ebener and W. A. Backofen, Hardening characteristics of polycrystalline copper under fatigue loading, Tech. Rept. No. 7 (Office of Naval Research, NR No. 031–356, May 1, 1958).

[15] R. W. James, The optical principles of the diffraction of X-rays, The crystalline state, vol. 2, pp. 306–14 L. Bragg, ed., G. Bell & Sons, Ltd., London, England, 1948).

[16] C. J. Newton, False negative permanent strains observed with resistance wire strain gages, ASTM Bul. No. 235, pp. 42–44 (1959).

[17] W. A. Wood, Some basic studies of fatigue in metals, Fracture (ch. 20), p. 412 (John Wiley and Sons, New York, N.Y., 1959).

(Paper 65C1–55)

JOURNAL OF RESEARCH of the National Bureau of Standards—C. Engineering and Instrumentation
Vol. 65C, No. 1, January–March 1961

Enthalpy and Specific Heat of Nine Corrosion-Resistant Alloys at High Temperatures [1]

Thomas B. Douglas and Andrew C. Victor

(September 1, 1960)

Specific heats from 0 to 900 °C that are believed to be accurate in general to within ±0.3 percent are reported for two alloys: 90 Ni–10 Cr and stainless steel, type 316. These values were calculated from enthalpies measured with a drop method and a precision Bunsen ice calorimeter. For reference and comparison, high temperature specific heats of seven other base-metal alloys, determined similarly at the Bureau and previously published, also are tabulated. These seven alloys are 80 Ni–20 Cr, 76 Ni–15Cr–9 Fe (three slightly different samples), stainless steel, types 347 and 446, and Monel (67% Ni, 30% Cu).

1. Introduction

Certain base-metal alloys which are relatively resistant to corrosion find practical applications at elevated temperatures, where a knowledge of their specific heats and other physical properties is often needed. For many of these, specific heats only at or near room temperature have been reported. During the past few years the specific heats of nine such alloys have been measured accurately (from 0 to 900 °C in all but one case) at the National Bureau of Standards. The values for seven of these alloys and complete details have been published previously [1, 2][2], but for ready reference and comparison are tabulated here alongside the newly reported values for the other two alloys. Several of these alloys are so similar in chemical composition that the comparison of their specific heats may afford some assistance when it is desirable to estimate values for analogous compositions. It should be pointed out, however, that the specific heats of many alloys depend appreciably on their previous histories, and in many cases small changes in composition introduce into the specific-heat—temperature curve large anomalies attributable to the appearance of phase changes.

2. Alloys Recently Measured

Enthalpy measurements were made on three samples (A, B, C) of the alloy 90 Ni–10 Cr (commercially designated as Chromel P) and on one sample of stainless steel type 316 (Am. Iron & Steel Inst. designation). Table 1 gives the compositions of these alloys as determined by their analyses at the Bureau,[3] and also affords a comparison with the ranges of composition associated with the nominal designations "Ch P" [3] and "SS 316" [4]. No attempt was made to correct the measured enthalpies to the basis of a different composition.

The enthalpy measurements on 90 Ni–10 Cr were made on rolled strips. As indicated in section 4, a few of these measurements were on specimens that had been previously annealed by heating to approximately 1,100 °C for about 5 minutes [5].

[1] The measurements on 90 Ni-10 Cr were supported by the Diamond Ordnance Fuze Laboratory, Department of the Army, Washington, D.C. Those on stainless steel type 316 were supported by the Wright Air Development Center, Department of the Air Force, Wright-Patterson Air Force Base, Ohio.

[2] Figures in brackets indicate the literature references at the end of this paper.

[3] The samples of 90 Ni-10 Cr were analyzed by chemical methods. The analysis of the stainless steel type 316 was determined spectrochemically, and is to be considered approximate only, since suitable spectrochemical standard samples were not available. However, the enthalpy and specific heat of the latter alloy are insensitive to errors in composition, since the heat capacities per unit mass of the three principal elements (iron, chromium, and nickel) are approximately the same.

TABLE 1. *Chemical compositions of the alloys thermally measured and of the corresponding nominal alloys*

Alloy designation	Sample	Chemical composition (weight percent)											
		Ni	Cr	Fe	Si	Zr	Co	Cu	Mn	Nb	Mo	C	Total
Ch P	Measured (A)	89. 1	9. 6	0. 63	0. 42	0. 12	0. 08	0. 01	0. 01	------	------	------	100. 0
	----do----(B)	89. 3	9. 3	. 34	. 44	. 11	. 03	. 01	. 02	0. 26	------	------	99. 8
	----do----(C)	89. 4	9. 3	. 35	. 46	. 11	. 03	. 01	. 02	. 26	------	------	99. 9
	Nominal	90	10	------	------	------	------	------	------	------	------	------	100
SS 316	Measured	12. 6	17. 0	[a]	. 4	[a]	[a]	[a]	1. 4	[a]	2. 0	[a]	------
	Nominal	10–14	16–18	------	[b] 1. 0	------	------	------	[b] 2. 0	------	2–3	[b] 1. 0	------

[a] Not determined.
[b] Maximum.

All the enthalpy measurements on stainless steel type 316 were made on the sample (sawed from a large ingot) in the condition in which it was received, without further heat or mechanical treatment. The thermal history of the sample is unknown, but supposedly it had been annealed by heating in a salt bath and quenching, which is the standard procedure for austenitic stainless steels [4].

3. Calorimetric Procedure

The apparatus and method used in measuring the enthalpy were described in detail in a recent paper [6]. Briefly, the sample in a helium-filled container of the alloy 80 Ni-20 Cr was held inside a silver-core furnace in an atmosphere of helium until, as determined by preliminary "relaxation-time" tests, the sample had time to reach the furnace temperature within 0.01 deg C. The sample and container were then dropped into a precision Bunsen ice calorimeter, the heat they delivered in cooling to 0 °C being determined by the mass of mercury entering the calorimeter because of the reduction in volume caused by the melting of ice. Similar measurements were made on the empty container to account accurately for (a) the part of the heat due to the container when a sample was present, and (b) the heat lost outside the calorimeter during the drop.

The furnace temperature, which was held constant to ±0.01 deg C during a heat measurement, was measured up to 600 °C by a strain-free platinum resistance thermometer and above 600 °C by a platinum—platinum-10-percent rhodium thermocouple. Both instruments were actually read up to 600 °C in order to be able to detect any unusual departure of either from its calibration. The thermocouple had been calibrated on the International Temperature Scale of 1948. The calibration factor of the ice calorimeter was taken to be 64.646 defined thermochemical calories [4] per gram of mercury, which is based on hundreds of electrical determinations made earlier at the Bureau [6].

4. Enthalpy and Specific Heat of 90 Ni-10 Cr

The mean observed values of enthalpy relative to 0 °C are shown for the four samples in columns 2 to 5 of table 2. For each case where more than one run was made on the sample at a given furnace temperature, the standard deviation of the mean is stated as a tolerance, and takes into account not only the precision of the runs with sample but also that of the runs on the empty container at the same temperature. (No runs were actually made on the empty container at 350 and 650 °C, but the enthalpy values used at these temperatures were obtained from smooth deviation plots of the runs at the other temperatures.) The few values in columns 3 to 5, which were run to compare several similar samples, differ by 0.15 percent or less from the values in column 2 (amounts within the accuracy of the measurements), and will not be further considered.

The values in table 2, column 2, show smoothly varying differences up to and including 600 °C, but in comparison an anomalous rate of increase with temperature between 600 and 700 °C. Three empirical equations were derived to fit the enthalpy in the respective temperature ranges 0 to 600°, 600 to 700°, and 700 to 900 °C, and their deviations from the mean observed values are given in the last column of table 2. The coefficients of the enthalpy equation for 0 to 600 °C were derived by the method of least squares; those for the equation from 700 to

[4] The "defined" thermochemical calorie (=4.1840 absolute joules) is the unit of heat used throughout this paper.

TABLE 2. *Relative enthalpy of 90 Ni-10 Cr*

Furnace temperature t	Mean observed enthalpy, $H_t - H_{0\,°C}$ [a]				Mean observed (col 2) minus smoothed enthalpy
	Sample A unannealed	Sample A annealed	Sample B unannealed	Sample C annealed	
°C	*cal g*$^{-1}$	*cal g*$^{-1}$	*cal g*$^{-1}$	*cal g*$^{-1}$	*cal g*$^{-1}$
100.00	10.75 ± 0.005	----------	----------	----------	0.00
200.00	22.08 ± 0.020	----------	----------	----------	−.01
300.00	33.91 ± 0.010	----------	----------	----------	−.01
350.00	40.01 ± 0.005	----------	----------	----------	+.01
400.00	46.20 ± 0.025	----------	----------	----------	+.01
500.00	58.87 ± 0.005	58.87 ± 0.005	58.82 ± 0.015	58.90 ± 0.065	.00
600.00	71.93 ± 0.010	----------	----------	----------	−.01
650.0	78.78 ± 0.030 [b]	----------	----------	----------	−.03
700.0	85.81 ± 0.020 [b,c]	85.86 [d]	85.68 ± 0.045	85.75 [d]	.00
800.0	99.84 ± 0.025	----------	----------	----------	.00
900.0	114.28 ± 0.010	----------	----------	----------	.00

[a] Each value represents the mean of two runs on the sample except where otherwise indicated.
[b] The mean of three runs on the sample at this temperature.
[c] A fourth run on the sample, discarded because of very inferior precision, is not included in the tabulated mean or its stated tolerance.
[d] Only one run was made on the sample at this temperature.

900 °C were obtained by direct substitution of the experimental points. The equation for 600 to 700 °C was then derived by requiring continuity of enthalpy and specific heat at 600 and 700 °C with the equations representing the other two temperature regions. The enthalpy and corresponding specific-heat equations (in terms of calories per gram and at t °C) are:

0 to 600 °C:

$$H_t - H_{0\,°C} = 0.11680t + 1.652\ (10^{-5})t^2 - 8.11\ \log_{10}[(t+273.15)/273.15] \quad (1)$$

$$C_p = 0.11680 + 3.304\ (10^{-5})t - 3.52/(t+273.15) \quad (2)$$

600° to 700 °C:

$$H_t - H_{0\,°C} = 182.977 - 0.74319t + 1.3310\ (10^{-3})t^2 - 6.680\ (10^{-7})t^3 \quad (3)$$

$$C_p = -0.74319 + 2.6620\ (10^{-3})t - 2.0040\ (10^{-6})t^2 \quad (4)$$

700 to 900 °C:

$$H_t - H_{0\,°C} = -0.92 + 0.10955t + 2.050\ (10^{-5})t^2 \quad (5)$$

$$C_p = 0.10955 + 4.100\ (10^{-5})t. \quad (6)$$

The specific heats represented by eqs (2), (4), and (6) are shown by the solid curve in figure 1, and the "observed" points were computed from successive differences in table 2, column 2, with application of corrections for curvature derived from eqs (2) and (4). Though it is obvious that there is a local maximum between 600 and 750 °C, the enthalpy was measured at too few temperatures to define accurately the course of the specific-heat curve in this temperature region; the particular curve formulated is, however, consistent with all the enthalpy data obtained. The Curie temperature of this alloy lies below the range of measurement [8]. However, similar "anomalous" increases in heat capacity in the temperature range 500 to 800° C have been observed in many nickel-rich alloys containing chromium [1,2,7]. The effect is paralleled by irregularities in other physical properties of the same alloys, and has been attributed by some authors to the disordering of a lattice of short-range order in the neighborhood of the composition Ni_3Cr [8].

The precision of the enthalpy measurements on 90 Ni-10 Cr and their deviations from the empirical equations used to represent them are indicated in table 2. Considering also the known sources of possible systematic and instrumental errors, the authors believe that eq (2) represents the true specific heat between 100 and 600 °C within ±0.3 percent. Between 600 and 700 °C the uncertainty is much greater, for the reasons indicated above. Above 700 °C the uncertainty should be comparable to that below 600 °C.

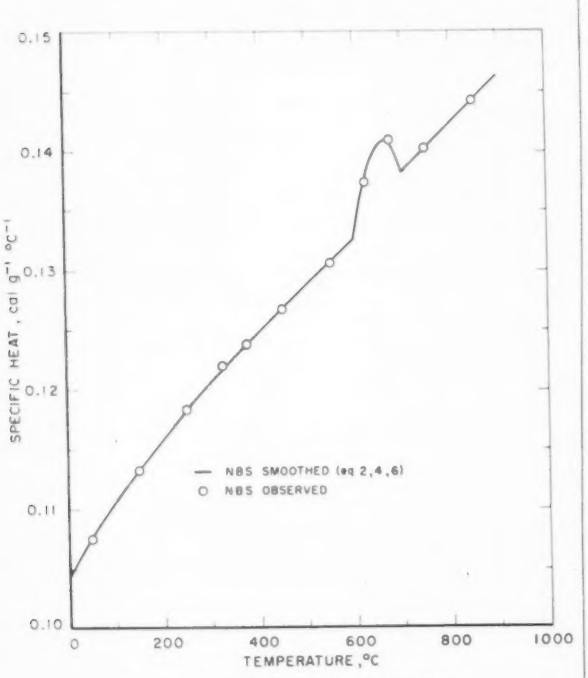

FIGURE 1. *Specific heat of 90Ni-10Cr.*

5. Enthalpy and Specific Heat of Stainless Steel Type 316

The mean observed values of enthalpy relative to 0 °C are given in the second column of table 3. Each stated tolerance represents the standard deviation of the mean, and reflects the contribution from the lack of perfect agreement for both the empty container and the container with sample. The "smoothed" enthalpy referred to in the last column of the table is that given by an empirical equation whose coefficients were derived from the values in the second column by the method of least squares.

TABLE 3. *Relative enthalpy of stainless steel type 316*

Furnace temperature t	Mean observed enthalpy, $H_t - H_{0\,°C}$ [a]	Mean observed minus smoothed enthalpy
°C	cal g⁻¹	cal g⁻¹
100.00	11.43 ± 0.015	+0.03
200.00	23.46 ± 0.010	−.01
300.00	36.10 ± 0.020	+.04
400.00	49.07 ± 0.015	−.03
500.00	62.51 ± 0.010	−.03
600.00	76.32 ± 0.015	−.06
700.0	90.62 ± 0.020	+.05
800.0	105.21 ± 0.045	+.08
900.0	119.96 ± 0.025	−.06

[a] Each value represents the mean of two runs.

This equation and the corresponding specific-heat equation (in terms of calories per gram and at t °C), applicable over the whole range 0 to 900 °C, are:

$$H_t - H_{0\,°C} = 0.12754t + 1.512\ (10^{-5})t^2 - 11.08 \log_{10}[(t+273.15)/273.15] \quad (7)$$

$$C_p = 0.12754 + 3.024\ (10^{-5})t - 4.81/(t+273.15). \quad (8)$$

Considering both random errors and known sources of possible systematic errors, the authors believe that eq (8) represents the true specific heat between 100 and 800 °C within ±0.3 percent.

The three curves of figure 2 represent the smoothed values of the specific heat of stainless steel type 316 as given by the present work, by Redmond and Lones [9], and by Lucks and Deem [10]. Compared with the authors' curve (labeled "NBS"), that of Redmond and Lones agrees within their stated uncertainty of ±5 percent, and that of Lucks and Deem agrees in general to better than ±1 percent.

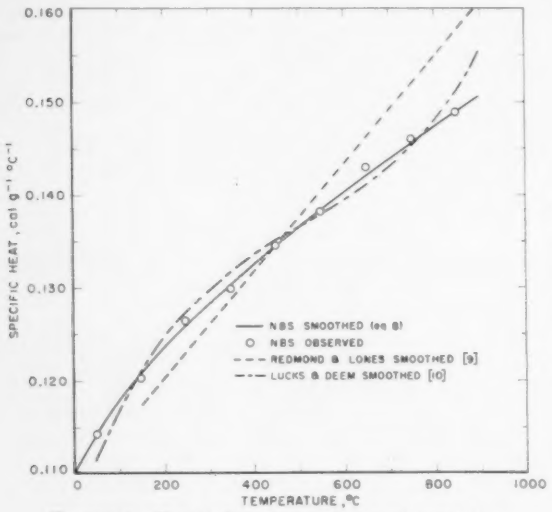

FIGURE 2. *Specific heat of stainless steel type 316.*

Because Lucks and Deem gave no unsmoothed values, estimates of accuracy, or sample analyses, there is no sound basis for making a truly objective comparison with the NBS curve. However, it seems likely that a major cause of the small differences may be their use of a positive-power series (of the form $C_p = A + Bt + Ct^2 + Dt^3$) to represent their smoothed values. As a general rule, if this form of equation does not indicate, in the temperature range of measurement, a radical change of slope for which there is no experimental evidence, it very often does so when extrapolated to higher temperatures. Knowing that extrapolation of empirical equations is widely indulged in by their users, and not without some practical justification, the present authors prefer forms of equation (such as eqs (6) and (8)) which give extrapolated curves similar in shape to the majority of known cases.

6. Compilation of the Specific Heats of Nine Alloys as Determined at the National Bureau of Standards

The purpose of this section is indicated in the introduction (section 1), where the original references to the seven alloys not discussed in this paper are cited. The chemical compositions as determined by chemical analysis are given in table 4, and the smoothed values of specific heat are given in table 5.

The authors thank several members of NBS who aided the present investigation: the samples of 90 Ni–10 Cr were chemically analyzed by R. K. Bell and E. E. Maczkowske, while the sample of stainless steel type 316 was furnished by L. L. Wyman and spectrochemically analyzed by R. E. Michaelis.

TABLE 4. *Chemical compositions of nine alloys (in % by weight)*

Element \ Alloy	Stainless steel			90Ni–10Cr	80 Ni–20 Cr	76Ni–15Cr–9Fe [b]			Monel
	316	347	446	Sample A		Sample 1	Sample 2	Sample 3	
	%	%	%	%	%	%	%	%	%
Fe	(a)	(a)	(a)	0.63	0.45	8.87	7.89	8.17	1.6
Ni	12.6	11.1	0.32	89.1	77.4	75.99	76.45	75.64	66.9
Cr	17.0	18.3	25.58	9.6	19.5	14.42	14.96	15.32	
Cu				0.01		0.22	0.15	0.19	29.8
Mn	1.4	1.30	0.42	.01	0.59	.28	.26	.33	1.0
Nb		0.86							
Si	0.4	.52	.68	.42	1.4	.17	.19	.21	0.07
C	(a)	.08	.23	(a)	0.04	.02	.07	.11	.15
S			.016			.007	.007	.007	
P			.019						
Zr				.12					
Mo	2.0								
Co				.08					
Total accounted for, %				100.0	99.4	99.98	99.98	99.98	99.5

[a] Not determined. [b] Alloys commercially produced as Inconel.

TABLE 5. *Specific heats of nine alloys (in cal g^{-1} deg C^{-1})*[a]

Temperature (°C) \ Alloy	Stainless steel			90Ni–10Cr	80Ni–20 Cr	76Ni–15Cr–9Fe[b]			Monel
	316	347	446	Sample A		Sample 1	Sample 2	Sample 3	
0	0. 110	0. 110	0. 108	0. 104	0. 103	0. 105	0. 104	0. 105	0. 101
25	. 1122	. 112	. 110	. 1058	. 105	. 1068	. 1061	. 1066	. 102
50	. 1142	. 114	. 113	. 1076	. 107	. 1084	. 1077	. 1082	. 103
100	. 1177	. 118	. 118	. 1107	. 111	. 1112	. 1108	. 1111	. 105
200	. 1234	. 123	. 129	. 1160	. 117	. 1160	. 1160	. 1162	. 110
300	. 1282	. 128	. 140	. 1206	. 122	. 1202	. 1207	. 1208	. 114
400	. 1325	. 133	. 151	. 1248	. 126	. 1240	. 1249	. 1251	----------
500	. 1364	. 137	. 163	. 1288	. 131	. 1276	. 1290	. 1292	----------
600	. 1402	. 141	. 21	. 1326	. 14	. 1379	. 1377	. 1396	----------
700	. 1438	. 145	. 170	. 138	. 147	. 1421	. 1422	. 1430	----------
800	. 1472	. 149	. 163	. 142	. 152	. 1462	. 1467	. 1465	----------
900	. 151	. 152	. 162	. 146	. 156	. 150	. 151	. 150	----------

[a] 1 cal = 4.1840 abs joules. See table 4 for chemical compositions of the alloys.
[b] Alloys commercially produced as Inconel.

7. References

[1] T. B. Douglas and J. L. Dever, J. Research NBS **54,** 15 (1955) RP2560.
[2] T. B. Douglas and A. W. Harman, J. Research NBS **60,** 563 (1958) RP2870.
[3] Mechanical Properties of Metals and Alloys, NBS Circ. 447 (U.S. Government Printing Office, Washington, D.C., 1943).
[4] Metals Handbook, Amer. Soc. Metals, pp. 554, 563, Cleveland, Ohio (1948).
[5] Metals Handbook, Amer. Soc. Metals, pp. 1031–1033, Cleveland, Ohio (1948).
[6] G. T. Furukawa, T. B. Douglas, R. E. McCoskey, and D. C. Ginnings, J. Research NBS **57,** 67 (1956) RP2694.
[7] H. Masumoto, M. Sugihara, and M. Takahashi, Nippon-Kinzoku-Gakkai-Shi (J. Japan Inst. Metals) **18,** 85 (1954); Chem. Abstr. **50,** 12625 (1956).
[8] M. Hansen, Constitution of Binary Alloys, 2d ed, pp. 541 to 546 (McGraw-Hill Book Co., Inc., New York, Toronto, and London), 1958.
[9] R. F. Redmond and J. Lones, U.S.A.E.C. Report ORNL–1342, 1952.
[10] C. F. Lucks and H. W. Deem, Thermal properties of thirteen metals, ASTM special technical publication No. 227, Amer. Soc. of Testing Materials, Philadelphia, Pa. (1958).

(Paper 65C1–56)

JOURNAL OF RESEARCH of the National Bureau of Standards—C. Engineering and Instrumentation
Vol. 65C, No. 1, January–March 1961

Determination of Minor Constituents in Low-Alloy Steels by X-Ray Spectroscopy

Robert E. Michaelis, Robert Alvarez, and Betty Ann Kilday

(September 13, 1960)

The analysis of low-alloy steel by X-ray spectroscopy has been investigated for the determination of minor constituents. In this study, detection limits and interferences were examined for the following 20 elements: Ag, As, Co, Cr, Cu, Ge, Mn, Mo, Nb, Ni, Pb, S, Se, Si, Sn, Ta, Ti, V, W, and Zr. For most of the elements, the detection limit is below 0.01 percent which is sufficient for control analyses. Interferences or interelement effects in low-alloy steel were found not to be serious, but may be encountered; for example, zirconium interferes with the determination of molybdenum. The application of the National Bureau of Standards standard samples to these determinations is discussed.

1. Introduction

A recent development in the field of spectrometric analysis is the application of the X-ray spectrum for making rapid and accurate determinations, particularly of major constituents in complex alloys such as those used in jet aircraft and rockets. The general techniques and applications of X-ray spectrometric analyses have been described in the literature [1, 2].[1] Although X-ray spectroscopy has been used for trace analyses, most of the reported work has been with solution or powder samples [3, 4]. Application of the X-ray method for determining a wide range of minor and trace constituents in steels by means of direct excitation of the metal has not been reported in the literature. The purposes of this investigation were twofold: First, to examine the sensitivity of detection and possible interferences in the determination of 20 elements in iron and steel; and second, to observe the applicability of NBS standard samples of low-alloy steels for calibration in this system.

2. Principles and Equipment

The analytical technique for X-ray emission analysis involves irradiating a sample by an X-ray beam of high energy, producing secondary X-rays having wavelengths characteristic of the elements in the sample. The radiation is dispersed according to wavelength by a suitable crystal and the X-ray intensity measured at selected wavelengths. Standard samples are used to relate this intensity to the concentration.

The instruments generally available are designated as flat- or curved-crystal spectrometers depending on the type of analyzing crystal employed. In flat-crystal spectrometers, collimators with parallel flat plates provide optimum intensity and resolution; in the curved crystal or focusing type, slits are used. In both types, the crystals are positioned according to Bragg's Law to obtain the wavelength of interest. Different crystals and radiation detectors with optimum characteristics may be used depending on the wavelength desired. Since the soft (longer wavelength) X-ray radiation of elements of low atomic number is easily absorbed by air, helium or hydrogen is substituted for air for the determination of elements below atomic number 22; recently vacuum spectrometers have been developed for the same purpose.

The detectors in common use include Geiger, proportional, and scintillation counters. Signal pulses from a detector may be counted by means of a scaler circuit, or the charge developed by the detector may be stored in a capacitor. An analytical curve can be established by relating the number of counts per unit time, or the integrated charge over a fixed time period, to the concentration.

A commercial multichannel X-ray unit of the curved crystal type served for this investigation. Incorporated in this unit is a series of crystal spectrometers, each with a detector and capacitor circuit. During the period of exposure of the sample, the intensities at each of 11 selected X-ray wavelengths can be integrated simultaneously. Instead of using the conventional millivolt chart recorder, a readout system especially designed for our laboratory is employed. In this arrangement, a digital voltmeter provides a measurement proportional to the voltage developed on each capacitor during exposure, and displays these numbers visually. At the same time, results can be typed and punched on tape by an electric typewriter. A four-digit number is obtained for each element by means of a sequential readout, and a feature of this equipment is that the response may be adjusted to be linearly related to concentration for most determinations.

The wavelength settings and other details of the X-ray equipment are given in table 1. The array indicated is designed primarily for the analysis of high-temperature alloys, although other applications

[1] Figures in brackets indicate the literature references at the end of this paper.

TABLE 1. *Details of the X-ray equipment*

Element	Wavelength	Crystal		Atmosphere	Detector	Slit	
		Radius	Material			Primary	Secondary
	A	*in.*				*in.*	*in.*
S	K_α 5.373	4	NaCl	He	Flow Geiger [a]	0.040	0.080
Mn	K_α 2.103	4	LiF	Air	Proportional [b]	.010	.005
Si	K_α 7.126	4	EDDT	He	Flow Geiger	.040	.020
Ni	K_α 1.659	11	LiF	Air	Proportional	.015	.030
Cr	K_α 2.292	11	LiF	do	do	.010	.050
V	K_α 2.505	4	LiF	do	do	.020	.010
Mo	K_α 0.711	11	LiF	do	do	.030	.015
Ti	K_α 2.750	4	LiF	do	do	.040	.020
Al	K_α 8.339	4	EDDT	He	Flow Geiger	.040	.020
Co	K_α 1.791	11	LiF	Air	Proportional	.040	.020
W	$L_{\alpha 1}$ 1.476	11	LiF	do	do	.010	.020
Nb	K_α 0.749	11	LiF	do	do	.030	.015
Scanner		11	LiF	do	do	.020	.030

[a] Minature tube with 2-cm window.
[b] Counter measures average current for integration.

such as to steel also were considered. All channels but one are fixed with respect to the individual wavelengths. The scanner, which may be set to measure any of the shorter wavelengths, provides additional flexibility for the determination of the elements of higher atomic numbers (atomic numbers 22 and above) not included in the fixed program.

As an external standard, a small copper sample is irradiated by the primary X-ray beam, and the undispersed secondary radiation measured by a Geiger detector operating in the proportional region. A preset value of integrated intensity for this channel terminates the exposure for all other channels.

Each spectrometer is set for the particular element by selecting the type of crystal and detector, choice of helium or air path, and settings of primary and secondary slit systems. These factors markedly influence the detectability, although other factors also are important such as the current and voltage of the X-ray tube, thickness and material of the tube window, path length, time of counting or integration, and the material irradiated.

The X-ray tube was supplied with an end window and a platinum target. Platinum was chosen since the determination of tungsten at low concentrations was required and this precluded the use of a tungsten target. Although studies were made to determine optimum power settings of the X-ray tube for the determination of some elements at low concentrations, it was found satisfactory to use one setting for all of the reported work—50 kv and 35 ma. Exposure times generally were either 1 min for the K series spectra of medium atomic number elements, or 4 min for the lighter elements and for the L series spectra of the heavier elements.

3. Standard and Reference Samples

The set of eight NBS Spectrometric Standard Samples of Ingot Iron and Low-Alloy Steel, NBS Nos. 1161 through 1168,[2] served for most of this investigation. Table 2 shows the values of the recently revised Provisional Certificate of Analyses for the eight standards. Other samples used in this investigation include the following: (a) Eight proposed NBS white cast-iron standard samples, (b) several of the older NBS spectrographic low-alloy steel samples which were originally ½ in. in diameter but were upset forged to a size suitable for X-ray spectroscopy (NBS Nos. 805a, 810a, 820a, and 821), (c) two solid sections of the NBS chemical standard samples (NBS Nos. 130a and 159), (d) seven reference samples of stainless steel containing a graded series for selenium, and (e) one reference sample of steel for silicon. A surface grinder was used for preparing all samples for analysis.

4. Results

4.1 Analytical Curves for Elements Commonly Determined

The analytical curve for manganese in iron and steel is shown in figure 1.[3] Each plotted point on this and subsequent curves generally represents the average of four individual determinations. With linear coordinates the plotted points closely fit a straight line. Log-log coordinates can be used to spread the analytical scale at the low concentrations when this is desirable. Note that the digital voltmeter response reads directly in terms of concentration; one digit response is equal to 0.001 percent of manganese. Similar straight-line curves are obtained with the standards for copper, nickel, chromium, and vanadium. If the concentration ranges are extended beyond those considered in this investigation, interferences may be observed. For example, chromium at higher concentrations will interfere in the determination of manganese [5].

[2] The standards are described in NBS Circ. 552, Standard Materials Issued by the National Bureau of Standards. This Circular may be obtained from the Superintendent of Documents, U.S. Government Printing Office, Washington 25, D.C., for 35 cents. Supplementary inserts are available from the National Bureau of Standards upon request.

[3] Sample designation is denoted on figures 1 through 8 by numbers or letters.

TABLE 2. *Provisional certificate of analysis*

(Revised—November 25, 1959)

Spectrographic ingot iron and low-alloy steel standards

NBS No.[a]	461 1161	462 1162	463 1163	464 1164	465 1165	466 1166	467 1167	468 1168
Designation	Low-alloy steel A	Low-alloy steel B	Low-alloy steel C	Low-alloy steel D	Ingot iron E	Ingot iron F	Low-alloy steel G	Low-alloy steel H
Element	%	%	%	%	%	%	%	%
C	0.15	0.40	0.19	0.54	0.037	0.065	0.11	0.26
Mn	.36	.94	1.15	1.32	.032	.11_3	.27_5	.47
P	.053	.045	0.031	0.017	.008	.012	.033	.023
S	(.02)[b]	(.02)	(.02)	(.02)	(.01)	(.01)	(.01)	(.02)
Si	.047	.28	.41	.48	.029	.025	.26	.075
Cu	.34	.20	.47	.094	.019	.033	.067	.26
Ni	1.73	.70	.39	.13_5	.026	.051	.088	1.03
Cr	0.13	.74	.26	.078	.004	.011	.036	0.54
V	.024	.058	.10	.29_5	.002	.007	.041	.17
Mo	.30	.080	.12	.029	.005	.011	.021	.20
Sn	.022	.066	.013	.043	.001	.005	.10	.009
Ti	(.01)	.037	.010	.004	.20	.057	.26	.011
B	.000_2	.000_5	.0012	.005	.000_1	(.000_2)	(.000_2)	.009
As	.028	.046	.10	.018	.010	.014	.14	.008
W	.012	.053	.10_5	.022	(.001)	(.006)	.20	.077
Zr	(<.005)	.063	.20	.010	(.002)	(<.005)	.094	(<.005)
Nb	.011	.096	.19_5	.037	(.001)	.005	.29	.006
Ta	.002	.036	.15	.069	.001	.002	.23	.005
Al	(.005)	.02_3	.02_7	.005	.19	.01_5	.16	.04_2
Co	.26	.11	.01_3	.02_8	.008	.04_6	.07_4	.16
Pb	(.003)	.006	.012	.020	(<.0005)	(.001_3)	.000_6	(<.0005)
Ag	(.001_5)	(<.0002)	(<.0002)	(.003_0)	(.0002_5)	(.0004_5)	(.004_0)	(<.0002)
Ge	(.001_5)	(.003_0)	(.002_5)	(.001_5)	(.003_5)	(.003_0)	(.003_0)	(.001_0)
O	(.02_0)	(.006)	(.007)	(.006)	(.003)	(.005)	(.004)	(.004)
N	(.00_6)	(.00_8)	(.00_6)	(.00_7)	(.00_5)	(.00_6)	(.00_4)	(.00_6)

[a] Sizes: 400 series, rods 7/32 in. in diameter and 4 in. long.
1100 series, disks 1¼ in. in diameter and ¾ in. thick.

[b] Values in parenthesis are *not* certified, but are given for information on the composition.

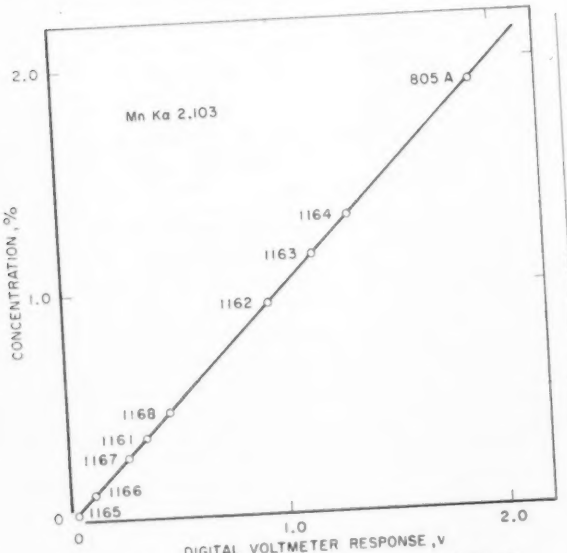

FIGURE 1. *Analytical curve for manganese in steel.*

The analytical curve for the molybdenum K_α line at 0.711 A is shown in figure 2; some of the points of this curve exhibit interference caused by the zirconium K_β line at 0.702 A. For interference of this

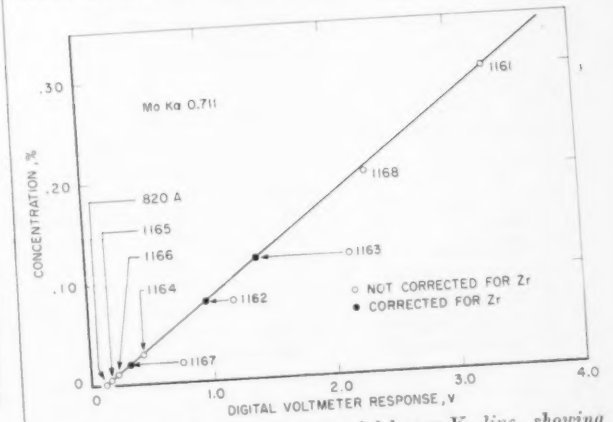

FIGURE 2. *Analytical curve for molybdenum K_α line, showing correction for interference by zirconium.*

type, a correction curve can be established by the use of standard samples to relate the apparent increase in molybdenum content to the zirconium content. The relationship is linear for the ranges of concentration usually covered. The corrected values, which are otained from a separate correction curve, are indicated by the black dots. To determine molybdenum with the most sensitive K_α line, either the zirconium content of the samples to be analyzed must be known to be below about 0.02 percent, or the zirconium content must be determined and a correction made. An alternative procedure is to choose a higher diffraction order of the same line to achieve separation from the interference line; however, this usually results in a severe loss in intensity. Another alternative is to use another line of the same series or another series; either choice results in a loss of intensity, the magnitude of which depends on the line chosen.

The analytical curve for the molybdenum K_β line, figure 3, clearly shows the absence of zirconium interference. In contrast to a 1-min integration time with the K_α line, a 4-min time is necessary with the K_β line for suitable detectability and for the precise determination of molybdenum at an alloy concentration of about 0.2 percent.

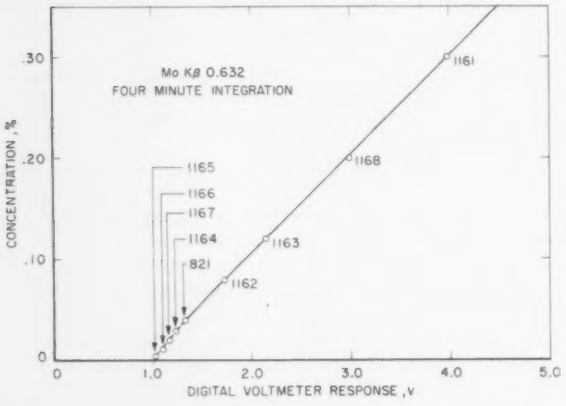

FIGURE 3. *Analytical curve for molybdenum K_β line, showing absence of interference by zirconium.*

Only preliminary results are available for the determination of silicon in low-alloy steel. Figure 4 shows the curve covering the range from about 0.1 to 0.8 percent of silicon and indicates the feasibility of the determinations. Even with 4-min integrations, however, rather poor detectability is observed and additional work on the determination of this element is necessary including possible changes in detector, crystal and slit width. Additional work on a set of proposed NBS white cast-iron spectrometric standards bas demonstrated the suitability of the X-ray method for the determination of silicon over the concentration range of 0.5 to 3.5 percent. In this investigation, it was observed that deviations from the analytical curve may occur as a result of

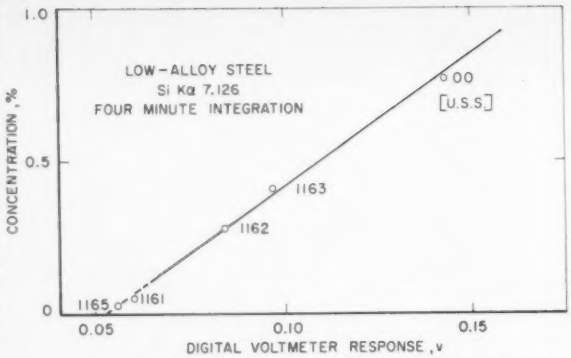

FIGURE 4. *Preliminary analytical curve for silicon in steel.*
Point 00 represents a reference sample from the United States Steel Corporation.

different casting conditions and surface preparations of samples and standards; these variables should be controlled carefully.

4.2. Analytical Curves for Elements Not Commonly Determined

The determination of boron in steel unfortunately cannot be done with the X-ray spectroscopic equipment now available; hence, optical emission has the advantage for this element. By contrast, selenium determinations cannot be made by conventional optical emission spectroscopy, but may be made readily by X-ray spectrometry. Since samples of low-alloy steel containing selenium were not available, analyzed samples of free-machining stainless steel of the 18-chromium—8 nickel type were used.[4] The results for selenium are shown in the analytical curve in figure 5.

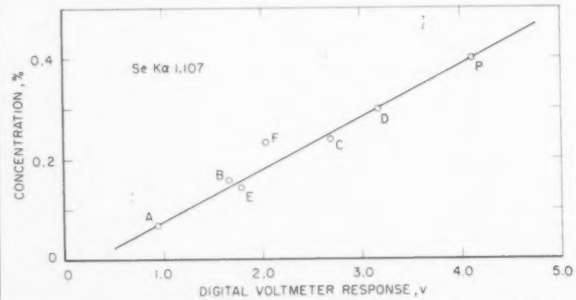

FIGURE 5. *Analytical curve for selenium in free-machining stainless steel.*

Arsenic also is difficult to determine in steel by conventional optical emission spectroscopy. The analytical curve obtained by X-ray spectroscopy is given in figure 6. A correction for amounts of lead above about 0.005 percent was found necessary, since the $L\alpha_1$ line of lead is coincident with the $K\alpha$ line of arsenic. The analytical points for arsenic, after making linear corrections for lead, are shown by black dots.

[4] The samples were provided by courtesy of the Baltimore Works of the Armco Steel Corp.

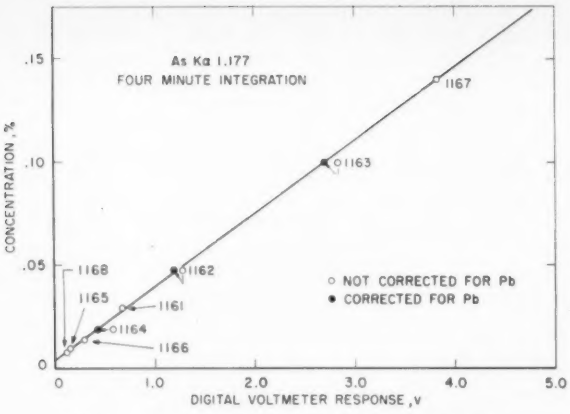

FIGURE 6. *Analytical curve for arsenic in steel.*

The analytical curve for zirconium is presented in figure 7. This curve is useful not only for determining zirconium but also for correcting results obtained when using the most sensitive molybdenum Kα line (see fig. 2), provided the relationship of the zirconium content to the apparent increase in molybdenum content is established. Linear analytical curves similar to that of zirconium are obtained with K radiation for titanium, cobalt, niobium, silver, and tin. Interferences are not observed. Because of the limitation in maximum voltage (60 kv) with this X-ray tube, L-series radiation must be used for the determination of some elements having large atomic numbers. The elements in this class include tantalum, tungsten, and lead. The intensities of the L spectra relative to the K spectra are low; this can generally be compensated by increasing the integration time from 1 to 4 min. Interferences are not detected for tantalum and tungsten. For lead, which exhibits interference from arsenic, the Lα_1 line can be used providing either the arsenic content is low, or a correction is made for the coincident Kα line of arsenic. As an alternative, the L$_\beta$ line for lead can be used with little loss in sensitivity.

The results of preliminary data for sulfur, which is present in eight proposed NBS white cast-iron standards, are presented in figure 8. A linear

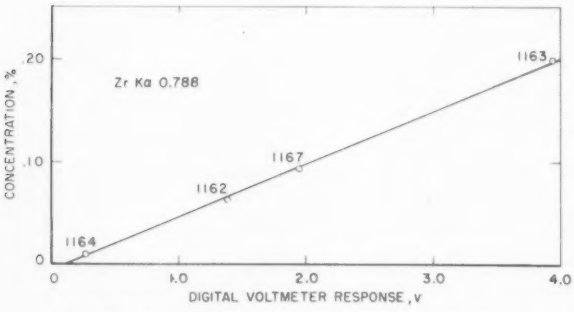

FIGURE 7. *Analytical curve for zirconium in steel.*

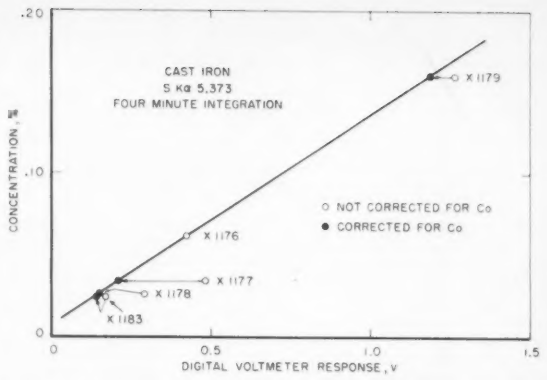

FIGURE 8. *Preliminary analytical curve for sulfur in cast-iron showing correction for interference by cobalt.*

correction for the cobalt content was found necessary because the cobalt Kα line at 1.791 A in the third order (5.373 A) interferes with the sulfur Kα line at 5.373 A. With the corrected data, a good fit of the analytical points to a straight line is observed for six of the eight standards. The other two show some deviation from the curve and are under further investigation. Similarly to silicon, a bias may be exhibited in the X-ray determination of sulfur because of different casting conditions and surface preparations of samples and standards.

4.3. Detectability

Results of the investigation for elements commonly determined in low-alloy steel are shown in table 3. Attention is called first to the detectability, which is defined here as that concentration at which the coefficient of variation is equal to 100 percent; and second, to the coefficient of variation at an alloy concentration for each element. With the possible exception of silicon, the data appear to be acceptable for control analyses of steel for these elements.

The results of the investigation for elements not commonly determined in steel is presented in table 4.

TABLE 3. *Results for elements commonly determined in low-alloy steel*

Element	Wavelength	Integration time	Detectability	Precision		
				Concentration	Coefficient of variation	Interference
	A	min	%	%		
Mn	Kα 2.103	1	0.003	1.00	0.3	None
Si	Kα 7.126	4	.05	0.30	16.3	Do.
Si [a]	Kα 7.126	4	----------	2.00	2.2	Do.
Cu	Kα 1.542	1	.005	0.25	2.0	Do.
Ni	Kα 1.659	1	.004	1.00	0.4	Do.
Cr	Kα 2.292	1	.005	1.00	.5	Do.
V	Kα 2.505	1	.007	0.25	2.7	Do.
Mo	Kα 0.711	1	.001	.25	0.4	Zr
Mo	K$_\beta$ 0.632	4	.002	.25	.8	None

[a] Cast iron.

TABLE 4. *Results for elements not commonly determined in low-alloy steel*

Element	Wavelength	Integration time	Detectability	Interference
	A	*min*	%	
S	K_α 5.373	4	0.002	Co
Ti	K_α 2.750	1	.015	None
Ti [a]	K_α 2.750	1	.007	Do.
Co	K_α 1.791	1	.002	Do.
Ge	K_α 1.256	4	.003?	?
As	K_α 1.177	4	.0007	Pb
Se	K_α 1.107	1	.006	None
Zr	K_α 0.788	1	.0006	Do.
Nb	K_α 0.749	1	.002	Do.
Ag	K_α 0.562	1	.0009	Do.
Sn	K_α 0.493	1	.004	Do.
Ta	L_{α_1} 1.522	4	.009	Do.
W	L_{α_1} 1.476	4	.003	Do.
Pb	L_{α_1} 1.175	4	.004	As
Pb	L_β 0.982	4	.005	None

[a] Geiger tube; the detectors for other elements are listed in table 1.

Acceptable detectabilities have been obtained for most of the elements. Specifically, the observed detectability for sulfur in the cast irons, 0.002 percent, indicates that this element can be determined successfully in most steels and cast irons. Note that for titanium, a two-fold improvement in detectability was realized by the substitution of a Geiger for a proportional counter. Although not normally required, considerable additional improvement for titanium (and vanadium as well) could be realized by employing helium or a vacuum rather than an air path. Samples containing more than about 0.003 percent of germanium were not available for further study of this element.

5. Discussion

It is of interest to compare the X-ray spectroscopic method of analysis for low-alloy steels to the conventional optical emission method with respect to detectability, precision, and speed. Although X-ray spectroscopy has gained widespread use primarily in the determinations of major and some minor constituents, the observed detectabilities for the minor and trace elements contained in low-alloy steels show that the method can be extended satisfactorily to this application. For the majority of elements, however, the optical emission method offers a marked advantage in detectability.

(Paper 65C1–57)

It is difficult to compare the precision of the two methods without specific reference to the element, concentration, exposure time, and sample. For most elements and with normal exposure times, optical emission will provide better precision below 0.1-percent concentration; the precision of the methods are about equal for concentrations of 0.1 to 1.0 percent, while the X-ray method is superior for concentrations above 1.0 percent. A statement as to the accuracy of the two methods would be similar to that for precision, except that X-ray spectroscopy may provide an advantage, at least for the heavier elements, in the analysis of samples having different metallurgical history. This results from the fact that the chemical combination of the elements has little or no effect on X-ray spectroscopy, but may have a marked effect on volatilization in optical emission analysis.

The exposure time required for optical emission analysis of a sample of low-alloy steel for the elements manganese, silicon, copper, nickel, chromium, and molybdenum is about 30 sec. With the exception of silicon, the same analysis by X-ray spectroscopy requires about 1 min (although this time may be reduced to 30 sec providing the concentration of each element is above 0.1 percent). To include the silicon determination by X-ray spectroscopy would require a minimum of 4 min (but at the same time sulfur also could be determined). The use of a vacuum instead of a helium path, improvements in crystals and detectors, and shorter path length may reduce considerably the time required for the silicon determination or for other determinations that now require long integration times. It may be noted that while boron cannot be determined with available X-ray spectroscopy equipment, selenium and sulfur cannot be determined with conventional optical emission instrumentation.

With respect to standard samples, the investigation has shown that the set of eight NBS Ingot Iron and Low-Alloy Steel Standards (Nos. 1161 to 1168) can be applied to develop suitable analytical curves for the X-ray determination of As, Co, Cr, Cu, Mn, Mo, Nb, Ni, S, Si, Sn, Ta, Ti, V, W, and Zr. For the determination of Ag, Ge, Pb, and Se, additional standard samples are required.

6. References

[1] L. S. Birks and E. J. Brooks, Anal. Chem. **30,** No. 10, 19A (1958).
[2] H. A. Liebhafsky, E. H. Winslow, and H. Pfeiffer, Anal. Chem. **32,** No. 5, 240R (1960).
[3] W. J. Campbell, M. Leon, and J. W. Thatcher, Bureau of Mines Report of Investigations 5497 (1959).
[4] P. D. Zemany, W. W. Welbon, and G. L. Gaines Jr., Anal. Chem. **30,** No. 2, 299 (1958).
[5] P. D. Zemany, Spectrochim. Acta. **16,** No. 6, 736 (1960).

JOURNAL OF RESEARCH of the National Bureau of Standards—C. Engineering and Instrumentation
Vol. 65C, No. 1, January–March 1961

Publications of the National Bureau of Standards*

Selected Abstracts

Measurement on the smoothness of paper, T. W. Lashof and M. Mandel, *Tappi* **43,** *No. 5, 385 (1960).*
The details of an interlaboratory study of the Bekk, Sheffield, and Bendtsen air-leak methods for the measurement of the smoothness of paper are presented. The data are analyzed using a procedure based on a linear model of the measuring process, and the results are interpreted in terms of this statistical model and the sensitivity concept. A comparison with previous work is also included. For the special series of mimeobond papers used in the study, good relationships were found between methods. Between-laboratory variability is appreciable in all three methods, but could be reduced with the aid of one or two standard samples. Both the Bendtsen and Sheffield methods suffer from scale-type errors due to the difficulty of bringing the several manostats of the Bendtsen or the several columns of the Sheffield into agreement with each other. When advantage is taken of their faster testing times to increase the number of specimens tested, the Bendtsen and Sheffield methods are slightly more sensitive to smoothness differences than the Bekk method.

Shielded coaxial leads for low temperature electrical measurements, N. L. Brown and R. N. Barfield, *Rev. Sci. Inst.* **31,** *No. 5, 517 (1960).*
The problem of making electrical contact to apparatus at very low temperatures is discussed, with particular reference to dielectric constant measurements in a situation where multiple shielding is required. Examples are given of easily constructed rigid electrode leads suitable for use at low temperatures, which have low thermal conduction, low and stable inter-conductor capacitance and conductance, and which provide for more than two coaxial conductors.

Compressive properties of hard tooth tissues and some restorative materials, J. W. Stanford, K. V. Weigel, G. C. Paffenbarger, and W. T. Sweeney, *J. Am. Dental Assoc.* **60,** *No. 6, 746 (1960).*
An improved method for preparing cylinders of enamel and dentin has been developed. The method entails the use of a jeweler's lathe and hydraulic handpiece. In addition to the hard tooth tissues, cylinders of silicate cement, zinc phosphate cement, amalgam alloy, inlay casting gold alloys, plastic teeth, and direct filling resin have been tested; these cylinders approximated in size of the specimens of tooth structure. The average properties in compression for enamel ranged from 1.4×10^6 to 9.1×10^6 psi for modulus of elasticity; from 10,200 to 32,500 psi for proportional limit and from 13,700 to 42,300 psi for compressive strength; these properties depended upon location, that is, cusp, side, or occlusal surface, type of tooth, and orientation of structure. The average values for dentin ranged from 1.1×10^6 to 2.4×10^6 psi for modulus of elasticity, from 12,500 to 24,400 psi for proportional limit, and from 30,000 to 42,300 psi for compressive strength. The average values for the corresponding properties of the restorative materials ranged from 0.27×10^6 to 11.8×10^6 psi, from 6,400 to 33,700 psi, and from 9,700 to 57,800 psi, respectively.

Effect of tensile properties of reinforcement on the flexural characteristics of beams, R. G. Mathey and D. Watstein, *J. Am. Concrete Inst.* **31,** *No. 12, 1253 (1960).*
The effect of magnitude of steel stresses and the nature of the stress-strain characteristics on the center deflection, strain in the concrete, widths and spacing of cracks in the region of constant bending moment, load carrying capacity, and the manner of failure were investigated in a series of flexural beam tests. This series consisted of 12 rectangular concrete beams reinforced with six different types of steel bars with yield strengths ranging from 42,500 to 104,300 psi. The ratio of reinforcement was proportioned inversely to the yield strength, thus providing equal resistance to yielding under tensile forces.

Failure occurred in all the beams at approximately the same load. Test results were compared with values computed with the "straight line" and "ultimate strength" theories. The relationship between the computed steel stresses and the center deflections, width and spacing of cracks, and strain in the steel and concrete was determined for the six types of steel bars.

Interpolation of platinum resistance thermometers, 20° to 273.15° K, R. J. Corruccini, *Rev. Sci. Instr.* **31,** *No. 6, 637–640 (June 1960).*
A numerical method for interpolating the resistance-temperature relation of a platinum resistance thermometer is given. Calibration at three points such as 20, 90, and 273° K is required. The interpolation is then carried out by reference to the complete resistance-temperature relations of two other slightly different thermometers. Limited tests suggest that it is possible to achieve a temperature scale in this way using commercially available thermometers that is reproducible within 0.001 degree, provided the Callendar-van Dusen constants and the residual resistance ratio are sufficiently restricted.

Post office mechanization, B. M. Levin, M. C. Stark, and P. C. Tosini, *Proc. Information Processing and Retrieval, Am. Inst. Elec. Engrs. General Meeting, June 19–24, 1960, Atlantic City, New Jersey, Am. Inst. Elec. Engrs. Paper CP60–937 (1960).*
Post Offices perform repetitive, straight-forward operations on ever-increasing quantities of an input that approaches a degree of physical standardization. Such characteristics strongly imply the feasibility of automatic machinery. This paper discusses considerations involved in such automation. First the design and operational variables and parameters of most present manual Post Offices are presented. This is followed by descriptions of mechanical systems and of systems studies that have been performed. The various concepts are then integrated in a "not-too-blue sky" presentation of a future automated Post Office. This latter discussion deals primarily with the operational requirements imposed on a computer performing the major control functions in the automated system. It should be noted this paper presents some of the work done towards optimizing the operations within an individual Post Office. Concurrent effort is being directed toward optimizing the entire Post Office Department's sorting and distribution activities.

Sensitive thermal conductivity gas analyzer, J. R. Purcell and R. N. Keeler, *Rev. Sci. Instr.* **31** *No. 3, 304–306 (March 1960).*
A thermal conductivity gas analyzer has been designed using A–C excitation for the thermal conductivity cell. This has greatly reduced drift and has increased sensitivity. The unit has a minimum range of 200 ppm N_2 in H_2 for full scale deflection.

For many years the thermal conductivity method of gas analysis has been very popular. One of the first investigators to use this method was Schleiermacher. Farkas and others applied thermal conductivity methods in their research on the isotopic and ortho-para modification of hydrogen.

Transfer of liquid hydrogen through uninsulated lines, R. J. Richards, W. G. Steward, and R. B. Jacobs, *Proc. 1959 Cryogenic Engr. Conf., Vol. 5, Advances in Cryogenic Engineering, p. 103 (Plenum Press, New York, N.Y., 1960).*
For certain applications the transfer of liquid hydrogen through uninsulated transfer lines may be practical and convenient even though the steady state heat flux may be high. Because of the uncertainty about the nature of the condensing film (liquid air and ice mixture) and the unknown effects of liquid hydrogen flow rate and quality, the investigation reported here was undertaken to determine the heat flux to liquid hydrogen flowing through uninsulated lines and to determine pressure drops.

The heat flux was found to be 1.1 watts/cm^4 (3490 B.T.U./hr. ft^2) for still ambient air and 1.9 watts/cm^2 (6020 B.T.U./hr. ft^2) when a 15 mile per hour wind was blowing across the test section. The only factors which produce perceptible, systematic changes in the heat flux are those, such as wind or vibration, which disturb the outside condensing film. The flow rate, quality and transfer line geometry did not affect the heat flux. The pressure drop data indicate that the pressure drop in uninsulated liquid hydrogen lines may be calculated with reasonable accuracy using the correlation of Martinelli and Nelsen.

Atomic clocks for space experiments, P. L. Bender, *Astronautics p. 69–71 (July 1960).*
One prediction of the General Theory of Relativity is that identical clocks operating in regions of different gravitational potential will run at slightly different rates. This effect can be checked by placing an atomic clock in an earth satellite and comparing it with one on the ground. Types of clocks which are suitable for this experiment are discussed. The use of atomic clocks or frequency standards in satellites and space probes for communications and tracking purposes is also mentioned.

Electroless plated contacts to silicon carbide, R. L. Raybold. *Rev. Sci. Instr.* **31,** *No. 7, 781–782, July 1960).*
Electroless plating provides a contact useful for experimental testing of silicon carbide crystals. The process requires a minimum of special equipment and produces a contact with good electrical mechanical properties.

Effect of water-reducing and of set-retarding admixtures on properties of concrete, Introduction and Summary, B. E. Foster. *Am. Soc. Testing Materials Spec. Tech. Publ.* **266** *Introduction 1 & 2 and Summary 240–246 (June 1960).*
This paper records the introductory remarks at the ASTM Symposium on effect of water-reducing and of set-retarding admixtures on properties of concrete, which was held in San Francisco on October 14, 1959.

A barium fluoride film hygrometer element, F. E. Jones and A. Wexler, *J. Geophys. Research* **65** *No. 7, 2087–2095 (July 1960).*
An electric hygrometer element which responds rapidly to changes in humidity is described. The relative humidity indication of the element passes through 90% of a total change in indication in 3 seconds at −20 °C and 8 seconds at −40 °C.

The element consists of a thin film of barium fluoride deposited over metallic film electrodes on a glass substrate. The electrical impedance of the element varies about three orders of magnitude with relative humidity throughout the range 20% to 100% relative humidity at a given temperature. It can be fabricated reproducibly to conform to mean calibration curves.

The results of a laboratory study of performance characteristics indicate that the element responds to changes in relative humidity over a wide range of humidities. In the range studied, no upper or lower limits to the operation of the element were found. Hysteresis effects are small. Exposure to high humidity, water spray, or water immersion had no permanent harmful effect on the functioning of the element. Polarization effects are avoided by using the element only in a–c circuits. Aging effects resulting in shifts in calibration with time require further study.

Other NBS Publications

Journal of Research, Section 64A, No. 6, November–December 1960. 70 cents.
The spectrum of singly ionized atomic iodine (I II). W. C. Martin and C. H. Corliss.
The third spectrum of gold (Au III). L. Iglesias.
Tolerances for layer thicknesses in dielectric multilayer coatings and interference filters. K. D. Mielenz.
Note on particle velocity in collisions between liquid drops and solids. O. G. Engel.
Resistance of white sapphire and hot-pressed alumina to collision with liquid drops. O. G. Engel.
Note on the thermal degradation of polytetrafluoroethylene as a first-order reaction. S. L. Madorsky and S. Straus.
Heat of formation of titanium trichloride. W. H. Johnson, A. A. Gilliland, and E. J. Prosen.
Heat of formation of decaborane. W. H. Johnson, M. V. Kilday, and E. J. Prosen.
Ultra low-conductivity water by electrophoretic ion exclusion. W. Haller and H. C. Duecker.
Spectrophotometric determination of the ionization constant of dimethylpicric acid (2,4,6-trinitro-3,5-xylenol) in water at 25 °C. M. M. Davis, M. Paabo, and R. A. Robinson.
Spectrophotometric determination of the ionization constant of 2,4,6-trinitro-m-cresol in water at 25 °C. M. M. Davis and M. Paabo.
Method for the separation of titanium, zirconium, iron, and aluminum from one another and for their subsequent determination. T. J. Murphy, W. S. Clabaugh, and R. Gilchrist.

Journal of Research, Section 65A, No. 1, January–February 1961. 70 cents.
Faint lines in the arc spectrum of iron (Fe I). C. C. Kiess, V. C. Rubin, and C. E. Moore.
Infrared absorption of spectra of some 1-acetamido pyranoid derivatives and reducing, acetylated pyranoses. R. S. Tipson and H. S. Isbell.
Monolayers of linear saturated succinate polyesters and air liquid interfaces. W. M. Lee, J. L. Shereshefsky, and R. R. Stromberg.
Heat of formation of beryllium chloride. W. H. Johnson and A. A. Gilliland.
Heat of decomposition of potassium perchlorate. W. H. Johnson and A. A. Gilliland.
Heats of formation of lithium perchlorate, ammonium perchlorate, and sodium perchlorate. A. A. Gilliland and W. H. Johnson.
Heat of formation of *N*-dimethylaminodiborane. W. H. Johnson, I. Jaffe, and E. J. Prosen.
Separation of hafnium from zirconium by anion exchange. J. L. Hague and L. A. Machlan.
Reaction of sulfur, hydrogen sulfide, and accelerators with propylene and butadiene. F. J. Linnig, E. J. Parks, and L. A. Wall.

Journal of Research, Section 64B, No. 4, October–December 1960. 75 cents.
Magnetic polarizability of a short right circular conducting cylinder. T. T. Taylor.
Accuracy of Monte Carlo methods in computing finite Markov chains. N. W. Bazley and P. J. Davis.
Error bounds in the Rayleigh-Ritz approximation of eigenvectors. H. F. Weinberger.
Sequence transformations based on Tchebycheff approximations. J. R. Rice.
Numerical solution of the frequency equations for the flexural vibration of cylindrical rods. W. E. Tefft.

Journal of Research, Section 65D, No. 1, January–February 1961. 70 cents.
Incoherent scattering by free electrons as a technique for studying the ionosphere and exosphere: some observations and theoretical considerations. K. L. Bowles.
Radio wave absorption of several gases in the 100 to 117 kMc/s frequency range. C. O. Britt, C. W. Tolbert, and A. W. Straiton.

On the theory of diffraction by a composite cylinder. R. D. Kodis.

An atlas of oblique-incidence ionograms (a digest). V. Agy, K. Davies, and R. Salaman.

A new approach to the mode theory of VLF propagation. J. R. Wait.

East-west effect on VLF mode transmission across the earth's magnetic field. D. Dobrott and A. Ishimaru.

Magneto-ionic propagation phenomena in low- and very-low-radiofrequency waves reflected by the ionosphere. J. R. Johler.

Correlation of monthly median transmission loss and refractive index profile characteristics. B. R. Bean and B. A. Cahoon.

Characteristics of waveguides for long-distance transmission. A. E. Karbowiak and L. Solymar.

Useful radiation from an underground antenna. H. A. Wheeler.

Observation of *F*-layer and sporadic-*E* scatter at VHF in the Far East. K. Miya, T. Sasaki, and M. Ishikawa.

A high-resolution rapid-scan antenna. H. V. Cottony and A. C. Wilson.

Alphabetical index to tables of chemical kinetics. Homogeneous reactions. Supplement 2 to NBS Circ. 510 (1960) 35 cents.

The metric system of measurement, NBS Misc. Publ. 232 (1960) 50 cents.

Standard X-ray diffraction powder patterns, H. E. Swanson, M. I. Cook, E. H. Evans, and J. H. deGroot. NBS Circ. 539, Vol. 10 (1960) 40 cents.

Stabilization of free radicals at low temperatures, edited by A. M. Bass and H. P. Broida. NBS Mono. 12 (1960) $1.50.

New description of thorium spectra, R. Zalubas. NBS Mono. 17 (1960) 65 cents.

Measurement of neutron flux and spectra for physical and biological applications. NBS Handb. 72 (1960) 35 cents.

Protection against radiations from sealed gamma sources. NBS Handb. 73 (1960) (Supersedes H54) 30 cents.

Standardization activities in the United States. A descriptive directory, S. F. Booth. NBS Misc. Publ. 230 (1960) (Supersedes M169) $1.75.

Investigation of bearing creep of two forged aluminum alloys, L. Mordfin, N. Halsey, P. J. Granum. NBS TN55 (PB161556) (1960) $1.00.

A survey and bibliography of recent research in the propagation of VLF radio waves, J. R. Wait. NBS TN58 (PB161559) (1960) 75 cents.

Measurements and standards in plasma-physics and astrophysics at the National Bureau of Standards. NBS Tech. Note 59 (PB161560) (1960) $1.00.

Amplitude and phase of the low- and very low-radiofrequency ground wave, J. R. Johler, L. C. Walters, and C. M. Lilley. NBS TN60 (PB161561) (1960) 75 cents.

Proceedings of the 1960 conference on the propagation of E.L.F. radio waves. (1960) NBS Tech. Note 61 (PB161562).

Rapid determination of the order of chemical reactions from time-ratio tables, J. H. Flynn. NBS TN62 (PB161563) (1960) 75 cents.

Single scattered neutrons from an isotropic point source, E. R. Mosburg, Jr., and W. M. Murphey. NBS TN63 (PB161564) (1960) 50 cents.

Radio refractometry, J. W. Herbstreit. NBS TN66 (PB161567) (1960) 50 cents.

Low- and very low-radio-frequency model ionosphere reflection coefficients, J. R. Johler, L. C. Walters, J. D. Harper, Jr. NBS TN69 (PB161570) (1960) $2.00.

An analysis of an absolute torsional pendulum viscometer, E. A. Kearsley, Trans. Soc. Rheology **III,** 69 (1959).

The black void reactor concept, C. O. Muehlhause, Nuclear Sci. and Engr. **7,** No. 6, 505 (1960).

Dewar system for low temperature experiments, C. T. Zahn, Rev. Sci. Instr. **31,** No. 3, 328 (1960).

Radio echoes from field-aligned ionization above the magnetic equator and their resemblance to auroral echoes, K. L. Bowles, R. Choen, G. R. Ochs, and B. B. Balsley, Letter J. Geophys. Research **65,** 1853 (1960).

Geomagnetic and solar data, J. V. Lincoln, J. Geophys. Research **65,** 1639 (1960); J. Geophys. Research **65,** 1821 (1960).

The spark of originality, A. T. McPherson, The Chemist **37,** No. 7, 275 (1960).

Infrared emission spectra of gaseous B_2O_3 and B_2O_2, D. White, D. E. Mann, P. N. Walsh, and A. Sommer, J. Chem. Phys. **32,** No. 2, 481 (1960).

A demonstration of color perception with abridged color-projection systems, C. S. McCamy, Photographic Sci. and Engr. **4,** No. 3, 155 (1960).

Heat of formation of nitrogen trifluoride and the N–F bond energy, G. T. Armstrong, S. Marantz, and C. F Coyle, Commun. to Editor, J. Am. Chem. Soc. **81,** 3798 (1959).

Elastic constants of synthetic single crystal corundum at room temperature, J. B. Wachtman, W. E. Tefft, D. G. Lam, R. P. Stinchfield, J. Am. Ceram. Soc. **43,** No. 6, 334 (1960).

A simple centering jig and goniometer for punching or drilling spheres for structural models, D. K. Smith, Am. Mineralogist **45,** No. 5–6, 273 (1960).

Propagation of electromagnetic pulses in a homogeneous conducting earth, J. R. Wait, Appl. Sci. Research **B8,** 213 (1960).

Rapid impact loading of textile yarns, J. C. Smith, Book, High speed testing, Vol. 1, p. 67 (Interscience Pub. Inc., New York, N.Y., 1960).

The absolute zenith intensity of (OI) 5577 at College, Alaska, F. E. Roach and M. H. Rees, J. Geophys. Research **65,** No. 5, 1489 (1960).

Studies on sudden commencements of geomagnetic storms using IGY data from United States stations, S. Matsushita, J. Geophys. Research **65,** No. 5, 1423 (1960).

Photometric observations of the twilight glow (OI) 5577 and (OI) 6300, L. R. Megill, J. Atmospheric and Terrest. Phys. **17,** 276 (1960).

Microwave spectrum and internal rotation of ethyl cyanide, V. W. Laurie, J. Chem. Phys. **31,** No. 6, 1500 (1959).

A study of local geomagnetic influence on the (OI) 5577 night-glow emission at Fritz Peak, J. W. McCaulley, F. E. Roach, and S. Matsushita, J. Geophys. Research **65,** No. 5, 1499 (1960).

Local standards laboratories, A. T. McPherson, Handbook of Electrical Measurements, 1960 ed., p. 72 (1960).

Infrared emission spectrum of gaseous HBO_2, D. White, D. E. Mann, P. N. Walsh, and A. Sommer, J. Chem. Phys. **32,** No. 2, 488 (1960).

The stokes flow problem for a class of axially symmetric bodies, L. E. Payne and W. H. Pell, J. Fluid Mech. **7,** Pt. 4, 529 (1960).

A further note on "sweepers," J. M. Watts, J. Atmospheric and Terrest. Phys. **18,** 81 (1960).

The incidence equation $AA^{\mathrm{t}}=aA$, K. Goldberg, Am. Math. Mo. **67,** 367 (1960).

Analysis of two-factor classifications with respect to life tests, M. Zelen, Book, Contributions to probability and statistics, Paper **42,** p. 508 (Stanford Univ. Press, Stanford, Calif., 1960).

OH emission in the earth's atmosphere, D. M. Gates and E. Jones, Proc. 2d Natl. Infrared Information Symp. **4,** 145 (1959).

Microwave spectrum of trans-crotononitrile, V. W. Laurie, J. Chem. Phys. **32,** No. 5, 1588 (1960).

Tropospheric fields and their long-term variability as reported by TASO, P. L. Rice, Proc. IRE **48,** 1021 (1960).

On the power of some rank-order two-sample tests, J. R. Rosenblatt. Book, Contributions to probability and statistics, Paper **32,** p. 358 (Stanford Univ. Press, Stanford, Calif., 1960).

Disc. distribution of flares associated with certain radio bursts, C. Warwick, Proc. Symp. Physical Processes in the Sun-Earth Environment, July 20–21, 1959 (Ottawa, Defence Research Telecommunications Establishment), DRTE Pub. No. 1025, 249 (1960).

The ionization potential of fluorine, J. T. Herron and V. H. Diebeler, Jr. Chem. Phys. **32,** No. 6, 1885 (1960).

The intensity of (OI) 5577 in the subauroral region as a function of magnetic activity, F. E. Roach, J. Geophys. Research **65,** No. 5, 1395 (1960).

A comparative study of absolute zenith intensities of (OI) 5577, F. E. Roach, J. W. McCaulley, E. Marovich, and C. M. Purdy, J. Geophys. Research **65,** No. 5, 1503 (1960).

Clay mineral content of two domestic kaoline, W. C. Ormsby and J. M. Shartsis, J. Am. Ceram. Soc. **43,** No. 6, 335 (June 1960).

Some Canons of sound experimentation, C. Eisenhart, Bull. Inst. Intern. Stat. **XXXVII,** No. 3, 339 (1960).

Thermodynamic properties of helium at low temperatures and high pressures, D. B. Mann and R. B. Stewart, Trans. Am. Soc. Mech. Engrs. J. Heat Transfer **81,** No. 4, 324 (November 1959).

Radiation from a slot on a large corrugated cylinder, J. R. Wait and A. M. Conda, Electromagnetic Wave Propagation, Proc. Intern. Conf. Propagation of Radio Waves, Liege, Belgium, **1958,** p. 103 (Academic Press, Inc., New York N.Y., 1960).

Low-temperature transport properties of commercial metals and alloys. IV. Reactor grade Be, Mo, and W, R. L. Powell, J. L. Harding, and E. F. Gibson, J. Appl. Phys. **31,** No. 7, 1221 (July 1960).

A rating scale method for evaluating research positions, H. A. McKean, J. Mandel, and M. N. Steel, Personnel Admin. **23,** No. 4, 29 (July-August 1960).

A study of two water resistance testers for shoe upper leather, R. L. Hebert, J. Am. Leather Chemists Assoc. **LV,** No. 7, 388 (July 1960).

Bounds on the dissipation of energy in steady flow of a viscous incompressible fluid around a body rotating within a finite region, E. A. Kearsley, Arch. Rational Mech. and Analysis **5,** No. 4, 347 (1960).

Low and medium frequency radio propagation, K. A. Norton, Electromagnetic Wave Propagation, Proc. Intern. Conf. Propagation of Radio Waves, Liege, Belgium, **1958,** p. 375 (Academic Press Inc., New York, N.Y., 1960).

Cavity resonator dielectric measurements of rod samples, H. E. Bussey, Conf. Electrical Insulation (Annual Report of 1959), Natl. Acad. Sci., Natl. Research Council Pub. **756,** 15 (1960).

Analysis of fractionally replicated 2^n3^n designs, R. C. Bose and W. S. Connor, Bull. Inst. Intern Stat. **XXXVII,** No. 3, 141 (1960).

Halobenzenes as sensitizers for the radiation-induced polymerization of styrene, D. W. Brown and L. A. Wall, J. Polymer Sci. **44,** 325 (June 1960).

Some aspects of fluorine flame spectroscopy, D. E. Mann. Proc. Propellant Thermodynamics and Handling Conf. Special Rept. 12 (Ohio State University, Columbus, Ohio, June 1960).

Optical constants of aluminum, H. Mendlowitz. Proc. Phys. Soc. (London, England) **LXXV,** 664 (1960).

Current-thermodynamic research on light-element compounds at the National Bureau of Standards, T. B. Douglas. Proc. Propellant Thermodynamics and Handling Conf. Special Rept. 12 (Ohio State University, Columbus, Ohio, June 1960).

Free radicals in gamma-irradiated polystyrenes, R. E. Florin, L. A. Wall, and D. W. Brown, Trans. Faraday Soc. **56,** No. 453, 1304 (Sept. 1960).

Sealed-off Hg^{198} atomic-beam light source, R. L. Barger and K. G. Kessler. J. Opt. Soc. Am. **50,** No. 7, 651 (July 1960).

Temperature dependence of Young's modulus of vitreous germania and silica, S. Spinner and G. W. Cleek. J. Appl. Phys. **31,** No. 8, 1407 (1960).

Photolysis of ammonia in a solid matrix at low temperatures, O. Schnepp and K. Dressler. J. Chem. Phys. **32,** No. 6, 1682–1686 (June 1960).

Photochemical rates in the equatorial F_2 region from the 1958 eclipse, T. E. Van Zandt, R. B. Norton, and G. H. Stonehocker, J. Geophys. Research **65,** No. 7, 2003 (July 1960).

Influence of source distances on the impedance characteristics of ELF radio waves, J. R. Wait, Proc. IRE **48,** No. 7, 1338 (July 1960).

Statistical models for component aging experiments, J. R Rosenblatt. Intern. Conv. Record. Inst. Radio Engrs. **8,** Pt. 6, 115 (1960).

Isotope effect in the hydrogen atom-formaldehyde reaction, J. R. McNesby, M. D. Scheer, and R. Klein, J. Chem. Phys. **32,** No. 6, 1814 (June 1960).

Electric current and fluid spin created by the passage of a magnetosonic wave, R. P. Kanawal and C. Truesdell, Arch. Rational Mech. and Analysis **5,** No. 5, 432 (1960).

The nature of the inorganic phase in calcified tissues, A. S. Posner. Calcification in Biological Systems, p. 373 (American Assoc. Advancement of Sci., Washington, D.C., 1960).

Absorption spectra of solid methane, ammonia, and ice in the vacuum ultraviolet, K. Dressler and O. Schnepp, J. Chem. Phys. **33,** No. 1, 270 (July 1960).

The extent of H II regions, S. R. Pottasch, Astrophys. J. **132,** No. 1, 269 (July 1960).

Nickel oxide thin film resistors for low pressure shock wave detection, K. E. McCullon. Rev. Sci. Instr. **31,** No. 7, 780 (July 1960).

Casimir coefficients and minimum entropy production, R. E. Nettleton, J. Chem. Phys. **33,** No. 1, 237 (July 1960).

Variations of surface tension calculated with improved approximation for activity coefficient, L. C. Shepley and A. B. Bestul. J. Am. Ceram. Soc. **43,** No. 7, 386 (July 1960).

Council adopts F.D.I. specification for alloy for dental amalgam, Council on Dental Research, J. Am. Dental Assoc. **60,** No. 6, 773 (June 1960).

The foundations of mechanics and thermodynamics, E. A. Kearsley and M. S. Green, Phys. Today **13,** No. 7, 22 (July 1960).

Optical methods for negative ion studies, S. J. Smith and L. M. Branscomb, Rev. Sci. Instr. **31,** No. 7, 733 (July 1960).

On the theory of the slow-tail portion of atmospheric waveforms, J. R. Wait, J. Geophys. Research **65,** No. 7, 1939 (July 1960).

Statistical aspects of the cement testing program, W. J. Youden. Am. Soc. Testing Materials Proc. **59,** 1120 (1959).

Optical transmissivity and characteristic energy losses, H. Mendlowitz, J. Opt. Soc. Am. **50,** No. 7, 739 (July 1960).

Pyrolysis of polyolefins, L. A. Wall and S. Straus, J. Polymer Sci. **44,** 313 (June 1960).

Low-energy photoproduction of neutral mesons from complex nuclei, R. A. Schrack, S. Penner, and J. E. Leiss, II Nuovo Cimento **16,** Serie X, 759 (March 1960).

Adsorption spectra of solid xenon, krypton, and argon in the vacuum ultraviolet, O. Schnepp and K. Dressler, J. Chem. Phys. **33,** No. 1, 49 (July 1960).

Radiation patterns of finite-size corner-reflector antennas, A. C. Wilson, H. V. Cottony, IRE Trans, Ant. Prop., **AP–8,** No. 2, 144 (March 1960).

Structure of sulfurous esters, H. Finegold, Proc. Chem. Soc. (London) p. 283 (August 1960).

VLF : ‘enuation for east-west and west-east daytime propagation using atmospherics, W. L. Taylor, J. Geophys. Research **65,** No. 7, 1933 (July 1960).

Mechanized conversion of colorimetric data to Munsell renotations, W. Rheinboldt and J. P. Menard, J. Opt. Soc. Am. **50,** No. 8, 802 (August 1960).

The use of geostationary satellites for the study of ionospheric electron content and ionospheric radio-wave propagation, O. K. Garriott and C. G. Little, J. Geophys. Research **65,** No. 7, 2025 (July 1960).

**Publications for which a price is indicated (except for NBS Technical Notes) are available only from the Superintendent of Documents, U.S. Government Printing Office, Washington 25, D.C. (foreign postage, one-fourth additional). Technical Notes are available only from the Office of Technical Services, U.S. Department of Commerce, Washington 25, D.C. (Order by PB number). Reprints from outside journals and the NBS Journal of Research may often be obtained directly from the authors.*

Editorial Notice

Beginning with the January issues the covers of all four sections of the Journal of Research of the National Bureau of Standards appear with a changed format to emphasize the subject content of each particular section.

Those who have occasion to make reference to Journal articles—or to request issues or volumes of the Journal from librarians—should continue to use the present conventional method of citing such references with the addition of the section title, as, for example:

> Kuder, M. L., Electronic scanning microscopy for a spectrographic plate comparator, J. Research NBS, 65C (Eng. and Instr.) No. 1, 1–8 (Jan. 1961).

W. A. Wildhack, *Editor.*

UNITED STATES
GOVERNMENT PRINTING OFFICE
DIVISION OF PUBLIC DOCUMENTS
WASHINGTON 25, D.C.

OFFICIAL BUSINESS

PENALTY FOR PRIVATE USE TO AVOID
PAYMENT OF POSTAGE, $300
(GPO)

JOURNAL OF RESEARCH of the National Bureau of Standards Vol. 65C, No. 1 January–March 1961
C. Engineering and Instrumentation

Contents

Page

Electronic scanning microscope for a spectrographic plate comparator. M. L. Kuder. 1

Viscoelastometer for measurement of flow and elastic recovery. Richard J. Overberg and Herbert Leaderman. 9

An ultra low frequency bridge for dielectric measurements. Donald J. Scheiber. 23

The Ephi system for VLF direction finding. G. Hefley, R. F. Linfield, and T. L. Davis. 43

Fast counting of alpha particles in air ionization chambers. Z. Bay, F. D. McLernon, and P. A. Newman. 51

X-ray diffraction measurement of intragranular misorientation in alpha brass subjected to reverse plastic strain. C. J. Newton and H. C. Vacher. 57

Enthalpy and specific heat of nine corrosion-resistant alloys at high temperatures. Thomas B. Douglas and Andrew C. Victor. 65

Determination of minor constituents in low-alloy steels by X-ray spectroscopy. Robert E. Michaelis, Robert Alvarez, and Betty Ann Kilday. 71

Publications of the National Bureau of Standards. 77

For sale by the Superintendent of Documents, U.S. Government Printing Office, Washington 25, D.C. Price 75 cents (single copy)
Subscription price: $2.25 a year; 50 cents additional for foreign mailing.

UNITED STATES GOVERNMENT PRINTING OFFICE, WASHINGTON : 1961